Jupiter's Radiation Belts at 13.8 GHz

Thesis

C. M. Moeckel

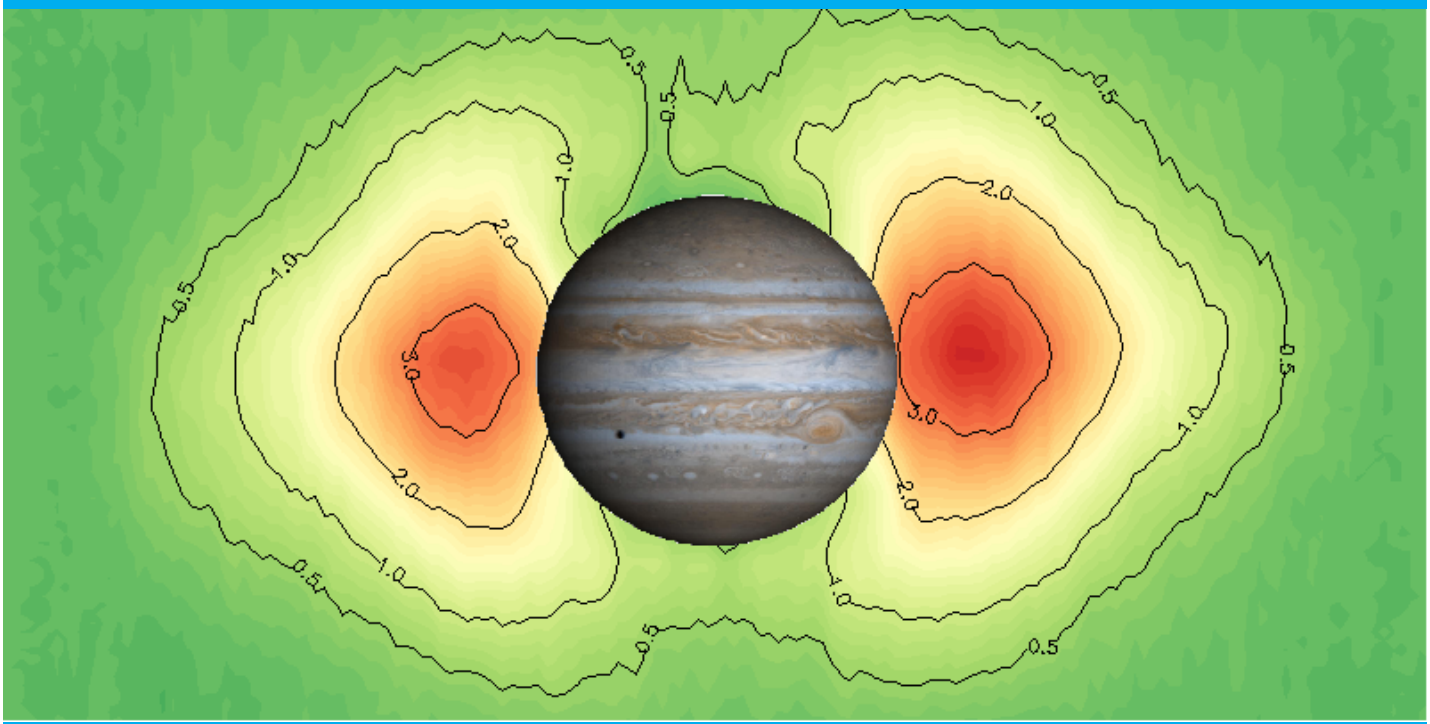

TU Delft

Preface

The work reports on the re-calibration of the Cassini RADAR observation of the Jupiter system. This work was performed at the California Institute of Technology/ NASA Jet Propulsion Laboratory in conjunction with Delft University of Technology and was supported and supervised by Prof. Imke de Pater (TU Delft, UC Berkeley) and by Dr. Michael Janssen (California Institute of Technology).

The thesis committee is formed by:

- Prof. Imke de Pater (Chair of the Assessment Committee)
- Prof. Bert Vermeersen
- Prof. Bernhard Brandl
- Dr. Paco López-Dekker

Lastly, I would like to acknowledge my supervisors for their continuous support. I would like to extend my gratitude to Daniel Santos-Costa, Steve Levin, Bob Sault and Zhimeng Zhang for the scientific discussion. Last but not least, I would like to thank my family for their support and Caro for her patience.

C. M. Moeckel

Delft, May 2017

Jupiter's Radiation Belts at 13.8 GHz

Thesis

by

C. M. Moeckel

to complete the Master of Science
at the Delft University of Technology,

Student number: 4108620
Project duration: May 12, 2017

Front image credits: NASA/JPL - California Institute of Technology/University of Arizona

TU Delft

Contents

Nomenclature

Abbreviations

RMS	Root mean square
AU	Astronimical Unit
BF	Jupiter brightness frame
CMB	Cosmic Microwave Background
EMIC	Electromagnetic Ioncylotron waves
EUV	Extreme Ulatraviolet
JSIII	Jupiter System III (1965), Left-Handed System
LHS	Left-Handed System
RED	Relativisitic Electron Dropouts
SC	Cassini spacecraft frame
ULF	Ultra low frequency waves

Greek Symbols

η_i	Fractional abundance of ion species i	–
Ω_i	Ion-gyrofrequency of ion species i	Hz
ω_{pe}	Plasma frequency	Hz
ω_{pi}	Ion plasma frequency of ion species i	Hz
ϵ	Electron-proton mass ratio	–
γ	Lorentz factor	–
λ	Longitude in a planetocentric Jupiter system	rad
$\lambda_c as$	Spacecraft subsatellite latitude, see CML,	deg, rad
Ω_s	Main beam solid angle	srad
Ω_s	Solid angle of the source	srad
ϕ_i	Beaming curve coefficient: phase of order i	rad
θ	Cone opening angle	rad
$\theta_c as$	Spacecraft subsatellite latitude,	deg, rad
θ_e	Emission angle of the received radiation, measured from local zenith	rad

Roman Symbols

m_e	Rest mass of electron	kg
m_i	Rest mass of ion species i	kg

m_p	Rest mass of proton i	kg
N_e	Plasma density, cold electrons below 10 keV	$1/m^3$
q	Charge of an electron	C
ΔT_{cal}	Temperature variations due to the calibration constant	K
a	Feedline attenuation	K
A_i	Beaming curve coefficient: amplitude of the sinusoidal variations of order i	Jy
B_R	Bandwidh of the Radiometer	Hz
C_{rl}	Antenna count when observing the resistive load	counts
C_{sky}	Antenna count when observing the sky	counts
cal	Calibration constant, relates antenna temperature and antenna counts	K/counts
$cal_{Jupiter}$	Estimate of the calibration constant based on on early Jupiter sca ns	–
cal_{Saturn}	Estimate of the calibration constant based on Titan scans at Saturn	–
E_{min}	Minimum energy for interaction with EMIC waves of phase speed ω	MeV
g_{norm}	Raw gain normalization constant	K/counts
h	Planck's constant	Js
I_h	Spectral intensity, horizontally polarized	W/sr/Hz
I_t	Spectral intensity	W/sr/Hz
I_v	Spectral intensity, vertically polarized	W/sr/Hz
k	Boltzman's constant	J/deg
N_{CMB}	Antenna count of the CMB	counts
N_{sky}	Antenna count on the sky	counts
S_t	Flux density	Jy, W/sr/Hz
$T_{a_{pre}}$	Antenna temperature (pre-liminary)	K
T_A	Antenna temperature	K
T_a	Antenna temperature	K
T_{b-CMB}	Rayleigh Jeans equivlanet CMB brightness temperature at Cassini's frequency	K
T_B	Brightness temperature	K
T_{LNA}	Temperature of the low noise amplifier	K
T_m	Equivalent antenna temperature	K
T_m	Simulated antenna temperature	K
T_{rec}	Receiver noise temperature	K
$T_{rl-nominal}$	Nominal temperature of the resistive load as used in the ground-based calibration	K
T_{rl}	Temperature of the resistive load read out from a sensor	K
T_{RN}	Radiometer noise	K, Jy

T_{sky}	Equivalent antenna temperature of the sky	K
T_{sys}	Equivalent noise temperature of the system	K
u	Dimensionless wave phase speed	–
x	Dimensionless wave frequency	–

List of Figures

List of Tables

Preface

The work reports on the re-calibration of the Cassini RADAR observation of the Jupiter system. This work was performed at the California Institute of Technology/ NASA Jet Propulsion Laboratory in conjunction with Delft University of Technology and was supported and supervised by Prof. Imke de Pater (TU Delft, UC Berkeley) and by Dr. Michael Janssen (California Institute of Technology).

The thesis committee is formed by:

- Prof. Imke de Pater (Chair of the Assessment Committee)
- Prof. Bert Vermeersen
- Prof. Bernhard Brandl
- Dr. Paco López-Dekker

Lastly, I would like to acknowledge my supervisors for their continuous support. I would like to extend my gratitude to Daniel Santos-Costa, Steve Levin, Bob Sault and Zhimeng Zhang for the scientific discussion. Last but not least, I would like to thank my family for their support and Caro for her patience.

C. M. Moeckel

Delft, May 2017

Executive Summary

The inner magnetosphere of Jupiter is characterized by intense radiation, produced when relativistic particles are accelerated in the strong Jovian magnetic field. This environment prevents spacecraft from exploring the inner region of Jupiter without cost-prohibitive heavy shielding; a region, where among others the Galilean moons are high profile scientific targets for the quest of understanding the formation of the solar system (Io) and the existence of life in the solar system (Europa). Scientists, therefore, rely on remote sensing observation to study the inner magnetosphere, by tracking the relativistic electron's synchrotron radiation with radio telescopes. Inversion of the radio emission allows for obtaining an estimate for the number density of relativistic particles in the Jovian magnetosphere. These results can be used to improve radiation models for use in the design of satellite's shielding, which currently rely on large safety factors.

The temporal variability is one of the big remaining questions in synchrotron radiation. Most known processes modulate the radiation belts on time scales of month and years, whereas variations on shorter time scales are still a subject of scientific debate. In this light, the 2001 radio measurements obtained by the Cassini spacecraft during its flyby of Jupiter are very surprising. The obtained estimate of the ultra-relativistic electron number density is considerably lower when compared to model calculations. Initially, the measurement was explained with extreme variability, but the measurements could not be reproduced with ground-based observations. This discrepancy has led scientists to suspect that the measurement was dominated by systematic artifacts common early in the instrument's life cycle, and has prevented modelers from utilizing the Cassini results in their simulations.

In an attempt to provide a solution to these problem, this work aimed at reducing the systematic uncertainties in the retrieval by re-calibrating the raw data. The excellent understanding of the Cassini RADAR, derived from a decade of operation at Titan, was applied to the Jupiter scans. The remaining uncertainties pertaining to spacecraft pointing and the Jovian thermal radiation were solved for by applying a Markov-Chain Monte-Carlo optimization to the full set of 20 Jupiter scans. The synchrotron radiation was then recovered by subtracting the thermal radiation extending from Jupiter's upper atmosphere, which comprises up to 97% of the total signal strength in the Cassini frequency band. The excellent knowledge of the instrument allows for constraining the disk-averaged brightness temperature of 158.6K ± 2.4K and can be used to improve the calibration of radio telescope such as the Very Large Array.

The new retrieval revised the initial measurement to 1.10 Jy ± 0.07 Jy, a 2.5 factor increase compared to the initial estimate, confirming that systematic artifacts propagated into the analysis. A sensitivity analysis was able to pinpoint the thermal contribution of Jupiter, as the main reason for the artificial deflation of power in the original retrieval in 2001. The spatial distribution of the charged particles was obtained by mapping the radiation onto the plane of the sky. These radio maps indicated an enhancement at higher latitudes of electrons, requiring processes to scatter particles to higher latitudes. Comparison with other radio maps demonstrated a positive correlation between the energy of the electrons and the scattering they experienced. Such processes (resonance between plasma waves and energetic electrons) are known to be acting in the terrestrial van Allen belts but have not so far been considered in the Jupiter system.

A simple model was developed that studied the feasibility of these processes in the Jupiter system. As expected these processes are ineffective during nominal conditions, but external disturbances such as fluctuations in the solar extreme ultraviolet flux and extreme volcanic activity of Io could cause conditions where such processes can be sustained. The new analysis makes a strong case for wave-particle interaction in the inner Jupiter magnetosphere and recommends modelers to include these processes, as they might be the key to understanding the short-term variability and can significantly improve our predictive capabilities.

1 Introduction

Extreme measurements can be a blessing and a curse. A blessing because they are scientifically very interesting, advance the state of art, and allow new theories to emerge. A curse because you have to prove that they are not the result of measurement artifacts. This was the case of the Cassini radio experiment at Jupiter, that aimed at mapping the distribution of ultra-relativistic electrons in Jupiter's magnetosphere. The results indicated a lack of energetic electrons and radiation variability on very short timescales. The measurements, however, could not be reproduced with simulations, nor could other measurements replicate their findings. So what did Cassini measure? Did Cassini indeed measure signs of extreme variability or can systematic artifacts explain the extreme data point?

Jupiter and its moons replicate the solar system on a miniature scale. Several minor bodies orbit a central gas giant. This system is therefore highly interesting for planetary science, including atmospheric science studying the complex dynamics in the upper atmosphere, the study of the interior of the planet where the pressure is high enough to form metallic hydrogen or the unique geology of Io's volcanism and Europa's subsurface ocean. Jupiter is characterized by the strongest planetary magnetic field, co-rotating with Jupiter, and to first-order represents a dipole slightly inclined with respect to the planet's spin axis. Many parameters on conditions of the inner magnetosphere can be obtained by ground-based observation in combination with simulations, but in-situ probes can still provide unrivaled resolution. Jupiter is an attractive target for planetary probes exploring the outer solar system, as its gravitational potential is used to boost the spacecraft on its journey. Therefore, there is an incentive from scientists and mission operators to get close to the planet. One problem stands out: intense radiation and charged particles traveling close to the speed of light prohibit long-term exploration and require heavy shielding. Most spacecraft avoid the inner magnetosphere (Galileo, New Horizon, and Cassini), traverse it quickly (Pioneer and Voyager), or use polar orbits to avoid the charged particle environment (Juno). Large uncertainties in our understanding of the distribution of these charged particles result in hefty safety factors for the spacecraft shielding, adding to the many challenges for the exploration of Jupiter's Galilean moons. Therefore, measurements are required that increase our knowledge on the density of these charged paticles close to Jupiter.

The acceleration of these charged particles in the magnetic field produces radio waves, known as synchrotron radiation, which can be picked up by ground-based radio antennas [Ginzburg and Syrovatskii, 1965]. These radio waves allow for estimating the abundance of the electrons from afar, and for decades radio signal from Jupiter have been tracked. Concurrently, models were developed to increase our understanding of the processes regulating the movement of these charged particles. Whereas at lower frequencies the synchrotron radiation is the dominant emission mechanism, at higher frequencies Jupiter's black-body radiation steeply increases and thus dwarfs the synchrotron radiation [Carr et al., 1983]. Most observations, therefore, concentrate on the lower frequency, limiting our understanding of the processes at higher frequencies. Cassini, en route to Saturn, was capable of mapping the high-frequency emissions at Jupiter in more detail, due to the proximity during the flyby. The analysis of the 2001 maps at low frequencies revealed that the magnetosphere was in a highly disturbed state [Santos-Costa et al., 2014], generating interest in how the radiation belts behave at higher frequencies.

In this context, the Cassini results demonstrate that there are less energetic electrons than expected, indicating the existence of processes that should be included in the synchrotron models and potentially allowing for a reduction of interplanetary probes' heavy shielding. Before these results are implemented in current models and applied to the design the next-generation of Jovian explorers, it is, therefore, important to confirm the validity of the results obtained in 2001.

This work aims to address the mismatch between the models and the Cassini observation, by re-calibrating the measurements and systematically decreasing the uncertainties associated with the retrieval. Chapter 2 provides a short overview of the synchrotron radiation principle and the sate-of-the-art knowledge, and a basic overview of how radio measurements are inverted. The methodology that was applied in this report, along with the steps taken to verify the approach, is presented in Chapter 4. The results of the re-calibration are given in Chapter 5, with a brief discussion of possible processes that could explain the Cassini measurements in Chapter 6. The conclusions and the recommendations for future research are summarized in Chapter 7.

2

Literature Review

2.1. Synchrotron radiation

For a more detailed review, the reader is referred to the extended literature review performed prior to the research project. This section is meant to provide context for the research questions.

The electromagnetic waves originating from Jupiter allow for studying the Jovian system from afar. They often are emitted in regions that are difficult to explore in-situ due to harsh environments and long distances involved in space exploration. The various sources differ in intensity, frequency, and their temporal evolution. This review focuses on the emissions that pertain the Cassini frequency of 13.8 GHz, at which two processes are contributing radio waves as seen in Figure 2.1: (i) thermal radiation emitted in the top layer of the atmosphere; and (ii) synchrotron radiation received from the magnetosphere.

This review focuses on the synchrotron radiation as it is the primary target of the Cassini observations. In contrast to the thermal emission, which is generated by thermal motion in the atmosphere, the synchrotron radiation is produced by the acceleration of electrons in a magnetic field. The energy of the electron determines the speed at which they gyrate in the magnetic field, and the Lorentz force controls the radius of curvature in the gyration motion. The curved path in the magnetic field causes the particles to be subjected continuously to centripetal acceleration. This acceleration of charged particles in a magnetic field causes the particles to emit radiation [Roederer, 1970]. The emission of low energy particles, also known as cyclotron radiation, is named after the particle accelerators that exploit this behavior. In this setup, the electrons emit power isotropically, akin to the emission pattern of a dipole antenna. In contrast, the synchrotron electrons, also named after a particle accelerator, are the relativistic counterpart and move at velocities close to the speed of the light. At these velocities, the emission pattern becomes highly confined into a cone in the forward direction [Ginzburg and Syrovatskii, 1965], where the opening angle, θ, is dependent on the energy of the particle $\theta = 1/(2\gamma)$. The frequency of the synchrotron is in theory dependent on the gyration duration of the electron, with a spike at higher harmonics. The large velocity, however, leads to significant Doppler shifts of the radio emitted signal and widens the frequency peak. As a consequence, the resulting power spectrum is spread across many frequencies defined by an emission peak at 0.29 of the critical frequency, ν_c. This specific frequency is a function of the energy of the electrons, E and the local magnetic field strength, B, as $\nu_c = 16.08E^2Bsin(\alpha)^2$ [Carr et al., 1983]. The angle, α, is defined as the angle between the magnetic field vector and the velocity vector. A small pitch angle indicates a particle motion parallel to the field lines, and a pitch angle of 90° is a pure gyration motion. The power, P, that is emitted per particle can be estimated by $P = 6 \times 10^{-22}E^2Bsin(\alpha)^2$ [Carr et al., 1983]. Lastly, the polarization of the radio waves is a result of the electron's orbit and the viewing geometry. Three cases of polarization are displayed in Figure 2.2. An observer, receiving radiation from a purely gyrating electron seen edge on, receives linear polarization. When perpendicular to the gyrating electron, the polarization is circular, for all other observation angles and pitch angles, the polarization is elliptical.

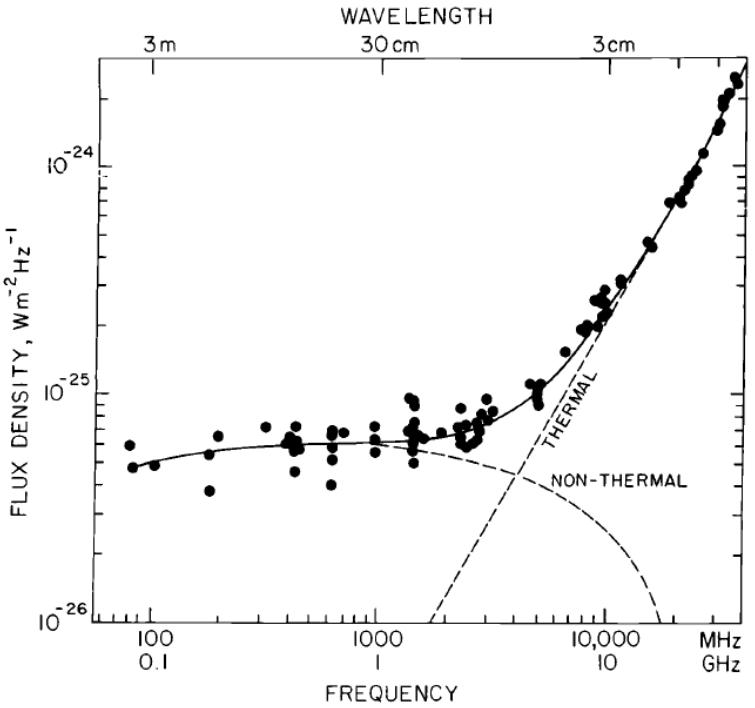

Figure 2.1: Flux density at higher frequencies. From [Carr et al., 1983, Figure 7.2]

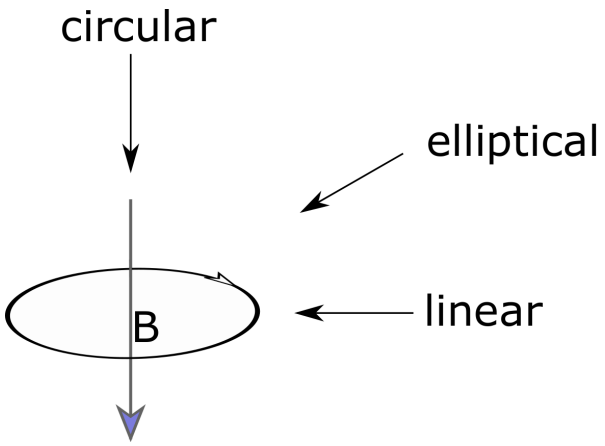

Figure 2.2: Gyrating electron in a magnetic field; polarization as seen by the observer, indicated by the arrow.

2.2. Jovian radiation belts

Jupiter's magnetosphere harbors the conditions for creating synchrotron radiation. Currents in the interior of the planet give rise to the strongest planetary magnetic field in the solar system. The magnetic field is to first-order dipolar, however, close to the planet higher order moments distort the magnetic field considerably [Khurana et al., 2004]. Additionally, a variety of sources, such as Io's volcanic activity, the ionosphere and the impinging solar wind maintain a stream of electrons to the magnetosphere [Bolton et al., 2004, 1989, Carr et al., 1983].

Once, the particles are injected into the magnetosphere their motion is controlled by the magnetic forces and the conservation of the adiabatic invariants [McIlwain, 1961, Roederer, 1970]. The electron velocity can be decomposed into several components: (i) the gyration motion around the magnetic field lines caused by the Lorentz force; (ii) the slow inwards drift towards the planet, a consequence of radial diffusion [Goertz et al., 1979] caused by fluctuations in the ionosphere [Brice and Mcdonough, 1973]; (iii) the bounce motion along the magnetic field between the mirror points is controlled by the second invariant; and (iv) a drift relative to the magnetic field that causes a longitudinal redistribution of particles. The pitch angle of the electron changes along the bounce motion, where minimum corresponds the magnetic equatorial crossing. With increasing latitude, the pitch angle is increased until at the mirror points the electron reaches a maximum of 90°, i.e. a pure gyration motion. The inward motion of the particles results in energization of the electrons. The first adiabatic invariant conserves the magnetic moment of the particles so that an increase in magnetic field strength is accompanied by a proportional increase in energy. This is primary reason for the existence of such energetic particles close to Jupiter.

At Jupiter, the synchrotron radiation is produced in the inner magnetosphere (inside of Io's orbit). The inner boundary is provided by the thin neutral atmosphere. Further outside, the electrons are not energetic enough to produce the characteristic beaming effects. Only as they diffuse inwards, they accelerate through radial diffusion [de Pater, 1981a, de Pater and Goertz, 1990] and gyro-resonant acceleration [Horne et al., 2008] and reach sufficient energy levels and regions of higher magnetic field strength to radiate significant power. The increase in energy and magnetic field strength leads to a ramping up of emitted power when getting closer to the planet, resulting in the typical synchrotron radiation peaks close to the planet.

The electron population responsible for the synchrotron radiation differ in pitch angle and energy. The pitch angle and energy of the electrons determine the location at which the electrons reverse their motion along the field lines. Further outwards, the electrons have a widespread in pitch angle, indicating a more isotropic distribution [Carr et al., 1983]. As the particles diffuse inwards, interaction with the moonlets [de Pater et al., 1997], dust particles [Santos-Costa and Bolton, 2008] and synchrotron radiation losses [Santos-Costa and Bourdarie, 2001] modify the pitch angle distribution. The detailed distribution thus varies with increasing radial distance, but it is best described as a two-component population. The majority of the particles (~ 70%) is contained to the magnetic equator [Roberts, 1965, 1976] and the remaining 30% bounces along the field lines. This behavior is reflected in radio maps, which report a dominating radiation maximum along the magnetic equator, with a secondary emission maximum at ~ 30 ° latitude [Carr et al., 1983].

The inwards boundary of the synchrotron region is defined by the upper thermosphere, where interaction with neutral particles causes recombination and removes the particles quickly [de Pater, 1981a]. The loss cone describes the region in which electrons path intersect with the atmosphere. Since the magnetic field is generated in the interior of the place, all magnetic field lines intersect with the planetary atmosphere, and thus particles with sufficiently small pitch angle enter the atmosphere on their bounce motion along the field lines. The latitude at which the magnetic field enters the atmosphere lines is dependent on the distance to Jupiter, as given by L-shell parameter [McIlwain, 1961]. This parameter quantifies the magnetic field lines, by numbering them based on the distance at which they cross the equator and is often used to describe regions in the magnetosphere. Further outwards, that is on large L-shells, very small pitch angles are required for electrons to enter the atmosphere. Contrary, close to the planet the field lines enter the atmosphere at lower latitudes, and thus more particles collide with neutral particles in the atmosphere, removing particles with small pitch angles rapidly.

The loss cone is the dominant mechanism that removes particles [de Pater and Goertz, 1990], but other process contributed to the loss of electrons. Collision with moons and the thin Jovian rings can cause particles

to be removed or change their motion [Carr et al., 1983, de Pater et al., 1997]. Effectively, all particles with a pitch angle of 70° or smaller are absorbed by interaction with the moonlets [de Pater et al., 1997, Santos-Costa and Bourdarie, 2001], as the bounce motion is quicker than the inwards diffusion. Inwards of Amalthea, several processes decrease the pitch angle again and re-populate the upper magnetosphere. These processes include whistler wave scattering [de Pater, 1981a, de Pater et al., 1997], interaction with dust particles [Santos-Costa and Bourdarie, 2001] and synchrotron radiation.

2.3. Observables

Several metrics are used to quantify the synchrotron radiation. The radiation received covers a wide frequency band. At the lower end (~ 100 MHz) the electrons are not energetic enough to produce synchrotron radiation, the higher end (~ 30 GHz) is determined by the maximum energy the particles can be accelerated to (100 to 160 MeV [de Pater, 1981a, de Pater and Dunn, 2003, Santos-Costa and Bourdarie, 2001]).

The flux density describes the total emitted power at a certain frequency, integrated over the radiation belts. It is given in units of Jansky, Jy, which is equivalent to $10^{26}\ W\ m{-}2Hz^{-1}$. The flux density follows the inverse square law, hence all observations are scaled to a common distance of 4.04 AU to allow intercomparison. The flux density spectrum indicates the power across the relevant frequencies. This quantity was shown already in Figure 2.1, where the slope of the flux density is directly correlated with the electron energy distribution [de Pater, 1991]. Therefore, the flux density spectrum is used to assess the various energy level of the electrons and determine the energy spectrum of the particles.

The variations, caused by Jupiter's rotation, are captured by the so-called "beaming curve", which gives the changes in radiation properties at the various central meridian longitudes (CML), which describes the longitude of the observer in Jupiter reference system III [Yoder, 1995]. This curve is sinusoidal and often decomposed into the first three Fourier components [Klein et al., 1989]. The variations with longitude are a direct consequence of the inclined magnetic field and the beaming effect of the synchrotron electrons. The narrow emission cone in combination with the concentration of the particles in the magnetic equator results in maximum flux when the magnetic equator is viewed edge on, whereas, with increasing magnetic latitude, the viewing angle to the equatorial plane, the emission is decreased. For an ideal dipole, the beaming curve would by purely symmetric, but the higher order moments and varying declination of the observer distort the beaming curve [Dulk et al., 1997, Klein et al., 1989].

The flux is received in the form of radio waves, and their metrics can also be used to describe the synchrotron radiation. The degree of linear polarization is used to study the electron distribution, where a higher polarization indicates more equatorial constrained particles. The degree of linear polarization is about 21% [Bolton et al., 2004], where the exact degree changes with longitude, the frequency of observation and time [de Pater and Klein, 1989]. The degree of circular polarization is very small (< 1%) and originates mostly from the higher latitude [de Pater, 1980b].

Radio maps give the distribution of the radiation across the sky and are useful quantities to constrain local feature such as the secondary emission maxima. A typical example can be found in Figure 2.3, in units of flux density, averaged over the telescope beam's footprint. In this case, the radio maps were obtained from a ground-based interferometer that employs large inter-antenna spacing to map Jupiter [Santos-Costa et al., 2014]. The maps can also be given in units of equivalent brightness temperature, with the advantage that the brightness temperature is an invariant property of the source and does not change with distance.

To this date, seven spacecraft have visited the Jupiter system [Khurana et al., 2004]. The intense radiation in the inner magnetosphere prohibits spacecraft from exploring this region in detail. The Pioneer probes were the first to visit Jupiter and provided invaluable observations on the electron energy distribution [Van Allen, 1976]. Measuring the electron energy and pitch angle distribution is crucial for validating models and improve our understanding of the electron's dynamics. Additionally, the Galileo probe [Fischer et al., 1996] and the Galileo spacecraft [Menietti et al., 2005] added information on the distribution of charged particles. Currently, the Juno mission is exploring the Jovian radio emission in detail, with a primary focus of constraining the magnetic field and the atmospheric composition. Nevertheless, the short visit time and the intrinsic variability of the system only allow for snapshots. Most in-situ observation report on a soft electron spectrum

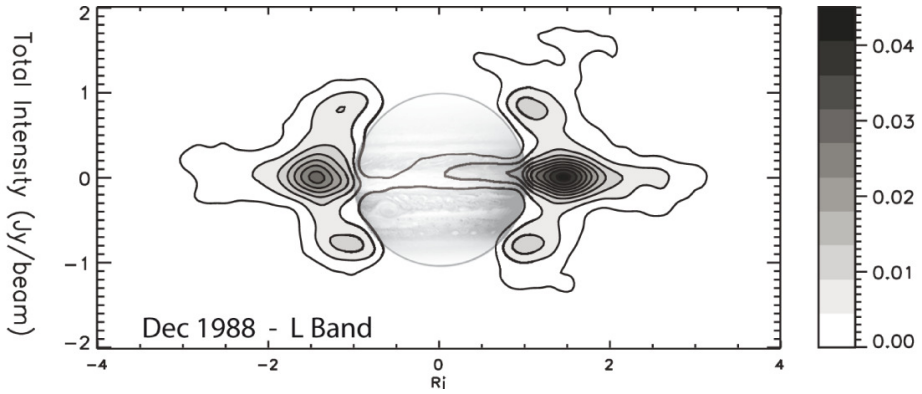

Figure 2.3: VLA radio map of the synchrotron emission at 1.4 GHz measured in Dec. 1988. Adapted from [Santos-Costa et al., 2014, Figure 1]

[de Pater, 1981a, Fischer et al., 1996, Van Allen, 1976], indicating a depletion of the very energetic electron population.

2.4. Models

The synthesis of simulations and models allow for subtracting more information from the observations. There are two different modeling strategies applied: empirical models that invert the ground-based observations and try to reproduce the observation [Divine and Garrett, 1983, Levin et al., 2001] and models based on physical processes [de Pater, 1981a, Kita et al., 2015, Santos-Costa and Bourdarie, 2001]. The physical models solve the Fokker-Planck transport equation [Roederer, 1970], that regulates the motion of particles in the magnetic field, and include the various processes that accelerate and remove particles from the magnetosphere. These model are employed to study these processes separately, and allow for understanding the complex interaction in the magnetosphere. Among others these models were used to study the impact of the solar wind on the synchrotron radiation [de Pater and Goertz, 1994], the interaction with the moonlets [de Pater et al., 1997, Santos-Costa and Bolton, 2008] and the interaction with ring particles [Santos-Costa and Bourdarie, 2001]. The models are crucial tools for studying the time variability of the synchrotron radiation.

2.5. Variability

The time variability of the synchrotron radiation is of particular interest for this research. After the discovery of synchrotron radiation from Jupiter [Burke and Franklin, 1955], the planet received more attention from radio astronomers. Despite larger instrument uncertainties, early observers were able to measure fluctuations in the synchrotron radiation [Gerard, 1970, Klein, 1976, Sloanaker, 1959]. The flux density is the easiest metric to track over long periods, leading to the Jupiter Patrol Program [Klein, 1976] that uses the Deep Space Network and the Goldstone Apple Valley Radio Telescope to track the flux density over the past decades.

The majority of these studies are performed at a single frequency, and thus the impact on other frequency is not well established. Studying the belts at many frequency, requires quasi-simultaneous measurements, to avoid temporal effects propagating into the analysis. The only dedicated campaign comparing the emission at different frequencies [de Pater et al., 2003] have established that the majority of the variability is contained in the lower-frequency observations, and the higher frequencies were shown to be relatively stable.

The radio maps are also known to show variations in their structure. The location of the peak radiation is known to change, moving closer and away from the planet [de Pater, 1991], where an inward movement was found to agree with enhanced radial diffusion [de Pater and Goertz, 1990, 1994]. Similarly, the degree of linear polarization is known to vary with time [de Pater and Klein, 1989], indicating a change in the electron distribution. A detailed comparison of synchrotron maps [Santos-Costa et al., 2014] highlighted that changes in the radio maps could occur across the full synchrotron region, where both a radial and zonal expense in the radio maps was noted.

Variability Drivers

As Earth and Jupiter move in their respective orbit, the viewing geometry changes. The declination of Earth, D_E, is varying between ±3.3° and is known to influence various synchrotron properties. It is, therefore, important to disentangle these effects. The declination is known to affect the beaming curve, the degree of polarization and the location of the synchrotron features [Klein et al., 1989].

Fluctuations in the flux density are in part caused by the varying solar wind conditions [Bolton et al., 1989], which established the solar wind as one of the sources for the electrons in the magnetosphere. The solar wind, especially the ram pressure and the thermal pressure are known to correlate well with the total emission [Bolton et al., 1989, Klein et al., 1989], and inclusion of the number density fluctuation in the solar wind improved simulations [de Pater and Goertz, 1994]. The maximum correlation was achieved when shifting the signal by 2.7 years, a time consistent with the duration of inwards diffusion of particles from Io's orbit to final absorption in the atmosphere [Bolton et al., 1989, de Pater and Goertz, 1994]. Further addition of measurements has degraded the agreement [Santos-Costa et al., 2008], require other processes to control the long-term evolution of the radio belts.

Whereas the solar wind impacts the number density, fluctuations in radial diffusion are known to alter the flux density as well. An enhanced radial diffusion forces particles closer to the planet, a region with stronger magnetic field and thus lead to an enhanced emission. Interaction with dust particles was highlighted as possible additional mechanism that can alter the synchrotron radiation [Santos-Costa et al., 2008].

These processes, however, cannot explain fluctuations on the shorter time scales on the order of days or weeks. A possible explanation for short-term variability involves the impact of EUV flux on the thermosphere [Miyoshi et al., 1999] and its indirect effect on the radial diffusion [Kita et al., 2013, 2015, Santos-Costa et al., 2009]. The observed heating of the upper thermosphere, however, does not seem sufficient to cause an increase in radial diffusion based on the use of physical model [Kita et al., 2013, 2015].

2.6. Jovian Thermal Contribution

At Cassini's frequency band the black-body radiation extending from Jupiter is produced at an altitude where the ammonia clouds are forming [de Pater et al., 2016]. As seen in Figure 2.1 at 13.8 GHz, the thermal radiation is two orders of magnitude larger than the synchrotron radiation. Recovering the synchrotron radiation is critically dependent on accounting for the atmospheric radio emission. Subtraction of the thermal contribution rely on separating the partially polarized synchrotron emission from the randomly polarized thermal emission [de Pater et al., 1982]. The behavior of the polarized light, however, is not well established at higher frequencies [de Pater, 1981b], rendering this method sensitive to uncertainties.

An alternative method comes from modeling and subtracting the thermal emission from Jupiter. Cassini's frequency is in the vicinity of a strong ammonia band, and thus the emission is modulated by the ammonia abundance in the atmosphere. The size of Jupiter does not allow for resolving all the critical processes in Jupiter's atmosphere and model the complete dynamics of the atmosphere. Therefore, simpler models focus merely on the radio emission [de Pater et al., 2001].

Additionally, radio images can be inverted to retrieve the ammonia abundance [Butler and Bastian, 1999, Cosentino et al., 2017, de Pater et al., 2016, Gibson et al., 2005]. The radio images can also be used directly to measure the thermal flux. This flux is highly sensitive to the frequency of observations, and thus only radio images at the correct radio frequency allow for accurately estimating the thermal contribution and their spatial variation [Cosentino et al., 2017, de Pater et al., 2016].

2.7. Antenna Basics

Antennas in their simplest form are transformers between an external electromagnetic waves and an internal voltage across the antenna. They can be used to send out information by modulating the internal current or used to receive information by measuring the volatage across the antenna. In the case of the Cassini measurements, the power emitted by the synchrotron electrons is the main quantity of interest, and thus only receiving aspect of the antennas are discussed.

Antenna temperature

The receiver power collected by the antenna is conventionally converted to the antenna-equivalent temperature T_a. Assuming an extended source with brightness temperature $T_b(\theta,\phi)$ that fully submerges the antenna, then the both quantities equal each other. In a more relaistic case, the brightness temperature varies across the source region, and thus the brightness temperature is defined in the observer's frame of reference as a function of declination θ and ascension ϕ: $T_b(\theta,\phi)$. The efficiency with which the antenna receives radiation is given by the gain of the antenna, $G(\theta,\phi)$, that describes the sensitivity in the same frame of reference. The antenna temperature is then determined by integrating the sky's brightness convolved with the sensitivity pattern of the antenna [Janssen, 1993, Chapter 1]:

$$T_a = \int\int_{4\pi} G(\theta,\phi)\, T_b(\theta,\phi)\, sin(\theta)\, d\theta\, d\phi \tag{2.1}$$

In radio observations, the brightness temperature of the sky is the quantity of interest, so that the antenna temperature has to be inverted to obtain brightness temperature. This inversion requires precise knowledge of the antenna temperature and the gain of the antenna.

Receiver Calibration

The receiver behind the antenna, however, does not measure a temperature, rather a voltage or a sky count. The relationship between the antenna temperature and the read-out voltage must be established first. For radiometer operating in the radio band, radiometer's voltage is linear with the antenna temperature [Janssen, 1993]. It is, therefore, sufficient to observe two targets, that ideally differ significantly in brightness temperature to establish this dependence [Janssen, 1993, Ulaby et al., 1981].

Targets for Calibration There is a range of sources that are used to calibrate the receiver of the Cassini RADAR. Throughout all the observations the Cosmic Microwave Background (CMB) was used as a cold reference. This radiation is a remnant from the early universe and has a very stable temperature across the full sky of 2.7 K, with fluctuation well below the noise level of Cassini.
For the hot reference, there are several options available. The Cassini RADAR can be calibrated with:

- Galactic radio sources such as M17, Cassiopeia-A, Taurus-A and Orion A [Elachi et al., 2004]. These sources are measured independently with the ground based systems as a reference.
- Planetary emitters such as Saturn and Jupiter, assuming that the temperature structure is well understood and modeled.
- The best calibration source stems from in-situ measurements of Titan's atmosphere and surface obtained by the Huygens probe [Fulchignoni et al., 2005].
- An internal reference in the form of a matched resistor with a known temperature can be used for a rough calibration.

Stability The instrument was designed to have a very stable performance, and the gain fluctuates less than 2% [Elachi et al., 2004]. West et al. [2009] estimated that for observations that last up to 100 seconds, the gain is essentially constant, which is far above the 1-second observational cycle of Cassini. The calibration is explained in more detail in Chapter 4.

Additional to the short term gain drift, the instrument performance changes over the course of the mission, which cannot be tracked by the calibration. This drift is obtained by comparing the response of the antenna to an invariant source, which is observed at different times during the mission. The Cassini mission used Titan as a reference target [Janssen et al., 2009, 2013, 2016], due to the in-situ knowledge of Titan's physical temperature [Fulchignoni et al., 2005] and the existence of dune, which have well-understood radio emission properties.

Beam Sensitivity Pattern

Radar antennas have typically a narrow region, the so-called main beam, where the antenna is very sensitive to radiation. This main beam follows a Gaussian beam shape and can be measured with high certainty. The angle at which the Gaussian shape breaks down is defined as the start of the near side lobes. This region has a low, but non-negligible contribution to the antenna temperature, and thus they must be included in the

retrieval. The weak response from the side lobes results in larger uncertainty associated with their knowledge. The normalized radiation pattern can be found in Figure 2.4.

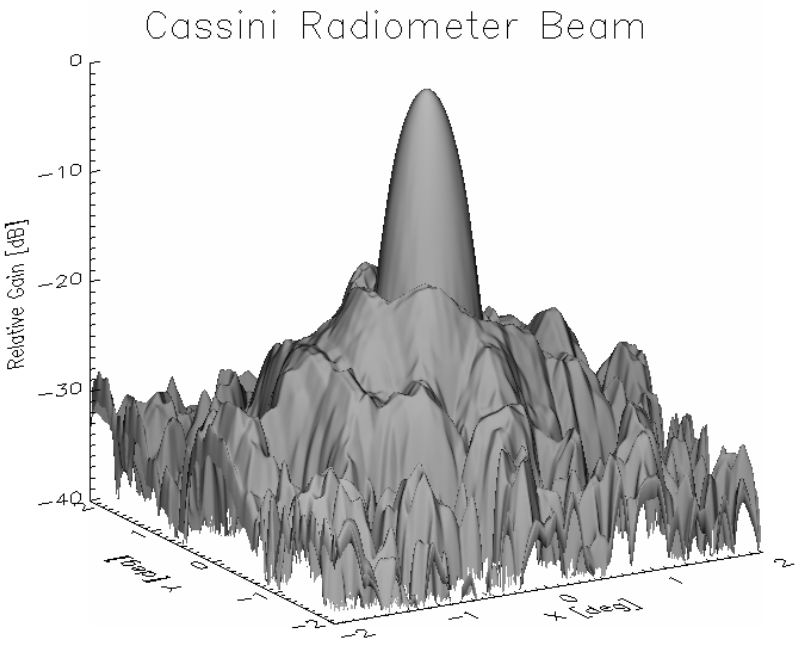

Figure 2.4: The updated beam pattern based on solar scans performed prior to Saturnian Orbit Insertion [Janssen et al., 2009].

Cassini RADAR Beam

This section will discuss how the beam calibration has evolved throughout the mission. The Cassini radiometer, which relies on the communication antenna, has a significant contribution from the side lobes, up to a declination of 60° [Janssen et al., 2009]. The Cassini beam shape is, therefore, defined by three regions, with decreasing sensitivity knowledge: the main beam, the near side lobe, and the far side lobes.

Main beam The main beam is the region of highest sensitivity, where the majority of the signal is collect. It follows a Gaussian beam shape until it gains drops to the -20dB level at a declination of 0.5°. The angle, at which the beam pattern diverges from a Gaussian beam profile is the defined as the cut-off for the main beam. The main beam pattern was established through a combination of ground-based testing and several scans during the cruise phase of the mission. Initially, a combination of Sun and Jupiter scans was used. Later on in the mission, only sun scans were used [Janssen et al., 2001, 2009].

Near side lobes The near side lobes begin at the -20dB level and become gradually weaker further outwards until they are truncated at -40 dB level. The cut-off is defined by the radiometer sensitivity level, that cannot longer resolve signal below the -40 dB level. The near side lobes are characterized by a gradual decrease in sensitivity with an additional fine structure on top. The sensitivity of the near side lobes was established together with the main beam by performing raster scans on the sun.

Far side lobes The existence and extent of the far side lobes were unknown during the Jupiter observations, but measurements from Saturn indicated that they account for as much as 35% of the signal [Janssen et al., 2013]. Their signal contribution is below the detection limit of the radiometer, and thus they cannot be obtained directly from the sun scans. Instead, their structure was obtained through an indirect method developed by Janssen et al. [2009], that minimized residuals between overlapping maps and assuming that the gain is radially symmetric.

Cassini Scan Cassini's flyby provided scientist with the unique advantage of testing their instruments, while simultaneously studying the Jovian system. The flyby occurred on the 29th of December in 2000, at a relatively benign distance of 138 R_J, and the Cassini RADAR scans were performed on the 2nd and 3rd of January when the spacecraft had already receded to 149 R_J. Each scan was designed to take an hour, in which the beam was moved systematically across the emission region. The 20 scans obtained by Cassini covered two complete rotations of the planet, where after the first ten scans the spacecraft was rotated by 90°. Recovering the total radiation, with a linearly polarized antenna, requires two set of measurements perpendicular to each other, resulting in the in 90° rotation of the spacecraft halfway the mapping campaign. The flyby saw Cassini passing through the Jupiter system in the equatorial region with a sub-spacecraft latitude slowly varying from ~ -1.3° to -1.7°.
The Cassini spacecraft hosts a Cassegrain reflector that couples the 4m antenna to the onboard radiometer [Elachi et al., 2004]. The antenna was designed for its primary communication task, however, in conjunction with the radiometer can also be used to the study the surface of Titan through the optically thick atmosphere. The instrument can operate in passive mode, by simply receiving radiation, or in active mode, by sending out radar pulses and measuring their return signal. Finally, the main properties of the Cassini beam are highlighted in Table 2.1.

Table 2.1: Main characteristic of the Cassini RADAR instrument obtained from [Elachi et al., 2004]

Instrument		**Beam properties**	
Frequency	13.78 GHz	Beamwidth	0.36 deg
Wavelength	2.18 cm	Main beam	$0 < \theta < 0.5$ deg
Bandwidth	135 MHz	Near side lobes	$0.5 < \theta < 2$ deg
1-σ Noise	0.13K	Far side lobes	$0.5 < \theta < 2$ deg
Polarization	linear		

3

Problem Statement

To this date, the results of the initial retrievals are contested, as the extreme low flux density obtained in 2001 [Bolton et al., 2002] disagrees with other high-frequency measurements. Furthermore, modeling efforts were not able to reproduce the measurements at high frequency, considering the enhanced flux at lower frequency [de Pater and Dunn, 2003, Santos-Costa et al., 2014]. The extreme measurement point could highlight processes that have caused such a rapid depletion of these particles and thus are of interest. Nevertheless, due to the early nature of the measurements, the possibility of systematic artifacts propagating into the analysis cannot be ruled out. Therefore, the second aspect of this analysis is to reduce the systematic uncertainties through various measures.

Points of Improvement

The following discrepancies were identified in the initial research and, therefore, require a more in-depth study.

Beam pattern Prior to the Jupiter scans, the beam pattern, especially in the near side lobes were not very well constrained [Janssen et al., 2001]. Considering their impact as established at Saturn [Janssen et al., 2013], an updated beam pattern is expected to reduce the uncertainties significantly. Before the Saturn Orbit Insertion, the full beam pattern was established based on raster scans at the sun Janssen et al. [2009], resulting in a noticeable improvement of the fine structure in the beam.

Thermal model Recovering the synchrotron radio contribution requires accounting for the thermal contribution of Jupiter. To take full advantage of the refined beam shape, a high-resolution description of the Jovian thermal contribution is required. Ground-based observatories such as the VLA have a calibration uncertainty in the microwave region of $approx$ 5 K [de Pater et al., 2016] and with that an order of magnitude above the sensitivity level of the observations. For this purpose, a limb-darkened model was constructed and interpolated onto a three-dimensional representation of Jupiter. Additonally, the zone-belt structures which are characterized by varying ammonia abundances are added on top of the base model to account for zonal variations in the brightness temperature.

Gain drift The change in performance on time scale of years is based on repeated measurements of Titan's thermal emission. Low solar forcing results in a stable temperature environment on Titan for years, and thus is an ideal target for establishing instrument's gain drift. The landing of the Huygens probe provided scientist with an in-situ measurement of the temperature on Titan's surface [Fulchignoni et al., 2005] and the well-modeled emission from sand dunes allows for constraining the calibration to an unprecedented level of accuracy [Janssen et al., 2009]. Through observations of this emission source at different epochs, it was found that the response of the antenna decreases linearly by 0.3% per year [Janssen et al., 2013]. This gain drift can be extrapolated backward to the exact date that Cassini did its initial Jupiter observations and results in absolute calibration uncertainty as low as 1%.

The overall goal of the research, therefore, can be summarized by the following objectives:

Quantifying the abundance of Jupiter's high energy electron population by re-calibrating the Cassini radio measurements.

1. Incorporate updated pointing and timing in the retrieval routine using the SPICE kernels for the original observations
2. Update the thermal model based on new understanding of the temperature structure at Jupiter
3. Apply the beam shape obtained through the ten years of operation at Titan
4. Compute the total emission and compare this emission to previous and later measurements
5. Stich together the individual observations to create radiation maps and compare to ground-based observations
6. Determine processes that can explain the deviation from other observations

The following list presents the question that the research proposal is aiming at answering.

1. Are the original measurements a consequence of systematic uncertainties?
   (a) How much radiation can be attributed to the extended sidelobes of the Cassini RADAR beam?
   (b) How much radiation was received from the atmosphere?
   (c) Are spacecraft pointing and timing offset propagating into the analysis?
2. How does the observed structure compare to ground-based observations?
   (a) Does the observed structure compare well with concurrent lower-frequency measurements (1.4 GHz and 325 MHz)?
   (b) Are there significant changes in structure when comparing to earlier/later observations?
3. Is the low abundance of high energy electrons as seen by Cassini a natural phenomenon?
   (a) What processes could cause such variations on short time scales?
   (b) What processes could cause such variations on longer time scales?

4

Retrieval methodology

The following section describes the relevant background information for performing the retrieval. After explaining the geometry during the flyby and the corresponding reference frames, the section details the calibration algorithm and concludes with the description on the uncertainty optimization.

4.1. Reference Frames

Reference frames are necessary to describe the viewing geometry and the relative positioning of the Jupiter and Cassini during the flyby (See Figure 4.1 for the three relevant frames). All refrence frames were verified through unit vector conversion and comparison with analytical expectations.

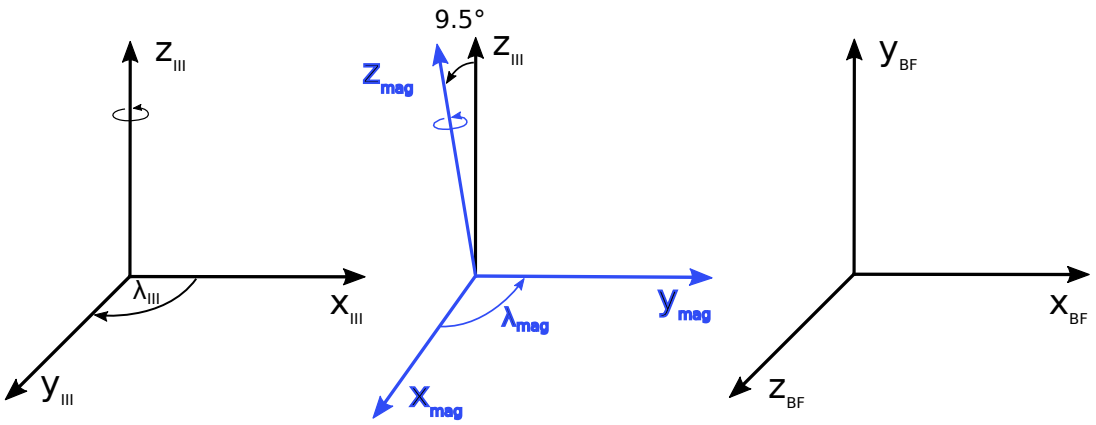

Figure 4.1: Three relevant reference frames: (left) indicates the left handed system III coordinate system aligned with the spin axis; (middle) gives the magnetic reference system, that is right handed and defined by the magnetic poles; (c) the brightness frame in which the brightness distribution of Jupiter is expressed.

4.1.1. Jupiter Frame

The motion of the spacecraft around Jupiter is expressed in the Jovian System III (1965) [Berge and Gulkis, 1976, JSIII], a geocentric, co-rotating frame. The x-axis is tied to the Jupiter's vernal equinox in 1965 and de-

fines the Prime Meridian. The Z-axis is aligned with the spin axis of Jupiter, and the Y-axis completes the left-handed system. In this analysis, the subscript $_{III}$ refers solely to the left-handed definition. Whereas recent publications have also used the notation to refer to a right-handed system, for comparison with older observations the notion of left-handed system is preferred. The spacecraft's position is defined by the subsatellite longitude, commonly expressed through the Central Meridian Longitude (CML) and the planetographic latitude, that is measured from the equator. In the JSIII system, the CML is increasing with time during the observations for a quasi-stationary observer.

4.1.2. Jupiter Brightness Frame

The retrieved quantities are displayed in a frame that is more intuitive for the reader. The Jupiter brightness frame ($_{BF}$) is centered on Jupiter, the x and y-axis create a plane perpendicular to Cassini, and the Jupiter-Cassini vector defines the z-axis. The positive y-axis is aligned with Jupiter's spin axis (geometric view) or with the magnetic dipole (magnetic view), and the x-axis completes the right-handed system.

4.1.3. Magnetic Frame

The synchrotron radiation is inherently tied to the magnetic field structure of Jupiter, so that part of the analysis is performed in a magnetic field frame. The most advanced magnetic field model at the time of writing is the VIP4 model [Connerney et al., 1998], that to first order degree is expressed by dipole tilt of 9.5 ° towards longitude λ_{III} = 200.8 °. The z-axis is aligned with the dipole; the x-axis is defined by the crossing of the magnetic equator with the spin axis equator at λ_{III} = 290.8 °; and the y-axis completes the right-handed system. In the right-handed system, the longitude is decreasing with time for an observer, and the co-latitude is measured from the pole.

4.1.4. Spacecraft Frame

Lastly, a spacecraft centered frame is used to describe the relative position of Jupiter and the beam center. The Cassini spacecraft frame is defined (SC) by physical features on the spacecraft so that the x-axis points away from the Huygens probe; the y-axis is parallel to the magnetic boom and the z-axis points in the direction of the propulsion system (see Figure 4.2). The RADAR 3 subsystem is aligned with the negative z-axis.

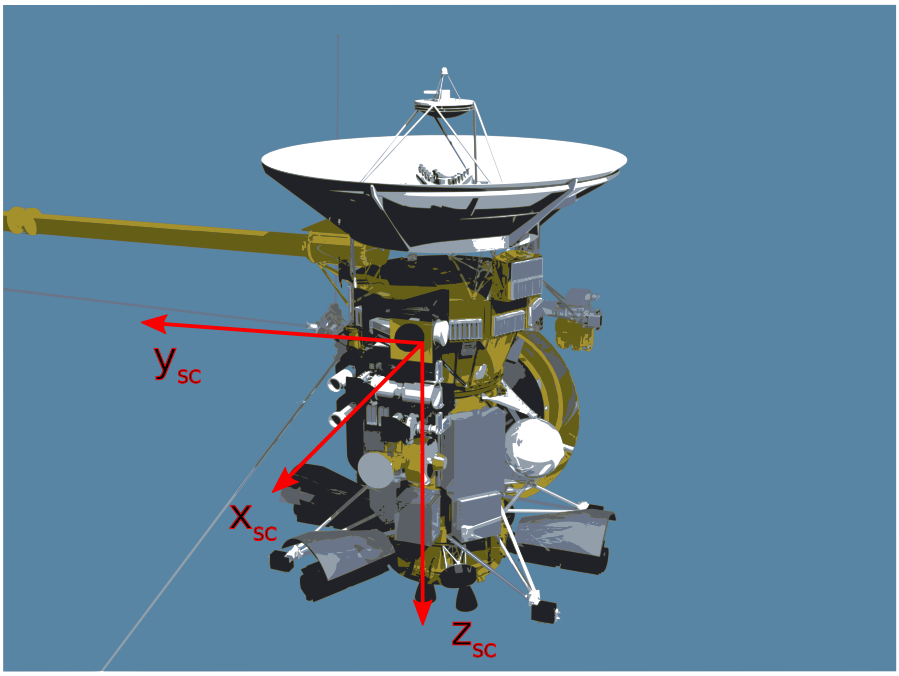

Figure 4.2: Cassini spacecraft reference frame

4.1.5. RADAR 3 Field of View

The field of view of the RADAR 3 instrument is determined by the knowledge of the spatial beam sensitivity. As discussed in Chapter 2, the main beam and near side lobes are well-established ±2° from the beam center. The far side lobes are one-dimensionally constrained and extend outwards to 60°. The use of the far side lobes in the current analysis is superfluous for two main reasons: (i) the vast distances assured Jupiter, and its emission belts always remained within the near side lobes; (ii) there are no other strong radio emitters in the vicinity of the Jupiter system, that in combination with the low sensitivity of the far side lobes, could alter the retrieval. Therefore, the field of view is shown in Figure 4.3, with Jupiter and the main beam to scale.

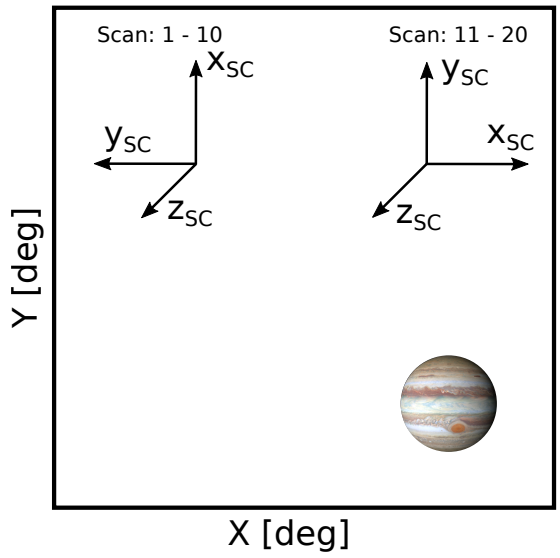

Figure 4.3: Field of View of the Cassini RADAR instrument with Jupiter to scale compared to the half power beam width (0.36 deg) of the instrument. The reference frame indicates the relative orientation to Jupiter for the two sets of scans. During the first ten scans, the spacecraft x-axis was aligned with Jupiter's spin axis, whereas during the second set the y-axis was aligned with Jupiter. Naturally, the antenna is pointing towards Jupiter, so the spacecraft z-axis is pointing away from Jupiter. Jupiter is located around ~ 150 R_J inside the figure.

4.2. SPICE

NASA's Navigation and Ancillary Information Facility (NAIF) has developed a "SPICE", a tool to standardize the calculation and retrieval of observation parameters for ground and space-based mission. This powerful software allows a range of capabilities, including the access to physical parameters, information on spacecraft's position and orientation and the computation, the rotation matrices between individual reference frames and the retrieval of the viewing conditions during the observations. The relevant parameters are presented in the result section.

4.3. Raster Scans

The Jupiter observations constituted a total of 20 hours observations, that span two complete rotations of the planet. The spacecraft was rotated after 10 hours, to switch from vertical polarization to horizontal polarization and monitor the planet at two different polarizations with a linear antenna . During the first part of the scan, the spacecraft's x-axis was perpendicular to the orbital plane, whereas during the second campaign the y-axis was pointed away from the plane as seen in Figure 4.3. As discussed in Chapter 2, the operations of radiometer requires two calibration targets, hot and cold. The calibration in combination with coverage of the main emission region was achieved by moving the beam across the planet and sufficiently far off the limb to obtain a cold target measurement. The scan covers a region of 8x6R_J, with an elongated east-west component to reflect the elongated synchrotron raditation region in the equatorial plane. The scans are initiated by moving the beam to the north-east of the planet and then systematically covering the emission region, where the scan paths are separated by half a beam width. An example of such a scan can be found in Figure 4.4, with the beam and Jupiter to scale in the Jupiter brightness frame.

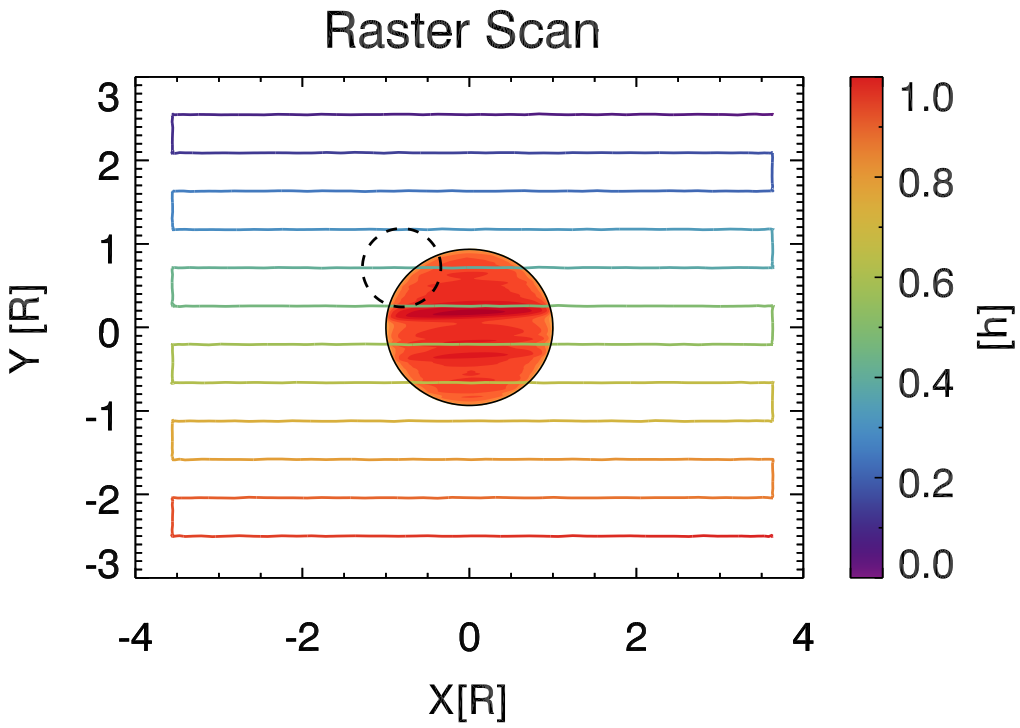

Figure 4.4: Raster scan of Jupiter's inner magnetosphere where the colors indicate the time of one scan. The scan is set conservatively to cover the region where the main emission is originating from. The beam is given to scale by the dotted line.

4.4. 3D Model

This section describes how Jupiter was represented during the retrieval in the Jupiter Brightness Frame. Jupiter is the fastest rotating planet in the solar system with a spin period of just under 10 hours, which causes the planet to have a significant equatorial bulge. The resulting oblate spheroid is best described by the equatorial (R_{Je}) and polar radius (R_{Jp}).

Accounting for the Jovian thermal emission required a description of Jupiter in the field of view of the instrument. First attempts of representing Jupiter as a flat disk, with a prescribed temperature distribution caused large residuals close to the limb. For a better representation, the planet was represented by a full three-dimensional model. As a first estimate, Jupiter was modeled as an oblate spheroid with the equatorial and polar radii as semi-major and semi-minor axis [Hilbert and Cohn-Vossen, 1952] as defined in the brightness frame,

$$\frac{y_{BF}^2}{R_{Jp}^2} + \frac{x_{BF}^2 + z_{BF}^2}{R_{Je}^2} = 1 \tag{4.1}$$

where x and y are the in plane coordinates, and z gives the out of plane coordinates.

This approximation is limited to an observer in the equatorial plane (x-z plane). Since Cassini flyby occurred out of this plane, the system had to be adapted to include the different viewing angle. Realizing that an oblate spheroid seen at different latitudes represents an ellipsoid, the resulting three-dimensional structure can be described by [Hilbert and Cohn-Vossen, 1952]:

$$\frac{x_{BF}^2}{R_1^2} + \frac{y_{BF}^2}{R_2^2} + \frac{z_{BF}^2}{R_3^2} = 1 \tag{4.2}$$

where the three semi-axes (R_1, R_2 and R_3) are obtained by rotating the oblate spheroid by the spacecraft's planetocentric latitude, θ_{cas}, around the x_{BF} axis. Recalling that the surface of Jupiter as a function of latitude is described as:

$$R(\theta) = R_{Je}(1+\eta^2 cos(\theta))^{-1/2} \tag{4.3}$$

with

$$\eta = \frac{R_{Je}^2 - R_{Jp}^2}{R_{Jp}^2} \tag{4.4}$$

$$R_1 = R_e \tag{4.5}$$
$$R_2 = R_{Je}/(1+\eta^2 cos(\theta_{cas}))^{-1/2} \tag{4.6}$$
$$R_3 = R_{Jp}/(1+\eta^2 cos(\theta_{cas}))^{-1/2} \tag{4.7}$$

The resulting three-dimensional structure is updated as Cassini's latitude changes slowly during the observations.

Jupiter's spin axis is slightly inclined with respect to the orbital plane (3.12° Yoder [1995]). An analysis of the spacecraft's orientation revealed that the spacecraft was not fully aligned with Jupiter's spin axis, rather with the momentum vector of the orbital plane. This misalignment manifest itself as a small rotation of Jupiter inside the Radar 3 frame. The relevant parameters are presented in Table 4.1 for the flyby epoch. The corresponding angle was obtained by projecting the spin axis and Cassini's x (y-axis, depending on the polarization) onto a plane, that crosses Jupiter's center and is normal to the vector linking Jupiter and Cassini. The projection is obtained by representing the spin axis as a vector and subtracting the normal to the plane component [Hilbert and Cohn-Vossen, 1952]:

$$u_p = u - \frac{u\dot{n}}{||n||^2} n \tag{4.8}$$

where,

- $\boldsymbol{u_p}$ Projected vector onto the plane
- $\boldsymbol{u}$ The vector to be projected onto the plane
- $\boldsymbol{n}$ The normal vector to the plane

	Jupiter's spin axis	Jupiter	Cassini
Right Ascension [deg]	268.06	60.05	59.06

Table 4.1: Relevant angles for calculating the obliquity of the planet in the celestial sphere for the scan 10 epoch. The data are taken from the latest ephemerics [Archinal et al., 2011]

The angle between the two projections is the apparent obliquity, which is found to be -2.23 °. This means that Jupiter has a slight counterclockwise rotation in the RADAR 3 frame. Noteworthy is also that Cassini passed Jupiter at a smaller right ascension, which is in contrast to the paper of [Hansen et al., 2004, Fig. 2], where presumably the X and Y axis have been flipped.

The resulting model is a three-dimensional model in Cartesian coordinates. For a better description of the brightness distribution across the sky, the system is interpolated into an angular grid. For each point, the corresponding angles are obtained using basic trigonometry:

$$\theta = atan\left(\frac{x}{z}\right) \tag{4.9}$$
$$\phi = atan\left(\frac{y}{z}\right) \tag{4.10}$$

4.5. Brightness Model Jupiter

Differentiating the synchrotron emission from the observations requires an accurate description of the Jovian atmospheric contribution. The radio emissions from a thermal source are determined by the brightness temperature of the medium following the principle of the blackbody radiation in the Rayleigh Jeans limit. At 13.78 GHz regime, the radio emissions originate from the top of the atmosphere, the region where the ammonia clouds are forming. At 1.3 cm, ammonia has a strong absorption band and therefore, is the main volatile that controls the brightness of the radio emissions. The temperature follows an adiabatic and as such increases with decreasing altitude at the 1-10 bar level Lindal et al. [1981], a low abundance allows for probing deeper into the warmer region of the atmosphere [De Pater and Massie, 1985]. Contrary, a large ammonia abundance renders the atmosphere opaque to the hot inner regions, and the emission effectively originates from the colder, upper region of the atmosphere. These ammonia variations correspond well with the visual features on the planet; a brown belt corresponds to a hot region, whereas the white zones and plumes indicate a reduced brightness temperature.

For a first order approximation, the Jovian brightness can be modeled as a simple limb-darkened model. This model is based on globally averaged ammonia abundance, resulting in a uniform temperature distribution, that decreases with increasing emission angle θ_e. The extended path of the radiation through the atmosphere increases absorption and causes a reduction in the brightness temperature. Towards the limb of the planet, the brightness temperature falls of corresponding to the emission angle, so that

$$T_b(\theta_e) = T_b(0) * cos(\theta_e)^{p_{(\nu)}} \tag{4.11}$$

where p determines the amount of limb darkening. Since the limb darkening is a function of the optical depth of the medium, the factor p_ν is frequency dependent. Cassini constitutes single frequency measurements so that the subscript $_\nu$ can be omitted in this work. At the Cassini RADAR frequencies, p takes up 0.08 corresponding to little limb darkening [de Pater et al., 2016]. There are, however, also indications that the ammonia abundance towards the poles is decreased, which effectively decreases the less limb darkening in the north-south direction (see [de Pater, 1986, Fig. 16]).

Three different models with increasing level of detail were applied to study the influence of the brightness model on the retrieved quantities. The models distinguish themselves by the complexity of the temperature variations and the resolution to resolve this structure.

4.5.1. Base Model

The brightness temperature is controlled by the optical depth of the atmosphere. With increasing incidence angles, the path through the atmosphere is longer, and thus signal is attenuated. The initial retrieval was based on this principle. Jupiter's brightness temperature was obtained through a model atmosphere that provided the brightness temperature for a given incidence angle. This apprach assumes a globally averaged ammonia abundance with a uniform limb darkening coefficient. Therefore, the base model for the retrieval is reproducing this atmosphere, by prescribing a nadir temperature and applying a limb darkening coefficient of 0.08 to it. Due to the large beam width, this model is sufficient to obtain a quick estimate and can be used to test algorithms.
The uniform limb darkening coefficient of 0.08, however, is in conflict with the ammonia depletion at the pole. A uniform limb darkening coefficient underestimates the radio contribution from the higher latitudes, and after subtracting the thermal emission from the observations results in bright residuals close to the poles. The initial retrieval suppressed these residuals by increasing the brightness temperature, across the whole globe, resulting in overestimating the radio emissions closer to the center.

Therefore, a first improvement over the base model comes by incorporating the depleted ammonia abundance at the poles. For this purpose the limb darkening coefficient, p was split into two separate terms: p_{EW}, describes the east-west limb darkening, whereas p_{NS} refers to the north-south component, with $p_{NS} < p_{EW}$.

4.5.2. Zonal Model

Abundance variations of ammonia are not limited to the poles but are predominant across the whole planet. The zone-belt structure is the best indication for the variations in the ammonia abundance with latitude. Especially, the Northern Equatorial Belt (NEB) is highly depleted of ammonia and results in a strong positive radio anomaly. The equatorial zone is also characterized by the synchrotron radiation maximum, which is centered on the magnetic equator. The overlap of these two high-emission regions can cause artifacts in the

analysis. For this reason, the second improvement is the inclusion of zonally averaged brightness variations. This analysis can be extended to add a further dimensionality and include the longitudinal variations in the zone-belt structure. Recent images obtained with the VLA [Cosentino et al., 2017, de Pater et al., 2016] have provided detailed insights in the longitudinal variations. There are however a few reasons, which complicate the inclusion of this level of detail. First, the radio-hot spots are local depletions of ammonia that drift inside the atmosphere. The drift velocity and direction are determined by the dynamics of the upper atmosphere and as a consequence, the locations vary on time scales of days [Cosentino et al., 2017], rendering the extrapolation of the locations over large time scales infeasible. The lack of concurrent images during the Cassini flyby, therefore, does not allow to determine the longitudinal average sufficiently to justify inclusion. Secondly, the longitudinal variations occur on much smaller scales than the latitudinal variations as seen in the radio maps by [Cosentino et al., 2017, de Pater et al., 2016, Fig.2,Fig. 1]. Since the size of the Cassini beam is large compared to the scale of these variations, the beam effectively averages the longitudinal structure.

Zonal deviations resolve variations of the ammonia abundance with latitude and are always presented as the difference from a uniform limb-darkened disk. High-resolution interferometry observations with sufficiently small beam size are capable of resolving such variations. The synthetic beam of the VLA, for example, offers a high enough resolution to capture these variations and, therefore, is the basis for the retrieval of this brightness signal. Before the averaged quantities are presented, the reader is cautioned that the inclusion of the zonal structure is based on the assumption that these structures do not vary with time. Especially the Southern Equatorial Belt (SEB) is known to disappear in irregular intervals [Sanchez-Lavega and Gomez, 1996] in optical images, however, at the time of Cassini observations, the SEB showed no signs of abnormal activity. Also, the correlation between visible and mircowave changes in atmosphere are not well understood and an active area of research. Nevertheless, to limit the impact of temporal changes, two different measurements were used and compared.

The first set of observations stems from VLA measurements of July 2000. In terms of time, these maps are the closest interferometric high-frequency measurements of Jupiter. Jupiter was observed at three different frequencies 15, 22.4 and 42 GHz to recover information on the atmospheric mixing ratio of ammonia. Especially the 15 GHz measurements are the most relevant for this research. The details of the data reduction of the VLA2000 maps are explained in Appendix A. The longitudinal structure was obtained by applying the Sault et al. [2004]-algorithm and and the data then reduced using the same method as the 2016 maps [de Pater et al., 2016]. The resulting maps are longitude resolved residual brightness temperature. Retrieving the zonal structure structure from these maps required further data reduction. In summary, the raw maps were cleared of residuals based on the effective resolution of the maps, where measurements below a threshold resolution were rejected. This approach removes artifacts that are present at the edge of the maps, where the resolution is poor. The cleaned maps were corrected for a uniform limb-darkened disk, and the quantities were averaged over all longitudes to retrieve the zonal profile.

The second set of observations is taken from high-resolution images obtained by de Pater et al. [2016]. Jupiter was observed with the VLA taken over its full spectral range (4GHz to 18 GHz) to probe the top layer of the atmosphere. By using radio spectral imaging, the researchers were able to reconstruct radio maps with an unprecedented longitudinal resolution at nadir. The zonal structure, as presented in their supplementary material, was obtained by subtracting a uniform limb-darkened disk with T_b = 161.86 K and p = 0.08 at frequency of 13.18 GHz. Since the measurements are averaged over 1 GHz frequency bins, the required brightness temperature was obtained by interpolating the zonal structure between the 13 GHz and 14 GHz bin, resulting in the approximate residuals at 13.78 GHz.

The two zonal profiles can be found in Figure 4.5, where the red line denotes the 2000 scans and the blue-dotted line is taken from the 2014 scans [de Pater et al., 2016]. Overall, the main features compare well between the two different scans, confirming little time variability the scans. The main difference between the two curves can be attributed to the resolution, as seen by the varying degree of details in the two scans. The blue dotted line resolves smaller features, especially at the mid-latitudes, whereas the low resolution of the 2000 scans smoothens the curve. This effect is also seen when comparing the brightness anomaly of the NEB (at 0.2 R), where the lower resolution of the 2000 scans effectively suppresses the peak brightness while increasing the spatial extent.

The last step consists of interpolating this structure onto the base model. Whereas the NS limb darkening is already included when the zonal deviations are presented, the EW component requires adjustment. It is assumed that the zonal variations fall off with the same coefficient as the uniform brightness model so that the zonal structure was adjusted using p = 0.08.

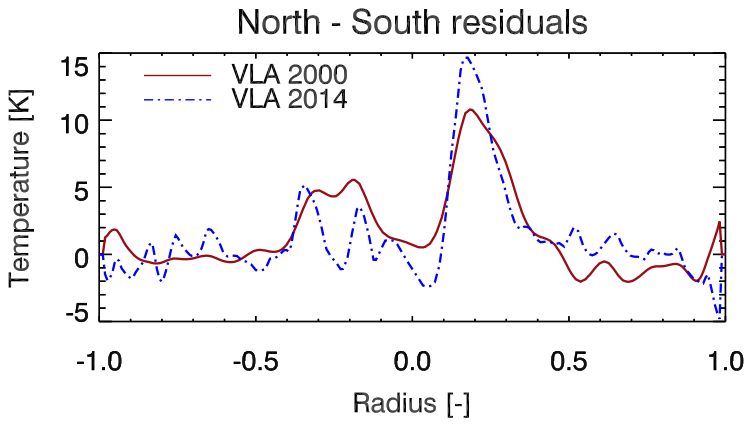

Figure 4.5: Comparison of the zonal radio anomalies as obtained by two different VLA scans with different resolution.

The third brightness model is based on the Berkeley Jupiter radiative transfer code as developed in 1991 [de Pater et al., 1991], updated based on new measurements and used after that in many atmospheric studies, such as [de Pater et al., 2001, de Pater et al., 2016]. The model includes the absorption of major atmospheric species in the upper atmosphere (NH_3, H_2, H_2S and H_2O), where the abundance of the volatiles can be varied with depth, testing for several depletion/enhancement scenarios. The model as used in this calculation uses solar abundances for the major species.

The impact of the brightness model can be studied by comparing retrieval based on different brightness models.

4.5.3. Cosmic Microwave Background

The Cosmic Microwave Background is the earliest signal that we receive from the Universe and has been extensively studied (see Durrer [2015], Fixsen et al. [1996] for a review of the CMB - science). Variations in the CMB give insights into the distribution of matter in the hot and young Universe. These fluctuations are very small ($\sim \mu$K), and can be safely ignored for our research. The CMB emission resembles a near perfect blackbody at a physical temperature of 2.73 K.

In radio astronomy, radiation is generally expressed as an equivalent brightness temperature in the Rayleigh-Jeans limit. This brightness temperature has the advantage of being additive so that several sources can be represented as superimposed individual sources, a useful property when observing Jupiter and its radiation belts. Starting from Planck's law of blackbody radiation,

$$I_\nu(T) = \frac{2h\nu^3}{c^2} \frac{1}{e^{h\nu/kT_p} - 1} \tag{4.12}$$

h $[Js]$ Planck's constant, 6.626069E-34

c $[m/s]$ Speed of light

k $[J/deg]$ Boltzman constant, 1.380E-23

ν $[Hz]$ Frequency

$\boldsymbol{T_p}$ $[K]$ Physical temperature, thermodynamic temperature

where the exponent in the denominator can be expanded for small frequencies ($h\nu \ll kT$) to obtain the Rayleigh-Jeans approximation:

$$I_\nu(T) = \frac{2\nu^2}{c^2} T_b \tag{4.13}$$

It is important to understand the difference in the two temperature at this point, T_p and T_b. The physical temperature, T_p, refers to the temperature that a perfect blackbody would have to emit the recorded intensity. The measured intensity, when converted to an equivalent temperature in the Rayleigh-Jeans approximation

is given by the brightness temperature, T_b. As long as the frequency is sufficiently small, these two temperatures are equal, and these two temperatures are often used interchangeably in the literature. Considering the case of the very dim CMB radiation as seen in Figure 4.6, one can see that at the Cassini frequency the Rayleigh-Jeans approximation as given by the red curve, is diverging from the Planck's radiation curve. As a consequence, the equivalent brightness temperature has been scaled to account for the deviations. This is done by equating the two intensities and finding the relation between the two temperatures at the given frequency and solving for T_b:

$$\frac{2k\nu^2}{c^2}T_b = \frac{2h\nu^3}{c^2}\frac{1}{e^{h\nu/kT_p}-1} \tag{4.14}$$

$$T_{b-CMB} = \frac{h\nu}{k}\frac{1}{e^{(h\nu)/(kT_P)}-1} \tag{4.15}$$

For a physical temperature of T_{CMB} = 2.73K, the equivalent Rayleigh-Jeans brightness temperature at Cassini's operating frequency is T_{b-CMB} = 2.41 K. This result is in line with values as observed by WMAP [Page et al., 2003] and as used in Jovian radio astronomy before [Gibson et al., 2005].

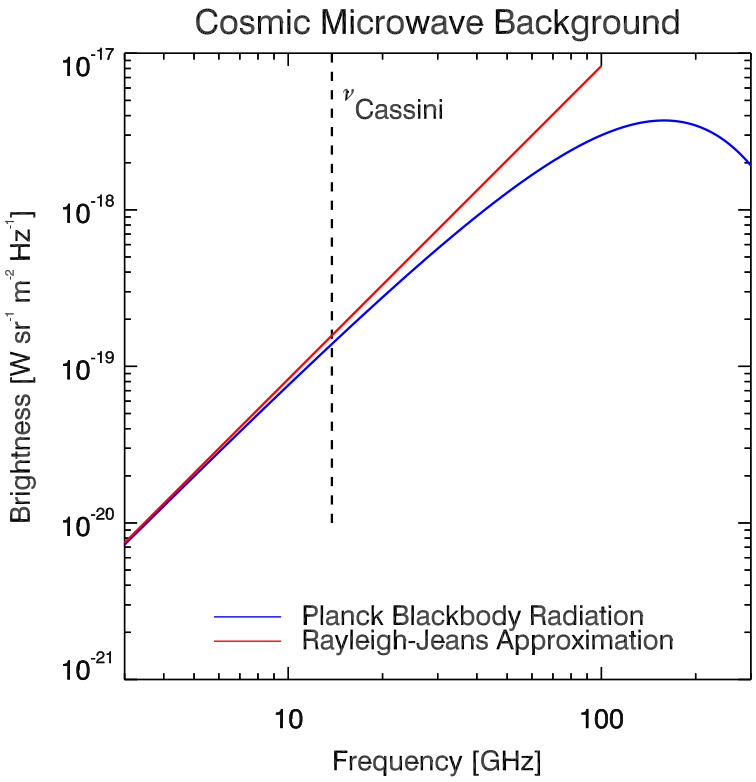

Figure 4.6: Comparison of the CMB radiation as expressed by the Rayleigh Jeans approxmations (red curve) and the Planck's blackbody equation (blue curve). Note the difference at the Cassini frequency.

4.6. A-priori Calibration Algorithm

In its basic form, the radiometer records the current in the antenna, as it is moved across the target. The current is dependent on the brightness of the source, which is the ultimate goal to be recovered. For the inversion of the antenna current to brightness temperature, the instrument must be calibrated against known signals, ideally a strong radio emitter ("hot target") and weak radio emitter ("cold target"). This section is based on the radiometer theory as touched upon in Chapter 2, and details how the calibration algorithm was applied to the Jupiter scans.

Recalling that in the microwave region, the antenna's current is linearly dependent on the brightness temperature, two reference sources with pre-established brightness temperature are sufficient to establish the relationship between measured signal and brightness temperature. Whereas this works in principle well, a few constraints do not allow this algorithm to be applied for the Cassini scans. Two of the main reasons are:

- Ideally the reference temperatures are in the vicinity of the spacecraft, to minimize the required slew of the spacecraft. Excessive motion of the spacecraft is fuel intense and reduces effective target observations time. Additionally, a reorientation of the spacecraft changes the immediate environment of the spacecraft and can lead to differential heating of the spacecraft and change the gain performance of the system.
- The radiometer is known to drift on short time scales due to changes in environmental conditions, such as temperature in the components. Large intervals between calibration observations are, therefore, prone to instrument effects and increase the uncertainty in the retrieval.

Due to the lack of other strong radio emitters in the vicinity of the Jupiter system, the internal reference load with known resistance was used as the hot target. As explained in Chapter 2, a single observations cycle of 1 seconds consists of a 35 μ s reference load observation to track the relative gain, and the remainder is dedicated to integrating the Jupiter radio emission [West et al., 2009]. Conveniently, the empty sky serves as an excellent cold target due to its stable cosmic microwave background (CMB) radiation with a blackbody temperature of 2.7 K and an equivalent brightness temperature of 2.4 K [Gibson et al., 2005, Page et al., 2003]. Recalling that the antenna is sensitive to a region of the sky, an ideal cold sky reference is obtained as far away from strong radio emitters as possible to limit the contamination of the signal from the sidelobes. The raster scans extended outwards to $\pm$ 3.5 R_J from Jupiter's center, an effective trade-off between target observations and quality of the signal. If the calibration targets were moved further out, the cold sky reference would improve, however, the time for the individual scans would increase due to the larger region in the sky that the instrument must cover. Contrary, moving cold target observations further inwards, allows for a better temporal sampling of the planet, but the quality of the cold sky reference would be decreased due to an increased sidelobes contribution. The current setup allows for a calibration scan every 5 minutes when the beam has reached the turn - around point as seen in Figure 4.4. This time exceeds the measurement stability of 100 seconds as estimated by [West et al., 2009].
Furthermore, the above procedure requires ideal instrument performance including a main beam with near unity beam efficiency. Unfortunately, the radio antenna was designed primarily for ground communication purposes, and therefore not optimized for the RADAR operation. The design deficiency resulted in large sidelobe contribution, which dilutes the signal unless excellent knowledge of the beam is established. The calibration algorithm of Cassini RADAR 3 was, therefore, adapted to accommodate the deficiency. Instead of absolute calibrating the instrument, the new algorithm relied on a priori estimate of the instruments quantities and quantified these uncertainties when calibration targets were available.

The algorithm relies on the following apriori estimates:

$\boldsymbol{T_{rec}}$ = 550 $[K]$ Receiver noise temperature, the noise temperature when the antenna is idle. This system temperature is assumed to be constant, and repeated measurements at Titan have shown excellent stability [Janssen et al., 2016].

$\boldsymbol{T_{rl-nominal}}$ = 300 $[K]$ Nominal temperature of the resistive load

$\boldsymbol{g_{norm}}$ = $(T_{rec} + T_{rl-nominal})/262000$ $[K/counts]$ Normalizing constant for the raw gain, based on ground-based measurements, so that measurements of an ideal resistive load with $T_{rl-nominal}$ would result in 262000 counts.

$\boldsymbol{cal}$ = 1/206.2 $[K/counts]$ Calibration constant, adjustment for the waveguide noise contribution. This constant changes with wave guide temperature, and is dependent on the illumination conditions. This parameter can be obtained during the warm-up phase of the instrument by observing a hot target continuously.

$\boldsymbol{a}$ = 0.8 $[-]$ Attenuation of signal when propagating inside the instrument.

The operation of the radiometer has shown that the gain of the system is tracked accurately by the internal reference load [Janssen et al., 2009], reducing the effect of gain drift between calibration measurements. Two

points are required to establish the slope the radiometer equation. The first point is provided by the antenna count when observing the resistive load, C_{rl} and a corresponding physical temperature read out from a sensor, T_{rl}. The temperature of the resistive load is kept nearly constant at 303.3 K ± 0.1 K. This temperature is very close to the reference measurements of 300 K as used for g_{norm}. The second reference point is given by the receiver noise temperature, T_{rec}, the theoretical temperature at which the antenna counts would be zero. After normalizing the gain, the gain is close to unity. Note, that the normalization also remedies the impact of the apriori estimate of T_{rec}, as the ratio of temperatures:

$$\frac{T_{rec} + T_{rl-nominal}}{T_{rec} + T_{rl}}, \tag{4.16}$$

effectively reduces the impact of the term. The linear antenna gain follows then:

$$g = g_{norm} \frac{C_{rl}}{T_{rec} + T_{rl}} \tag{4.17}$$

g $[counts/K]$ Radiometer gain

In a stable temperature environment, changes in the count on the resistive load indicates a change in gain. This expression simultaneously allows for operation during the warm-up of the instrument, when changes in internal temperatures of the components are captured by the temperature sensor at the resistive load. The read out from the temperature sensor and the count on the sky are prone to measurement noise, which should be removed to avoid contamination of the signal. The best indicator of the magnitude of this measurement noise comes from observations of the empty sky. In the absence of other strong radio emitters in the vicinity, the empty signal should constitute a flat empty sky signal. Consequently, any fluctuations observing the empty sky are indicative of measurement noise propagating into retrieval. Assuming that the measurement noise is purely Gaussian, averaging the gain will remove the noise contributions. Figure 4.7 shows the root mean square (RMS) of the retrieved empty sky signal for different averaging periods, N_{ave}, indicating a steep fall off with averaging length. The curve is leveling out around 50 seconds, to be conservative 100 seconds was chosen as the appropriate value. Even longer averaging periods are not advisable as they would interfere with the primary task of the reference load to track changes in the gain.

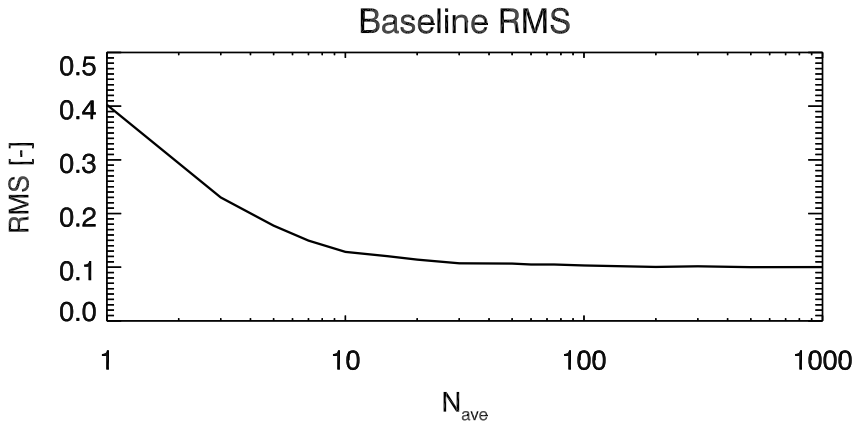

Figure 4.7: Root mean square of the retrieved empty sky signal for various averaging periods of the gain. The optimum was found at 100 seconds.

The total power that is received by the radiometer is a composite of the sky's signal, and internal noise contribution, P_sys. Using the definition of the antenna as matched resistor [Janssen, 1993], the total power, can be represented by the sum of equivalent temperatures, T_{sky} and T_{sys}:

$$T_{total} = T_{sky} + T_{sys} \tag{4.18}$$

The system temperature is determined by the receiver noise temperature (noise power defined at the radiometer) and the low noise amplifier temperature (noise power defined at the antenna plane). The low

noise amplifiers signal travels first through feed lines to reach the radiometer so that its signal is attenuated by the feed line loss, a. The final expression is scaled back to the antenna plane and is given by:

$$T_{sys} = \frac{1}{a}\Big((1-a)T_{LNA} + T_{rec}\Big) \tag{4.19}$$

The preliminary antenna temperature, $T_{a_{pre}}$, is obtained by applying the gain to the sky count and subtracting the estimated system noise temperature.

$$T_{a_{pre}} = \frac{cal\, C_{sky}}{g} - T_{sys} \tag{4.20}$$

At this point, the antenna is not absolutely calibrated. Three additional steps are required to achieve absolute calibration.

Gain drift and correction factor As the instrument is exposed to the harsh space environment, the components are slowly degrading in performance. Titan has a very stable temperature environment, a combination of a thick atmosphere and low orbital eccentricity of Saturn, serving as a stable calibration target. Repeated observation of Titan over the course of the mission have allowed for quantifying the annual drift g_d of the radiometer [Janssen et al., 2009, 2013, 2016]. Table 4.2 lists the best fit for the gain drift, assuming a constant brightness temperature of Titan. The decrease in gain drift is most likely due to a more robust fit and does not represent an actual deviation from the linear gain drift. The gain drift as identified from the latest Saturn measurements is the most applicable, and therefore chosen for this analysis as seen by the green shaded column in the table. Additional to the gain drift, the calibration has to be corrected for (i) internal inconsistency based on the comparison between maps; and (ii) for distortion of the real brightness of Titan due to its atmosphere. The correction factor amounts to F_{corr} = 0.9670 [Janssen, 2016, personal communication].

$$T_{acorr} = T_a\big(1 + g_d\, t\big)F_{corr} \tag{4.21}$$

	2009	2013	2016	2016
Drift: g_d	-0.0044	-0.004	-0.003	-0.0022
Epoch	1. Jan. 2004	1. Jan. 2004	1. Jan. 2004	11. Aug. 2009
Target	Titan	Saturn	Saturn	Titan
Source	[Janssen et al., 2009]	[Janssen et al., 2013]	[Janssen, 2016, personal communication]	[Janssen et al., 2016]

Table 4.2: Gain drift evolving over time. The green shaded region represents the absolute calibration that is used for this research.

Note, that the adjustment factor is smaller than 1, indicating a decrease in measured antenna temperature of roughly 5%. The lower sensitivity of the antenna over time, therefore, causes the gain factor to increase with time.

4.7. Convolution

The contribution of the thermal emission to observations is a compound of the brightness model of Jupiter as introduced at the beginning of the section and the antenna's sensitivity to radiation in the sky, the beam shape. The beam shape acts as a weighting function for the incoming radiation. The convolution requires excellent knowledge of Jupiter's position inside the beam frame, and the fine structure of the beam. Mathematically speaking, this contribution is the convolution of the normalized gain with the brightness distribution in the sky. Note, that this requires a transformation of the brightness model into the same coordinate system at the beam or vice versa. The convolution is given by:

$$T_m = \frac{\iint T_b(\theta,\phi)G(\theta,\phi)d\Omega}{\iint G(\theta,\phi)d\Omega} \tag{4.22}$$

By simulating the antenna temperature and by merging all uncertainties into the simulation process, the project can best be described by the forward approach. The basic idea revolves around reproducing the observations conditions as accurately as possible. The mismatch between the observations and the simulation is then attributed to the synchrotron radiation.

In theory, the synchrotron radiation could then be obtained by:

$$T_{sync} = T_a - T_m \tag{4.23}$$

4.8. Sidelobe Contribution

The last step in the analysis is removing the errors that were introduced by the a-priori estimates through the baseline subtraction. Recalling that Jupiter always remains within the near sidelobes, and the Jovian thermal emission is leaking in through the sidelobes even when the beam is far from the center. The antenna temperature is, therefore, always higher than that expected from a pure CMB signal. This effect is noticeable in the calibrated antenna temperature when analyzing the measured signal at the turn around points. Whereas the signal is small when the beam is at the corners of the scan region(~ 0.6K), the contribution reaches 1.5 K, when the beam is crossing the equatorial plane. The difference is shown in Figure 4.8, where the black line is the brightness temperature of CMB, and the red lines correspond to the simulated antenna temperature and a positive value of the signum plot indicates where the baseline reference is obtained. A zero value of the signum plots indicates the main beam is too close to the planet to obtain a baseline estimate. The small variations in the modeled antenna temperature at the baseline locations are due to the vertical motion of the beam at the turn around point and a sign of the excellent knowledge of the beam shape. At this point, it becomes clear that this approach is iterative in nature. The subtraction requires a thermal model of Jupiter, which is one of the quantities that is further constrained using the observations. The presented problem is best resolved through repeated subtraction and updating the brightness model based on the residuals of the previous iterations.

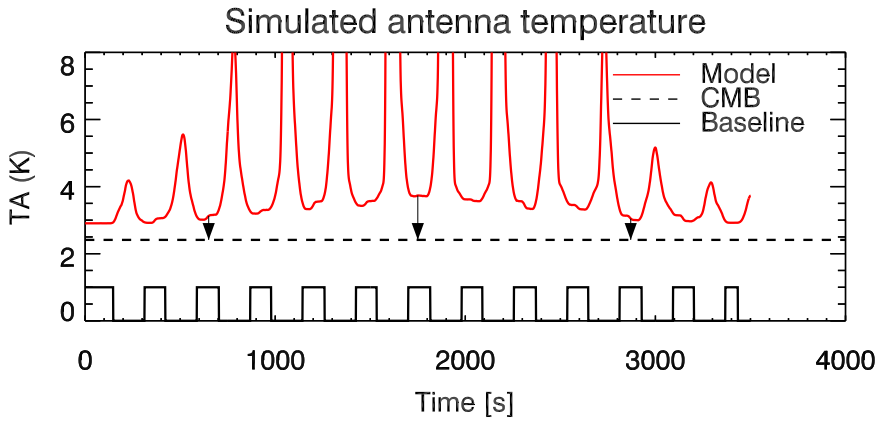

Figure 4.8: Simulated antenna temperature for a given scan. The difference between the CMB brightness temperature and the simulated antenna temperature indicates the sidelobe contribution, that has to be corrected for in the baseline subtraction. The arrows show the amplitude of the sidelobe contribution for three locations.

4.9. Baseline Subtraction

The uncertainties to first order affect all measurements similarly, the method of differencing removes these uncertainties. Assuming perfect knowledge of the reference point, the target observations can be made accurately relative to the reference observations. The CMB radiation is an ideal target for the reference target due to its uniform distributions. The sky count when observing the CMB, N_{CMB} is, therefore, subtracted from the sky count:

$$\Delta T_a = \frac{cal}{G(t)} N_{sky} - T_{sys}(t) - \left(\frac{cal}{G(t)} N_{CMB} - T_{sys}(t) \right) \tag{4.24}$$

Note, that the gain and the system temperature fluctuations are very small, as the fluctuations in the reference load and the low noise amplifier are small themselves. In this retrieval, these fluctuations were taken into account, however, for an analytic demonstration, these fluctuations are assumed to be negligible between the two measurements.

$$\Delta T_a = \frac{cal}{G(\bar{t})}\left(N_{sky} - N_{CMB}\right) \tag{4.25}$$

The baseline subtraction is visualized in Figure 4.9, where the green line indicates the uncorrected antenna temperature. The signum plot in black indicates the times that the baselines were subtracted, where a non-zero value corresponds to the beam at the turn-around point and thus the designated location for the subtraction. For lack of better resolution, the baseline is interpolated between the evaluation points and its magnitude is shown by the orange line. As a consequence of this approach, the residuals off the limb are centered around zero.

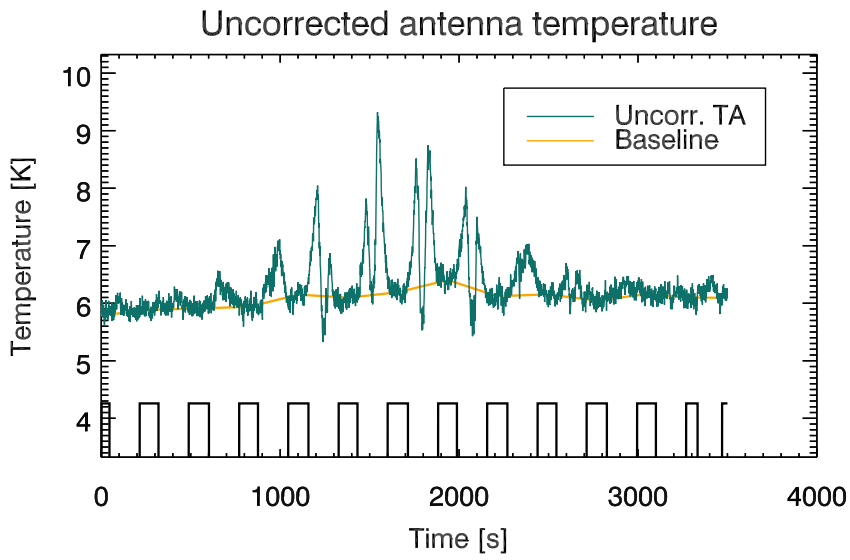

Figure 4.9: Example of temperature structure after Jupiter's contribution has been removed. Short term gain drift can be seen by the small flucuations in the orange base line cruve. This gain drift is removed by using the orange line as the cold sky reference, or in other words, only the signal is measured with respect to the orange curve. The signum plots indicates the periods where the zero subtraction is performed.

Since the observations are made relative to the CMB brightness, the final calibrated antenna temperature is then obtained by adding the brightness temperature, T_{CMB}.

$$T_a = \Delta T_a + T_{b-CMB} \tag{4.26}$$

The result at this point is the time-sorted residual antenna temperature as seen in Figure 4.10. Clearly visible is the double peaked structure of the synchrotron corresponding to the main emission lobes next to the planet. Close to the equator the emission is maximum, with a decreasing signal as the beam is moving away from the equator. Note that the colors corresponds to the beam location as given in Figure 4.4 This temperature represents the average brightness temperature of the synchrotron radiation in the main beam, and not the actual brightness temperature of the sky. For comparison with other observations, it is important to keep in mind that the relatively large beam averages the signal over a larger region, so that the synchrotron radiation appears less intense at the peak locations, however, more spatially extended. It also worthwhile mentioning that the total flux density is conserved through the convolution process.

The question remains, how the apriori estimates influence the antenna temperature. Returning to the simplified analytic solution Equation (4.24), one realizes that the receiver noise temperature T_{rec} influences

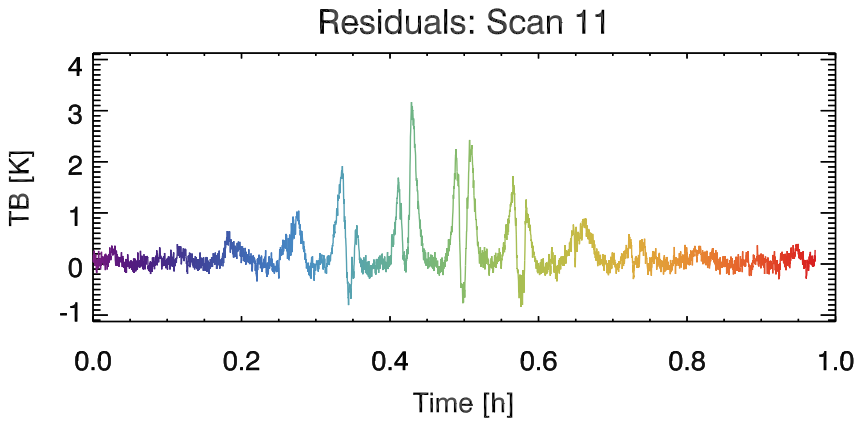

Figure 4.10: The example of the calibrated antenna temperature over the course of one scan. The colors corresponds to the location in Figure 4.4.

both the gain and the system noise temperature. The impact on the former is reduced by normalizing the gain, the impact on the later is reduced through the differencing process. Assuming that the system noise temperature fluctuates around a common mean, only short term variations remain and its contribution to the calibrated antenna are very small.

4.10. Flux Density

The synchrotron radiation after the model subtraction is in the units of antenna temperature. The relationship between brightness temperature and antenna temperature might appear simple, however, requires careful consideration. For sources larger than the main beam of the antenna, the relationship is simply given by:

$$T_a = T_b \tag{4.27}$$

For sources that are smaller than the main beam information on the source and beam solid angle are required [Marr et al., 2015]:

$$T_a = T_b \frac{\Omega_s}{\sqrt{\Omega_s + \Omega_{beam}}} \tag{4.28}$$

In the synchrotron radiation case, the source region is very loosely defined, complicating the definition of the appropriate solid angle. Since the main beam is tracing out the main emission region, the first definition is applicable, even though at the extreme corners of the scan region, the synchrotron brightness temperature appears weaker than in reality.

The relationship between intensity and brightness temperature is given through the Rayleigh-Jeans approximation. At first glance, one might assume that the Rayleigh-Jeans approximation is not applicable for the given conversion due to the weak brightness temperatures involved in the retrieval. Recalling, that the brightness temperature functions as a scaling of the intensity, it can be used as long as all sources in the system are expressed in equivalent brightness temperature. Mixing up equivalent brightness temperature and physical temperatures of blackbody can distort the analysis and should be avoided.
The Rayleigh-Jeans approximation as given by Equation (4.13) includes a factor of two. This factor is introduced to account for the polarization loss factor, $cos^2(\theta)$, which describes the efficiency at which a linearized antenna is picking up radiation. When the antenna's linear plane is aligned with the polarized signal, it is picking up the full intensity. With increasing angle between the antenna and polarization plane, the efficiency drops. This relationship is valid for unpolarized emission, where the intensity is evenly distributed between vertical and horizontal polarization and regardless of the orientation the antenna picks up half of the signal, hence the factor of two to quantify the total radiation. This assumption, however, does not apply to radiation that is preferentially polarized, such as synchrotron radiation that has a ~ 22% horizontally polarized component. To recover the total intensity from such a source, it is sufficient to measure at two orthogonal polarization, abbreviated by v (vertical) and h (horizontal). Each polarization picks up the pro-

jected polarization, and the combined signals from both polarization give the total intensity, where the factor of two is dropped to account for the polarization:

$$I_v = \frac{k\nu^2}{c^2} T_{b_v} \tag{4.29}$$

$$I_h = \frac{k\nu^2}{c^2} T_{b_h} \tag{4.30}$$

The total intensity, I_t is then given by the sum of the two polarized components:

$$I_t = I_h + I_v = \frac{k\nu^2}{c^2} \left(T_{b_h} + T_{b_v}\right) \tag{4.31}$$

Ground-based measurements report on the synchrotron radiation in units of flux density, so that the units of antenna temperature have to be converted into flux density. Flux density is defined as the spectral intensity integrated over the source region:

$$S_t = \iint I_\nu d\Omega_s = \frac{k\nu^2}{c^2} \int_0^\theta \int_0^{2\pi} T_b\theta, \phi sin(\theta) d\theta d\phi \tag{4.32}$$

Note that the solid angle in the above equation refers to the solid angle that the source extends. Contrary, the flux density that is entering through the main beam is defined by

$$S_{beam} = \iint I_\nu d\Omega_{beam} \tag{4.33}$$

This first definition is used when calculating the total flux that is received from the source, whereas the second definition is often used when constructing synchrotron radiation maps.

The integration of the source region requires again a description of the source. Common approaches quantify the thermal noise level and integrate the signal above this level. Due to the baseline subtraction, the far emission is fluctuating around zero. Integrating white noise centered around zero results in an overall zero contribution, so that inherently the thermal noise contribution should cancel out.
A more intuitive approach is calculating the total emission and projecting it onto the disk of Jupiter. In this approach, the solid angle of the source is simply given by Jupiter's disk and the signal is easily expressed as a fraction on top of Jupiter's thermal emission.

4.11. Pointing Accuracy

The convolution process requires excellent knowledge of the position of Jupiter in the beam frame of RADAR 3. Initial simulation results confirmed the presence of an offset of the beam shape from the spacecraft z-axis as reported before Bolton et al. [2002], Janssen et al. [2001], Zhang et al. [2017] and suspected by the RSS radio occultation team. The problem is further complicated by the fact that high-level requirements on pointing knowledge [Pilinski and Lee, 2009, Table 3] are two orders of magnitude larger than the required level of sensitivity. Whereas the instrument was designed to have a pointing knowledge of better than 1 mrad, the retrieval is sensitive to changes on the order of 10 μrad. This level of sensitivity was established by varying the beam offset and determining the level at which there are discernible differences in the residual structure of the synchrotron radiation. Variations below the 10 μrad level have no noticeable effect on the residuals. The actual pointing knowledge of Cassini is better than the requirements stipulated above Pilinski and Lee [2009]. As detailed in the paper, the pointing stability nominally outperforms the pointing knowledge requirement with a significant margin, so that the stability is on the order of μrad. Extensive tests with Cassini RADAR confirmed that this is a rather optimistic estimate and there are strong indications for variations in the pointing. This could partially be attributed to the early nature of the observation in the Cassini mission, and the analysis as presented by Pilinski and Lee [2009] reports on later improved efforts.

Beam offset The beam direction is defined by its boresight, the location of its maximum sensitivity. The design case foresees that the beam is pointed in the negative z-direction in the Cassini spacecraft frame (SC), i.e. the boresight is given by [0,0,-1]. Due to manufacturing imperfections and uncertainties during the beam calibration, the beam is offset and given by angular offset [dx,dy,dz]. The z-component is a consequence of

the rotation of the boresight vector and should not be seen as a physical offset. In practice, the retrieval is insensitive to the z-offset, so that it is assumed to be zero.

Oscillator drift Since the high-gain communication antenna was pointed at Jupiter, the data from the observations were directly stored on the onboard solid state recorder. The collected data includes the housekeeping data, such as information from the internal reference load, and also the integrated count on the sky for the given observation window [West et al., 2009]. The data are stored with the corresponding time stamp. Discussion with the Cassini Guidance and Navigation team [Burke, 2017, personal communication] has revealed that the onboard oscillator drifts about 0.5 seconds per day. Whereas post processing corrects for this drift in the spacecraft ephemeris, the recorded data are subjected to this drift. The time offset is co-aligned with the beam offset, however, depending on the scan direction, they are superimposed or act in different directions.

4.12. Optimization

Including the two parameters required for the thermal brightness model, the peak brightness at nadir, $T_b(0)$, and the limb darkening coefficient in the north-south direction, p_{NS}, the total number of uncertainties has increased to five. Notably, all uncertainties pertain to the subtraction of the thermal emission model. As established in Chapter 2, at these high frequencies the thermal radiation from Jupiter dominates the total emission, and the synchrotron radiation is just a small percentage of the signal. As a consequence, the retrieval is highly sensitive to uncertainties in the thermal emission. Only by constraining all five uncertainties simultaneously, the synchrotron radiation can be extracted with high confidence from the measurements.

An important factor to take into consideration is the time variability of these uncertainties. Naively, one may assume that the beam offset is constant over the duration of the full 20-h observation period. The strongest case can be made for the nadir brightness temperature, as longitudinal variations in temperature structure are small [Cosentino et al., 2017, de Pater et al., 2016] and thus no changes should occur. Regarding the limb darkening coefficient, less information on its longitudinal dependence are known due to the limited observation of the Jovian poles. Recent ground-based observations in the infrared indicate a similar consistent ammonia structure [Fernandez, 2017, personal communication].

Assuming perfect pointing knowledge, variations in the beam offset are unlikely as this would require a physical alteration of the antenna or the equipment. Uncertainties in the pointing knowledge of Cassini, however, will appear as variations in the beam offset and thus have to be taken into account. Assessing changes in the pointing uncertainty requires independent knowledge of the pointing, for example through the use of Doppler tracking or "point and stare" observation. The main problem with these measurements is that they are limited in their exposure time, The longest observations analyzed were 20 min timeframe, so that this constitutes the upper bound for that pointing variations [Pilinski and Lee, 2009]. If these variations can easily be extrapolated to longer time scales remains unknown. Lastly, the oscillator drift is tested against high precision on ground, and thus its drift is very well established with the 0.5 seconds per day.

Initial tests revealed that keeping the uncertainties constant for the full 20h period introduces large anomalies in the retrieved synchrotron radiation, strongly hinting at variations on smaller time scales. Naturally, one would want to resolve the uncertainties on the shortest possible time scale. This is not always possible, as the lower limit of resolvable time variations is set by solver; fewer data points reduces the robustness of the fit to the data. An intuitive compromise is given by the duration of a single scan with the 60 minutes, yet this is still 3 times above the level of variations constrained by the "point-and-stare" observations. The current solver, therefore, assumes that the variations are constant for a single scan. Should an offset drift occur on shorter timescales, they should introduce notable residuals in the synchrotron maps and, therefore, serve as first order test on the applicability of this assumption. Furthermore, difference between the solution for various scans can highlight the nature of the variations. Counterintuitively, large differences indicate a slow drift in uncertainties, whereas small difference hint at short time variations that cancel over the duration of the scan. Instead of constraining the uncertainties on a smaller time scales, it is better to understand the impact of these variations by studying the sensitivity of the integrated flux density to these variations, as presented in Chapter 5.

4.13. Monte-Carlo Markov-Chain

Solving simultaneously for the five uncertainties requires an appropriate solver. There is a wide range of solve available, from very simple grid-search to more advanced method such as genetic algorithms. Most solvers require a well-defined cost function to optimize for, a quantity that is very hard to define in the case of the synchrotron radiation maps. Ideally, the cost-function is an objective measure of the quality of the fit, this, however, begs the question what a good fit is. The more apriori knowledge on the synchrotron maps is introduced beforehand, the more the solution suffers from being over-constrained. The simplest approach would be finding an empirical solution, through the visual comparison of maps with ground-based observations. In this case, the uncertainties are selected based purely on the apriori knowledge on how the maps should look like. This approach, however, is very time-consuming and updates in the retrieval would require a new fit. Furthermore, it does not offer any quantitative insights into the sensitivity of the solution to the uncertainties. The genetic algorithm on the other hand offers insights only when the algorithm has converged, and thus are very inflexible when the cost function is poorly constrained. Only after the solution has converged, the cost function can be updated.

A more flexible approach is offered by the Markov-Chain Monte-Carlo (MCMC) [Geyer, 2011]. The Markov Chain offers the advantage of building updating its sampling from the solution space on the current level of knowledge. In practice, it establishes the unknown posteriori distribution based on an initial a priori and information collected while "walking" through the solution space. In simple terms, the algorithm starts from an initial guess with a pre-defined a priori, in this case, information on how the uncertainties are spread. As it walks through the various possible combinations of uncertainties, it essentially starts exploring the solution space around this newly gained information. Thus, as the number of iterations grows the MCMC samples from this constructed a posteriori and reduces the impact of the a priori distribution.

4.13.1. Solution Space

The principle of the MCMC is best explained by exemplifying how it was implemented in the retrieval process. As stated above, first the a priori distribution of the uncertainties must be established, that is the possible range of the uncertainties. The larger the solution space and the finer the resolution of the uncertainties, the better the performance of the MCMC, however, at the expense of computing time and power. The final decision on the resolution and size of the solution space is a trade-off between required resolution and the computing power available to sample the solution space. The required resolution was determined from the level of sensitivity of the residuals so that a resolution step should not affect the integrated flux density by more than 3%. Another way to look at this is the sensitivity of the solution to a step in the solution space. Significant changes in the integrated flux density hint at low-resolution step, and require further refinement. The solution space is presented in Table 4.3, along with typical changes in integrated flux density in the vicinity of the optimum. Note that these sensitivity values are exemplary, and their behavior is more complex than presented here (for a more detailed discussion see the uncertainty analysis in Chapter 5).
The minimum and maximum value were obtained dynamically. The first optimization runs were set with a low resolution, therefore, allowing for a quick exploration of the solution space. When the uncertainties are far from the optimum solution, the synchrotron residuals reach unphysical values, e.g. large negative values, discontinuities in the signal structure. These early runs provided the information needed for reducing the solution space.

4.13.2. Cost Function

The MCMC requires information on how to advance inside the solution space. This metric, in optimization often referred to as the cost function, determines the quality of the solution. The metric is evaluated on the residuals antenna temperature of a single scan as seen in Figure 4.10. Early attempts used a simple cost function that analyzed the signal when the beam was far from the planet where the residuals should approach white noise. The quality of the solution, however, was poor, leading to a more complex expression that combines information from various points during the scan. This approach is not without disadvantages, as it requires a priori knowledge to evaluate the goodness of fit. The regions with strongest signals are shown graphically in Figure 4.11, the impact of the various parameters on the different regions is tabulated in Table 4.4, the logic behind the region is listed as follows:

1 When the beam is far from the main emission region, the structure should be pure white noise. Any

Table 4.3: Solution Space explored by the Markov-Chain Monte-Carlo

Uncertainty	Min	Max	Step	Sensitivitiy
T	160	163	0.20	3%
p	0.05	0.09	0.01	>1%
dt	0	0.5	0.1	1%
Scan 1 - 10				
dx	0.35	0.45	0.01	>0.1%
dy	0.50	0.65	0.01	>0.1%
Scan 11 - 20				
dx	0.30	0.40	0.01	>0.1%
dy	0.20	0.40	0.01	>0.1%

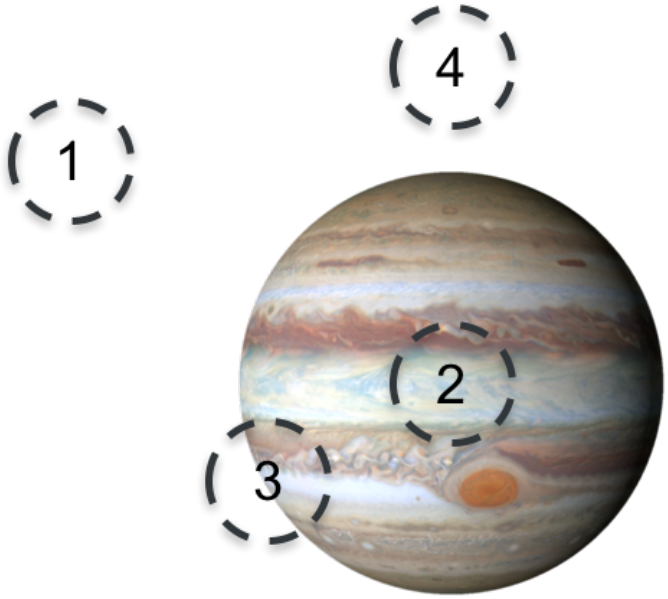

Figure 4.11: Regions of interest for evaluating the cost function. The various circle are exempalary beam footprints, where the numbers indicate the region.

residual signals in this region is an indication for a large beam offset. This is a helpful quantity to constrain the overall solution space, however, is quite insensitive to small changes in beam offset.
The quantity used is the root mean square of the residuals when the beam is further than 3 R_J away from the planet.

2 The synchrotron signal strength is dependent on the number of particles along the line of sight. Considering the observational geometry, when the beam is on the Jovian disk only a small number of the electron population is sampled. The signal from the side of the planet, where the line of sights passes through a significant fraction of the electron population, in contrast, is large. Therefore, the radiation minimum when passing the emission region should be in the vicinity of the center of the disk. The location of this minimum is mostly determined by x-offset in the beam and the time-offset; the depth of the radiation valley is controlled by Jupiter's brightness temperature.
In practice, the algorithm finds the locations of the minimum in front of the disk (one per disk crossing) and calculates the distances from the spin axis. The larger the distance from the spin axis, the further the solution is from the optimum. The second metric from this measurement is obtained from the absolute strength of this radiation, the larger the value at the radiation maximum, the larger the metric.

Table 4.4: Impact of the uncertainties on the cost function

Region	1	2	3	4
T	none	large	small	medium
p	none	none	none	large
dt	none	medium	large	small
dx	small	medium	large	small
dy	small	small	medium	large

Negative residuals in front of the disk indicate that the thermal brightness model is too strong, and are penalized; large positive residuals indicate that the Jupiter is too dim. Nevertheless, one has to be careful not to overconstrain this value, as a small fraction of the signal is expected in front of the disk.

3 The thermal emission from Jupiter comprises the majority of the signal. Moving the main beam off the disk of Jupiter results in a large drop in received power. In an ideal case, the signal when crossing the limb should be continuous, whereas spikes and discontinuities are strong indications for an offset. This signal, therefore, mostly controls the beam-offset and the time drift of the oscillator, as they modify the position of simulated Jovian thermal emission in the field of view of the antenna.
The algorithm identifies the measurement point closest to the limb crossing and stores the residual antenna temperature. The sum of all limb crossing then builds the basis for this metric. The larger the sum, the more likely is an offset of the simulated thermal emission.

4 Recalling the distribution of the synchrotron radiation, there should be no radiation coming from the vicinity of the poles of Jupiter. Any radiation from this region should be of thermal nature. The extended beam at these regions picks up radiation from the high latitudes of Jupiter, and thus effectively probes the ammonia abundance close to the poles. The limb darkening coefficient is a proxy for the ammonia abundance at the poles and therefore is the main factor controlling this signal.
The minimum radiation is expected when crossing the magnetic spin axis. The residual antenna temperature in the vicinity of this crossing immediately above the poles is summed and used for this metric.

The signal from the various regions must then be combined into a single metric, the compound cost function and the MCMC solver aims at minimizing this metric. Naturally, the metric strength differs between the various cases, and appropriate normalization must be applied to establish a robust cost function. The basis for the normalization is that in the vicinity of the optimal solution all four regions should have a similar impact on the cost function. At the optimum all metrics are designed to have ~ magnitude 3, where the factor 3 was chosen randomly, however, due to the normalization does not impact the result.
The various regions varied differently with changes in the solution space so that weights were applied to encourage the MCMC to converge to an optimal solution. The final choice of the weights was the output of a long process of fine tuning the algorithm:

- From Table 4.3 one can infer that the solution is very sensitive to the brightness of Jupiter. Therefore, the weight of region 2 was increased as it impacts all but the limb crossing and is crucial for controlling the magnitude of the thermal emission.

- Early retrieval attempts resulted in large residuals close to the poles. This effect prompted an increase in the importance of region 4, to understand the nature of this signal.

The breakdown of the metrics and the corresponding final weights are reported in Table 4.5.

Are these weights the final weights? Probably not, especially since perfect is the enemy of good! Nevertheless, the solution should not be sensitive to the various weights chosen in the process, which would amount to overconstraining the solution. The best way to counter this argument is showing by how the final solution does not differ drastically if different weights are applied. This assumption will be tested in the uncertainty analysis as presented in Chapter 5.

Table 4.5: Break down of the various components of the cost function. The normalization constant is applied to assure that all regions have a similar impact on the cost function. This is a consequence of the different nature of the regions, where the RMS is generally an order of magnitude smaller than the sum of residuals. The relative weights were than applied to force the MCMC to converge to the desired solution. The residual on the disk was found to be crucial in determining the proper flux density, so that a larger weight is required. The last column indicates typical magntidues that each region contributes to the compound cost function. The lower value is when the solution is close to optimum, the higher values indicates when there is a bad fit.

Region	Description	Type	Normalization	Relative weights	Typical Range
1	Off-limb residuals	Root mean square	25	1	3-4
2a	Distance to spin axis	Sum of distances	3	1	2-5
2b	Residuals on the spin axis	Sum of residuals	0.3	3	3-10
3	Limb-crossing residuals	Sum of residuals	1	1	3-15
4	Polar residuals	Sum of residuals	0.3	3	5-25

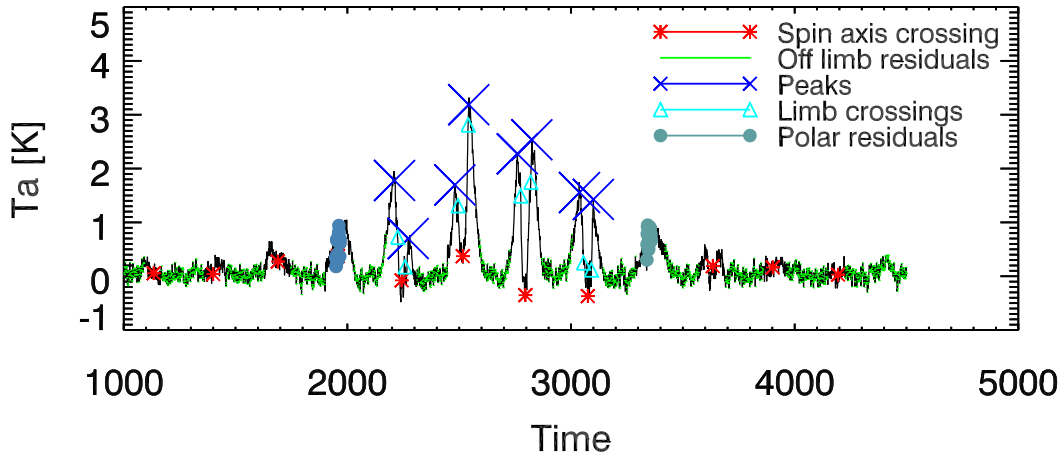

Figure 4.12: Residual antenna temperature for Scan 11. The various points are the regions of interest as identified by the algorithm. This is an example of a optimum solution for the given combination of uncertainties: dt = 0.1 [s], dx = 0.39 [mrad], dy = 0.57 [mrad], T = 162 [K], p = 0.05 and the corresponding value of the cost function is 28.99. The red stars indicate the crossing of the magnetic spin axis, and corresponds to a minimum when crossing the disk. The magenta cross indicate the value when crossing the limb and do not conincide with the radiation peaks as identified by the blue crosses. The polar residuals shown by grey dots, and should be relatively small.

4.13.3. Random Walkers

At this point, the MCMC can be initiated. The chain is started at an initial position and evaluates the cost function. The chain then starts "walking" through the solution space and evaluating the cost function for the given set of uncertainties (see Figures 4.12 and 4.13 for a good fit and a bad fit). At any time, out of the set of five uncertainties, only one uncertainty is changed for calculating the metric of the updated position. Once the algorithm has decided which uncertainty to alter, the magnitude of the uncertainty is chosen randomly based on the best knowledge of the distribution of uncertainties. In the beginning, the values are drawn from a normal resolution centered around the a priori, our best understanding before the analysis. As the number of iterations grows, the algorithm develops a better understanding where the optimal solution is located, and this information is combined into the posteriori. Simultaneously, the a prori loses importance and is taken over by the posterori. With time this approach encourages the solution to preferentially explore the region in the surroundings of the optimum. At the same times, this method builds up a posteriori distribution that can be used for studying the uncertainties in the process.

The second feature of the algorithm evolves around the transitional probabilities. To understand the importance of the factor the concept of local and global extremes has to be touched upon. Using the minimum cost function as an example, there exists only one point in the solution space that has the lowest magnitude, however, there exist several points where the magnitude is lower than in local region, hence a local minimum. Most simple optimization algorithms are exposed to the risk of converging to a local minimum. To avoid that

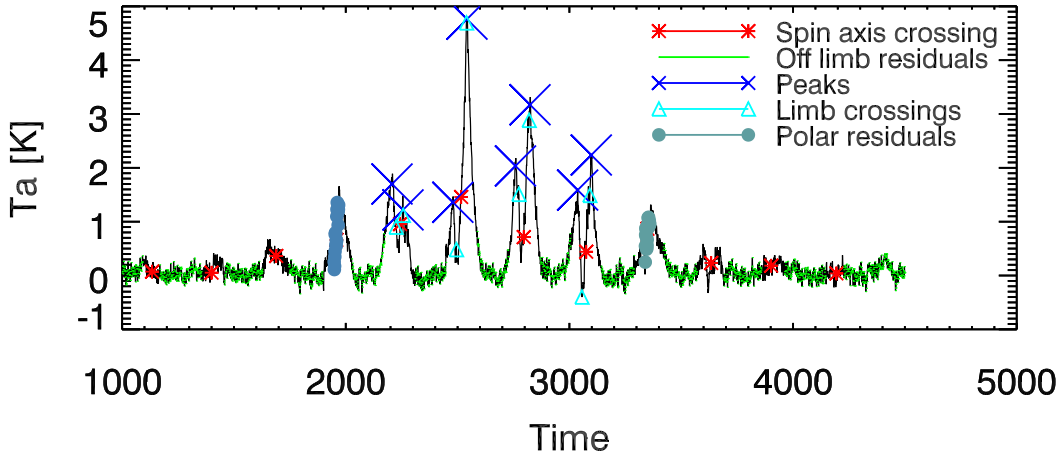

Figure 4.13: Residual antenna temperature for Scan 11. This is an example of a bad solution for the given combination of uncertainties: dt = 0.3 [s], dx = 0.41 [mrad], dy = 0.57 [mrad], T = 160.5 [K], p = 0.05 and the corresponding value of the cost function is 42.49. The location of the spin axis are offset from the radition value in an alternating fashion, indicating a time offset. The limb crossing (magenta triangles) conincide with the synchrotron peaks indicating an beam offset. Lastly, the radiation residuals on the disk are large, indicating that Jupiter's brightness temperature is not adequate.

an algorithm gets stuck at a local minimum, the MCMC is designed to not always continue in the direction of the minimum cost function; rather the transition probablity is evaluated based on the magnitude of the cost function at both points. The probability of advancing to the next step, P(i+1) is given by the fraction of the cost function, at the current position CF_i, and at the proposed next step, CF_{i+1}:

$$P(i+1) = \frac{1 - CF_{i+1}}{CF_{i+1} + CF_i} \tag{4.34}$$

The smaller the cost function at the proposed next points, the larger is the probability of advancing to the next point. However, there is still a chance that this step is rejected and the random walkers continue in a different direction.

A few further tweaks are implemented to increase the robustness of the MCMC. The algorithm is set up to explore five points around the current position, but only by changing one given variable. The transitional probability is then obtained by comparing the cost function at each of the 5 points. In case all five proposed points have been computed already, the MCMC is forced to jump to a different position in the solution space, by drawing randomly from the a posteriori distribution. This hinders the MCMC from converging to a local minimum and increases the chance of solving for the global minimum.

This process is started for all 20 scans, and the a posteriori distribution of the uncertainties of the previous scans are passed as a priori distributions of the following scan. This has the advantage of speeding up the process under the reasonable assumptions that the uncertainties do not differ drastically between scans. Note that the rotation of the spacecraft also results in a rotation of the relevant reference frame. To avoid inconsistencies, the MCMC was run seperately on both sets of polarizations.

The number of samples to be evaluated depends on the size of the solution space. The problem with multi-dimensional spaces is that they grow very quickly, making a full exploration of the space infeasible. Even partial coverage of the solution space seems unlikely considering the total number of 66000 possible combinations as presented in Table 4.3 and roughly 15 seconds computing time per retrieval. Sampling from the a posteriori assures that the solution does not venture too far from the current optimum and helps to reduce the number of required iterations. Similarly, passing the solution of the previous scan to the next scan reduces the required iterations. By understanding how the optimum evolved with iteration can give insights in the required number of steps. As later shown the majority of the solutions were found in the first 250 iterations, given that the a priori was well constrained. Therefore, the maximum iteration step was conservatively chosen to be 500, requiring two days of computation to find the optimum for all 20 scans.

5
Results

This section reports on the results of the updated retrieval of the Jovian synchrotron radiation. The first section discusses insights gained from the MCMC a posteriori distribution. Then the calibrated synchrotron radiation maps are presented including updated information on the total flux density for the corresponding measurement campaign.

5.1. Uncertainty Analysis

The compound cost function is a useful tool to study the uncertainties and possible variations throughout the Jupiter flyby. As explained in the MCMC, the optimal solution is dependent on the chosen optimization weights, and an analysis purely on the one solution is considered statistically insignificant. When the majority of the solutions, however, converge to a similar region in the solution space, it is a strong indication that the uncertainties represent a significant signal. For that reason, from every scan, the top ten solutions with minimum cost function were chosen to perform the analysis and averaged quantities can be used to study the uncertainties. The following subsections discuss the set of five uncertainties. The performance of the MCMC is dependent on the strength of the synchrotron features. The horizontal polarization has strong emission features next to the planet, allowing the MCMC to converge to a unique solution. The weaker vertical polarization lacks these strong features so that the MCMC had more problems converging to a solution. This is reflected by the size of the error bars in the following section that indicate the 1 σ variation found in the measurements.

5.1.1. Time-offset

Figure 5.1 represents the oscillator drift that was obtained individually for every fit. Recalling that the time-offset has a resolution of 0.1 seconds, the presented quantities are the averaged over the top ten results. The first striking feature is the increase with time, were both polarizations indicate a similar increase over time: 0.3 seconds in the course of 10 hours, consistent with the 0.5 seconds drift in 24 hours as expected from the on-ground post processing by the Cassini Navigation team. The nature of the drift however varies. Where the first ten scans indicate a gradual increase in time offset, the second set of scans indicates an exponential increase. Since during the scan the distance between Cassini and Jupiter is changing, one might suspect that light time variations influence this parameter. The light time variations were corrected for in the computation using the in-build functionality in SPICE, and due to the rather benign flyby distance the light time and relative velocity showed a linear increase and decrease, respectively. It is, therefore, unlikely that the presented quantities are a result of the movement of Cassini.
The second striking feature is that they are not continuous between the scans so that both scans start off from a base value of 0.1 and eventually reach 0.4. The scans were not performed immediately after each other, as the spacecraft had to be rotated first. It is possible that the on-onboard oscillator was corrected between the two scan.
The effect of a positive drift in the oscillator causes the Jupiter model to be offset with respect to its real position. The relatively large beam size convolves the limb crossing residuals with the region of peak synchrotron radiation, and thus it directly affects the synchrotron signal strength. Not properly accounting for the time offset can be easily mistaken for stray thermal emission and result in artificially reduced signal.

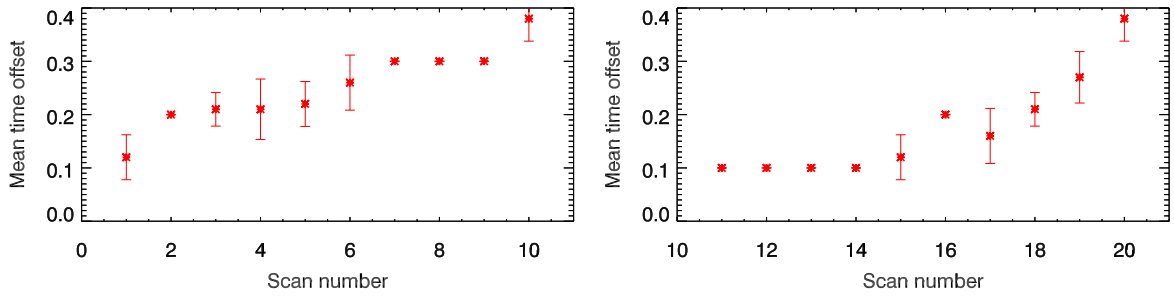

(a) Vertical polarization

(b) Horizontal polarization

Figure 5.1: Oscillator drift

5.1.2. Beam x-offset

The x-offset is defined in the spacecraft coordinate frame and , therefore, is conserved through the rotation of the spacecraft. When inspecting the outcome in Figure 5.2, both sets of scans show to first-degree a constant offset, with a second-degree fluctuation around that mean. This behavior is interpreted as a constant beam offset, due to misalignments in the scan procedure or due to a physical alteration of the antenna, whereas the higher-order variations are the result of spacecraft jitter. Jitter describes the motion of spacecraft below the detection limit of the on-board inertial reference units that establish the pointing of the spacecraft.

Due to the partially polarized nature of synchrotron radiation, the horizontal polarization scan has a stronger signal to noise ratio. This stronger signal allows for resolving smaller variations, which explains why there is finer structure in the second set of scans, compared to the flat behavior of the first set of scans. Nevertheless, the variations are outside of the one sigma variations, indicating that these are indeed statistically significant variations.

Somewhat surprisingly, the mean beam-offset differs between the two set of scans. Since physical changes in the beam offset are very unlikely, this must indicate changes in the pointing knowledge of Cassini. As explained in Chapter 4, these variations are within the pointing knowledge requirements, yet are still larger than expected by the pointing analysis [Pilinski and Lee, 2009]. This could indicate that the inertial reference unit on board have a systematic offset, which is defined by two principal axis . Depending on the relative rotation between the spacecraft frame and the uncertainty frame of reference, the propagated magnitude is different.

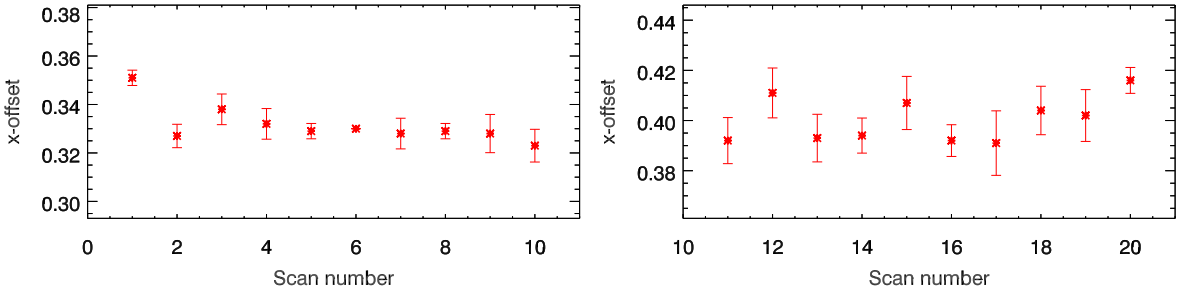

(a) Vertical polarization

(b) Horizontal polarization

Figure 5.2: Beam x-offset

The effect of misalignments in the x direction is very similar to the time offset, as both uncertainties are acting the same plane. As a consequence, depending on the beam motion, these uncertainties can be constructive or destructive. Only a very accurate knowledge of the beam shape allows for disentangling these two factors and prevent the uncertainty from propagating into the synchrotron flux.

5.1.3. Beam y-offset

The y-offset also supports the hypothesis that the beam offset is constant, even though the higher order fluctuations seem to be stronger. Due to weak signal coming from the poles it is harder to constrain the y-offset properly, which could partially explain the large variations. Nevertheless, significant interscan variations in combination with small standard deviations from the MCMC are good indications that these variations are real effects as well. Additionally, the single outlier for scan 1, there are signs that pointing effects have propagated into the analysis, as such a large difference cannot be caused by spacecraft jitter alone. The difference in beam offset between the two sets of scans is also present in the y-offset, confirming that a rotation caused a variation in the pointing knowledge. This difference is baffling and requires further investigation. The existence of the polar residuals has to be scrutinized in light of the temperature model of Jupiter. The eventual 3D distribution was prompted by unexplainable large residuals at the poles. Changing from a flat disk model to a more advanced 3D model, reduced the polar residuals, confirming that they were in parts a retrieval artifact. The whole retrieval was therefore updated using the 3D model in the optimization procedure, however, the polar residuals could not be removed completely. Since the full 3D representation is only limited by its resolution, it is very unlikely that the brightness model is the cause for any signal above the poles.

Disregarding the y-offset causes large residuals at the poles. These residuals at the poles are of special interest, as they probe a little-probed region of Jupiter atmosphere. The initial retrieval used an excessive disk temperature to counter these residuals, which also deflates the synchrotron signal.

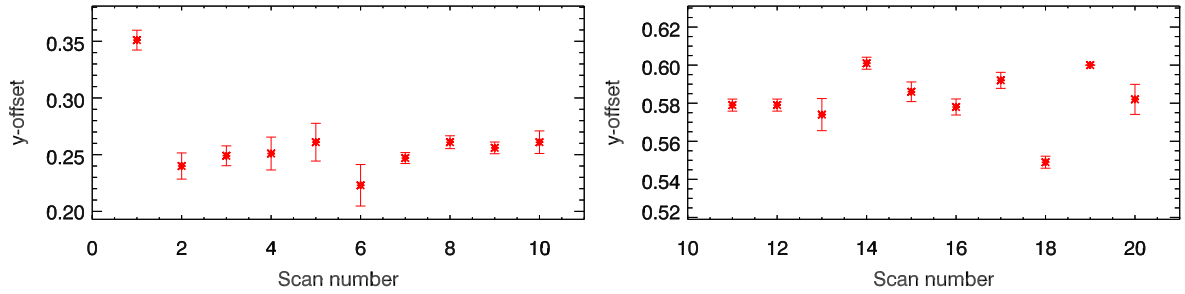

(a) Vertical polarization

(b) Horizontal polarization

Figure 5.3: Beam y-offset

5.1.4. Brightness Temperature

The brightness temperature of Jupiter refers to the peak brightness temperature at nadir of the underlying limb darkened model. This temperature does not affect the zonal deviations, which are added after obtaining the best-fit brightness temperature. The zonal structure was obtained from observation at similar frequencies so that it is reasonable to assume that they are applicable to this research. Henceforth, the two signals are decoupled, and only the underlying brightness temperature is evaluated.

Both polarizations show a relatively stable brightness temperature, as expecting from the small longitudinal variations as reported by the high-resolution radio maps at 15 GHz [Cosentino et al., 2017, de Pater et al., 2016]. The stable temperature is also indicative of a very robust solution allowing for constraining the brightness temperature with great accuracy. The vertical polarization (Scan 1-10) does not show a consistent longitudinal trend, however, as indicated by the large error bars, the MCMC had problems converging to a single solution, a result of the weak emission features. Contrary, the horizontal polarization (Scan 11-20), shows two small dips around Scan 14 and Scan 18. These scans correspond to small magnetic latitudes, that is Cassini is looking directly at the magnetic equator, where the synchrotron signal is the strongest. Since the MCMC is trying to minimize the signal in front of the disk, an increase in synchrotron signal causes a reduction in the brightness temperature. This has to be carefully considered, as it discounts the synchrotron signal in front of the disk as an increase in brightness temperature. Avoiding this effect would require introducing further a-priori knowledge into the MCMC. Considering that the signal in front of the disk is small compared to the main emission region (10%), this effect is accepted as a by-product of the retrieval. In worst case scenario, it deflates the synchrotron flux slightly. As this can be reduced to a change in brightness temperature, this effect is further analyzed when analyzing the sensitivity of the solution to the brightness temperature in Section 5.6.

No full explanation has been found yet for the difference in mean peak brightness temperature of 1K. This could indicate a gain dependent on the rotation of the beam, other observations, however, have not reported on such an issue. Since the radiation in front of the disk is mostly horizontally polarized, another explanation could be an increased activity in front of the disk.

Misrepresenting the brightness distribution has shown the greatest impact on the retrieved radio maps. When the main beam is centered on the main synchrotron radiation, the thermal emission from leaking in from the side lobes still dwarfs the synchrotron signal. During the subtraction of the simulated antenna temperature from the calibrated antenna temperature, a too bright Jupiter effectively decreases the signal attributed to the synchrotron radiation.

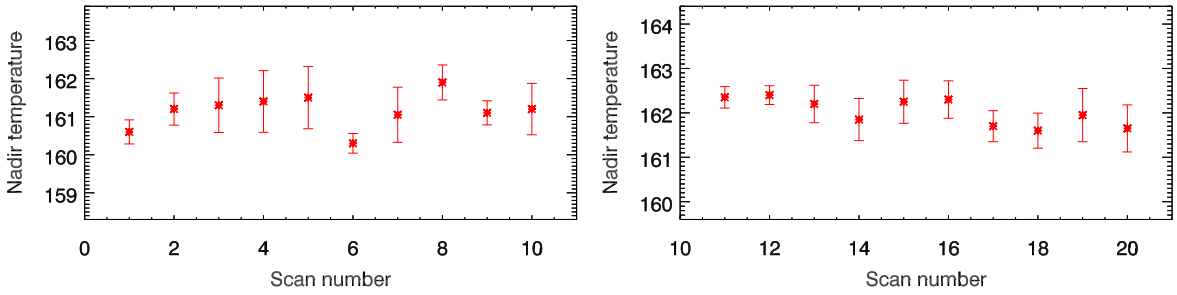

(a) Vertical polarization

(b) Horizontal polarization

Figure 5.4: Nadir brightness temperature

5.1.5. Limb Darkening Coefficient

The limb darkening coefficient was introduced to study the polar residuals. These residual were originally attributed to an insufficient brightness distribution that could not resolve the fine structure of the brightness model. However, even a complete 3D dimensional brightness distribution could not explain the curious signal, leading to the introduction of a more basic brightness model was introduced to study the residuals. Considering that the east-west limb darkening coefficient is normally given by p = 0.08, [de Pater et al., 2016], it is astounding that both polarizations converge on a weaker limb darkening coefficient (see Figure 5.5). Barring a strong, yet unphysical synchrotron signal from the poles, this indicates that the polar regions must be depleted in ammonia. A similar conclusion had been reached by de Pater [1986], where she inferred the ammonia abundance from high frequencies maps of Jupiter.

It is difficult to determine any longitudinal trend. The limb darkening coefficient for the horizontal polarization seems to be anti-correlated with the magnetic latitude, similar to the conclusion reached by the brightness temperature profiles. However, the large uncertainties do not allow for any significant conclusions.

Lastly, by not accounting for the signal appropriately large polar residuals can be confused for an excessive radiation from the polar region. By increasing the brightness temperature of Jupiter, the polar residuals can be suppressed, at the cost of overestimating the flux from the remainder of the disk. Since the measurement compromises the total flux, an increased thermal contribution leads to a reduction in the synchrotron contribution.

5.2. Summary of Results

The scan averaged results can be found in Table 5.1. The uncertainty analysis also allows for constraining the disk averaged brightness temperature, by combining the best fit results obtained for both scans. The uncertainty is constrained by the 1% measurement uncertainty, plus taken into account the variations from the optimization routine. The final obtained disk averaged brightness temperature of 158.6 $\pm$ 2.4$[K]$ and is about 2 K above the VLA calibration (156.6 $\pm$ 4.7$[K]$), yet still within the uncertainty [de Pater et al., 2016].

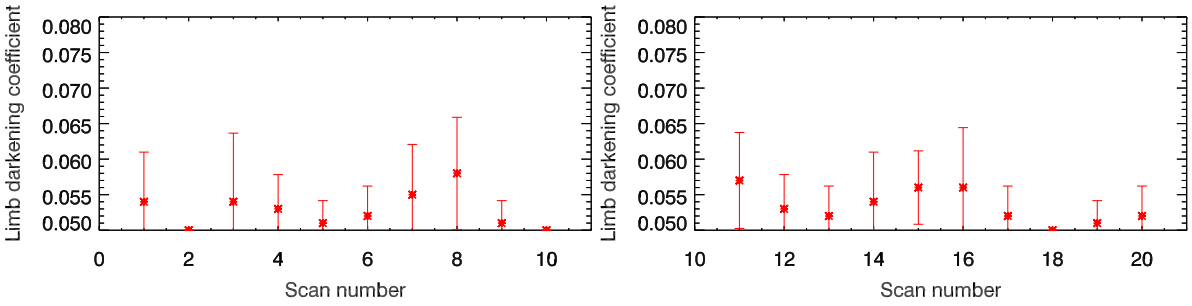

(a) Vertical polarization

(b) Horizontal polarization

Figure 5.5: North - South limb darkening coefficient

Table 5.1: Scan averaged uncertainty analysis for the two subset of scans.

Uncertainty	Magnitude	
Polarization	Vertical	Horizontal
dt [s]	0.26	0.17
dx [mrad]	0.33	0.40
dy [mrad]	0.25	0.58
T [K]	161.32	161.75
p [-]	0.05	0.05
Scan averaged		
T [K]	161.53	
p [K]	0.05	

5.3. Synchrotron Maps

This section presents the results for obtained by choosing the combination of uncertainties that was obtained from the MCMC for each map individually. For a detailed analysis of how the synchrotron radiation results change with the best-fit optimization, the reader is referred to Section 5.6.
The retrieved data are time sorted residual antenna temperature, corrected for the thermal contribution. For each measurement, the information on the pointing of the RADAR boresight during the can be used to map the information onto the plane of the sky. The distance between the boresight and Jupiter's center is obtained using the SPICE software, and the corresponding residuals are then interpolated onto an even grid that extends 8 R_J in the equatorial region, and 6 R_J in the polar direction centered on the planet. This results in a total of 20 maps, 10 for each polarization, which can be found in Appendix C. This section focus on the results that can be obtained from the rotationally averaged maps, which have a higher signal to noise ratio.

Vertical polarization Panel a) of Figure 5.6 displays the interpolated map for the vertical polarization. The antenna was aligned with the momentum vector of Jupiter's orbital plane and thus is sensitive to vertically polarized emission, or the fraction of the radiation projected onto the antenna. The local magnetic field controls the electron's motion, and thus the polarization of the synchrotron radiation reflects the local magnetic field. Whereas at the magnetic equator, the field lines of a perfect dipole are perpendicular to the equator, at higher latitudes the field lines are curved towards the planet. The resulting polarization is therefore to the first order defined by local magnetic field direction and has a component that is picked up by both alignments of the antenna. The vertical polarization, therefore, measures the projection of these particles onto the antenna plane. As can be seen, the main emissions indeed originate from the high latitude emission rings, where clear synchrotron peaks are recorded, whereas there is little radiation coming from the equatorial region. At the equator, only particles with small pitch angles emit partially polarized emission, which is picked up by the antenna. The measurement is therefore in agreement with the expectation that the majority of the electrons

Table 5.2: Emission maxima characteristics

	T_B (K)	Distance (R_J)	Latitude (°)
Region	**High latitude emission**		
left upper	2.45	1.44	24
left lower	2.14	1.45	33
right upper	2.30	1.44	34
right lower	2.41	1.37	27
	Equatorial		
left	3.32	1.47	0
right	3.64	1.46	0

is confined to the magnetic equator.
The second observation is the lack of signal coming from the face of the disk, indicating that the chosen brightness model accurately subtracts the thermal emission from Jupiter. The small negative residual at the center of the disk are indication of an excessive brightness temperature, however, when closer analyzing the negative residuals as given in Figure 5.7 a), the majority of the negative residuals are concentrated above -0.05 K, confirming the excellent brightness model. Furthermore, the negative residuals never drop below -0.15 K, which is consistent with the magnitude of thermal fluctuation in the system of about 0.13 K. The synchrotron region covered by the raster scans varied as the satellite's slowly receded from the planet. All measurements were interpolated onto a regular grid with size of 8 R_J x 6 R_J, slightly exceeding the measurement region. For data points outside of the measurement region, the interpolation was configured to return a 0 K signal, resulting in the large histogram count centered around the 0K mark. Also, note that the histogram counts left and right of the 0K mark should be of similar magnitude, as they reflect the noise level of the system, that is normally distributed for Gaussian noise. This yet another sign of the excellent brightness temperature fit of the Jovian disk.
Lastly, the polar regions show no indication of a residual signal. As a result of the magnetic field lines at the poles, which have a very small angle with the spin axis, any electrons in the vicinity of the poles would have an orbit that is quasi-parallel to the magnetic equator and would only be seen in the horizontal polarization measurements. As a consequence, any polar residuals can be mainly attributed to the ammonia abundance at the poles. The lack of polar residuals supports the hypothesis that the ammonia abundance is depleted at the poles and makes a stronger case for the chosen limb darkening coefficient.

Horizontal polarization The complementary horizontal polarization is provided in panel b) of Figure 5.6. The polarization axis was aligned with Jupiter's equatorial plane and thus picked up radiation from electrons with large pitch angles orbiting close to the equator. Since this comprises the majority of the particles (about 70% [de Pater, 1981a, Van Allen, 1976]), the received signal, especially from the equatorial region, is stronger than compared to the vertical polarization. The strong radiation maxima occur at 1.47 R_J (left) and 1.46 R_J (right) and agree with the expected location of the extremes [de Pater and Klein, 1989].
The radiation region has a component at the mid-latitudes and can be seen to extend further outwards in the equatorial plane. As explained before the polarization intensity is tied to the gyration motion of the electron. As explained in the Chapter 4, the efficiency of receiving out of plane radiation for linearly polarized antennas is given by a factor of $(cos\theta)^2$, where θ is the angle between the antenna and the wave's polarization plane. Close to the planet, the field lines are strongly curved, resulting in an electron motion that has a large angle with the equator, and the radiation is picked up by an antenna aligned with the equator or the pole. At greater distances from the planet, the curvature of the magnetic field lines decreases, so that the electrons gyrate at a smaller angle with the equator and the antenna aligned with equator picks up the majority of the signal.
A closer look at the equatorial region in front of Jupiter's disk reveals small positive residuals. The equatorial region is characterized by a positive brightness anomaly due to the ammonia depletion in the Northern and Southern Equatorial Belt. In between the spacecraft and the planet, is the main synchrotron emission ring. Recalling that the total synchrotron signal is the integrated emission from all electrons along the line of sight, the emission in front of the disk only has short integration path length and thus is weaker compared to next

to the planet. The impact of the Zone-Belt structure is mitigated using high-resolution scans from the VLA in 2000 (see Appendix A) and 2016[de Pater et al., 2016]. Nevertheless, this region is considered the least constrained.
The signal coming from the poles represents an interesting feature. There are several instrumental effects could be the source of this feature: (i) an insufficient representation of brightness at the poles; (ii) uncertainty in the beam structure; and (iii) drift in the beam offset. Each of these three points can be ruled when considering them carefully.
The MCMC was setup up to determine the best-fit parameters for the brightness model of Jupiter. The MCMC converged for both polarization to remarkably similar parameters for the thermal brightness model: all scans converged to the depleted ammonia solution, the only difference was the nadir brightness temperature, which was tuned to reduce the residuals in front of the disk and should have a minor impact on the polar residual. Furthermore, the vertical polarization showed no indication of the polar residuals, excluding a possible ammonia misrepresentation. Similarly, an insufficient description of the brightness model could introduce artifacts. This problem was identified early in the retrieval, and therefore a full 3D description of the brightness model was introduced at the cost of more computing power. The resolution of the brightness model is of lesser importance, as the beam averages over large portions of the brightness model and reduce the need for a high-resolution brightness model. These two factors exclude the brightness as a possible source for the polar residuals.
Whereas the main beam structure is well defined, especially the near-side lobes are more difficult to resolve. The sun scans prior to Saturn Orbit Insertion have improved on the knowledge in the near side lobes. Nevertheless, it is conceivable that small uncertainties in the beam structure can cause residuals in the retrieval. As a consequence of the invariant nature of the main beam uncertainties, uncertainties should materialize across all scans and should be present at the same location for all scans. Since the residuals are present only at certain longitudes, and absence at others it is unlikely that this is caused by a deficiency in the beam structure.
Lastly, a drift in the beam-offset as identified in the uncertainty analysis could introduce similar artifacts, especially a drift in the y-offset. The y-offset controls where the Jovian brightness model is placed in the Cassini RADAR reference system so that shifting the brightness model in the positive y-direction (upwards), introduces an asymmetric residuals pair. The brightness model underestimates the thermal contribution at the south pole, causing positive residuals, and overestimates the brightness at the north pole, resulting in a negative residual. Closer analyzing the residuals reveals that in many instances the residuals can be found in the same scan at both the north and south pole, and do not show the asymmetric structure. Therefore, the notion of positive residuals on both poles is hard to combine with a y-offset. It could potentially be explained by a beam drift on timescales lower than can be resolved by MCMC. Large difference between individual scans would support the hypothesis that the beam offset is drifting, however, the small variations as shown in Figure 5.3b do not support this assumption.
This strongly hints at the synchrotron nature of the polar residuals. The presence of synchrotron radiation is normally puzzling, as these magnetic field lines entering at the poles corresponds to large L-shells, indicating that the electrons must originate from the middle or outer magnetosphere. Furthermore, the Cassini measurements are sensitive only to high energy electrons , requiring strong acceleration mechanisms in the outer magnetosphere. These structures have been seen before [de Pater, 1980a] in VLA maps, however, were often reduced to artifacts. Interestingly, the recent Juno mission has on-board capabilities of detecting high energy particles in-situ [Becker et al., 2016b]. Particles of sufficient energy (> 10 MeV) penetrate the shielding of the spacecraft and create a noise signature in the star-tracker sensors. The in-situ population can be retrieved by understanding how primary and secondary particles affect the sensor. During the first Perijove pass the spacecraft picked up signal while it was threading through the high latitude region, and also experienced an increase in the sensor noise when passing over the poles [Becker et al., 2016a]. This local increase above the pole is consistent with the observations by Cassini, however, further observations of Juno are required to confirm the origin of this signal.

Combined polarization The brightness temperatures maps in panel a) and b) of Figure 5.6 are presented in equivalent brightness temperature for a single linear polarization. As explained in Chapter 4, the total brightness map are then obtained by adding the measurements at two orthogonal polarizations [Piepmeier et al., 2008]. Therefore, panel c) is simply the sum of two polarization. Note that this addition is based on the assumption that the emission region did not vary over the course of the 20 hours. Variations on such short time scales are not expected [de Pater and Klein, 1989], however, should be kept in mind. Furthermore, it

is important to highlight, that these maps constitute the brightness maps convolved with the Cassini beam. Deconvolution of the brightness map is in theory possible, however, due to the weak synchrotron signal, the deconvolution was dominated by numerical issues, and introduced large outliers. The convolution conserves the emitted power, however, degrades the details of the synchrotron maps. This leads to a spatial broadening of the emission features while reducing the intensity at the extremes.
As a consequence, the resolution of the measurements does not allow to distinguish between the equatorial emission and the high latitude rings, but the north-south elongation around 1.5 R_J is an indication for secondary emission at higher latitudes. Similarly, the radiation originating in front of the disk is most likely a result of the convolution process.

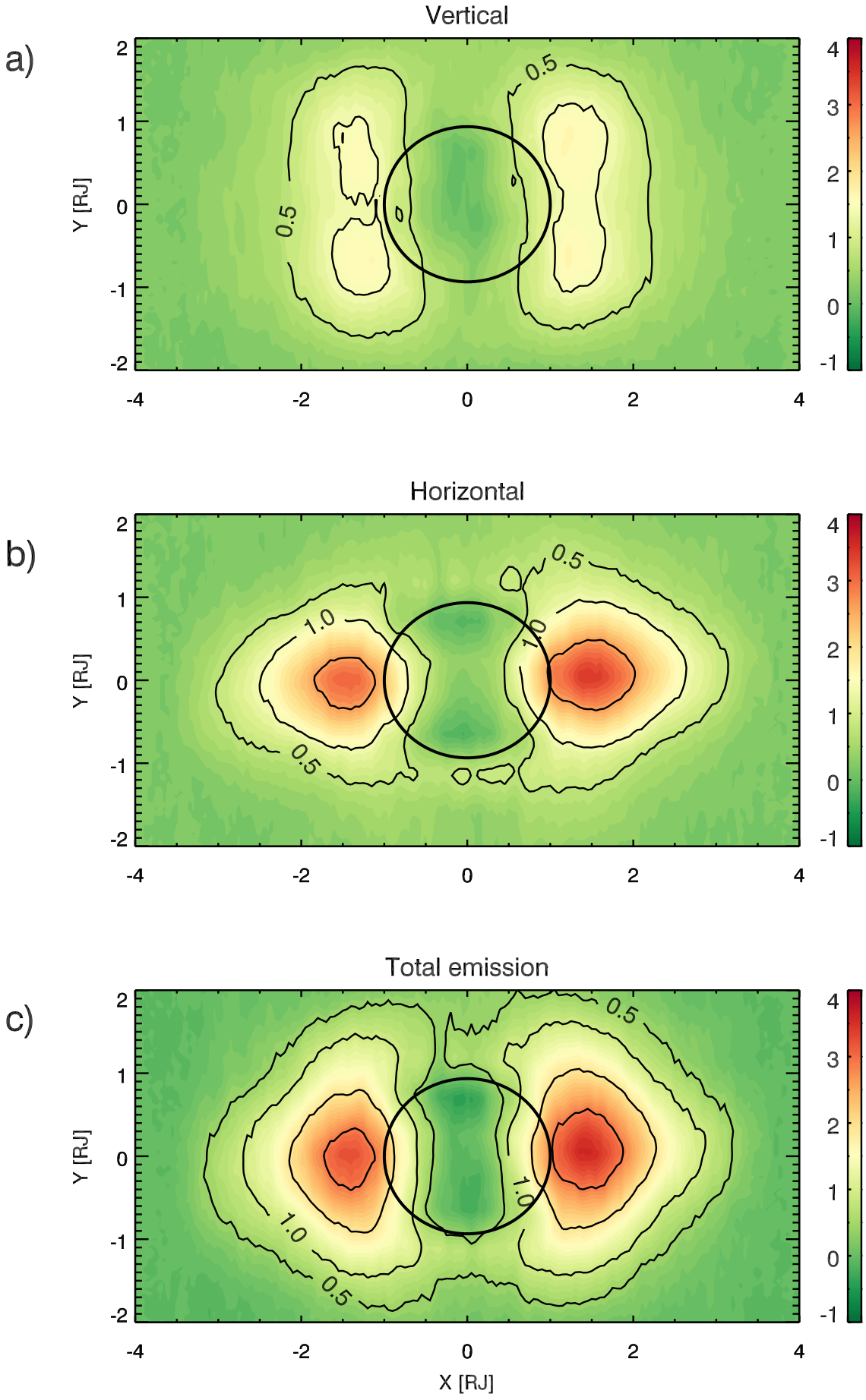

Figure 5.6: Synchrotron radiation maps for the two polarization and superimposed for the total radiation.

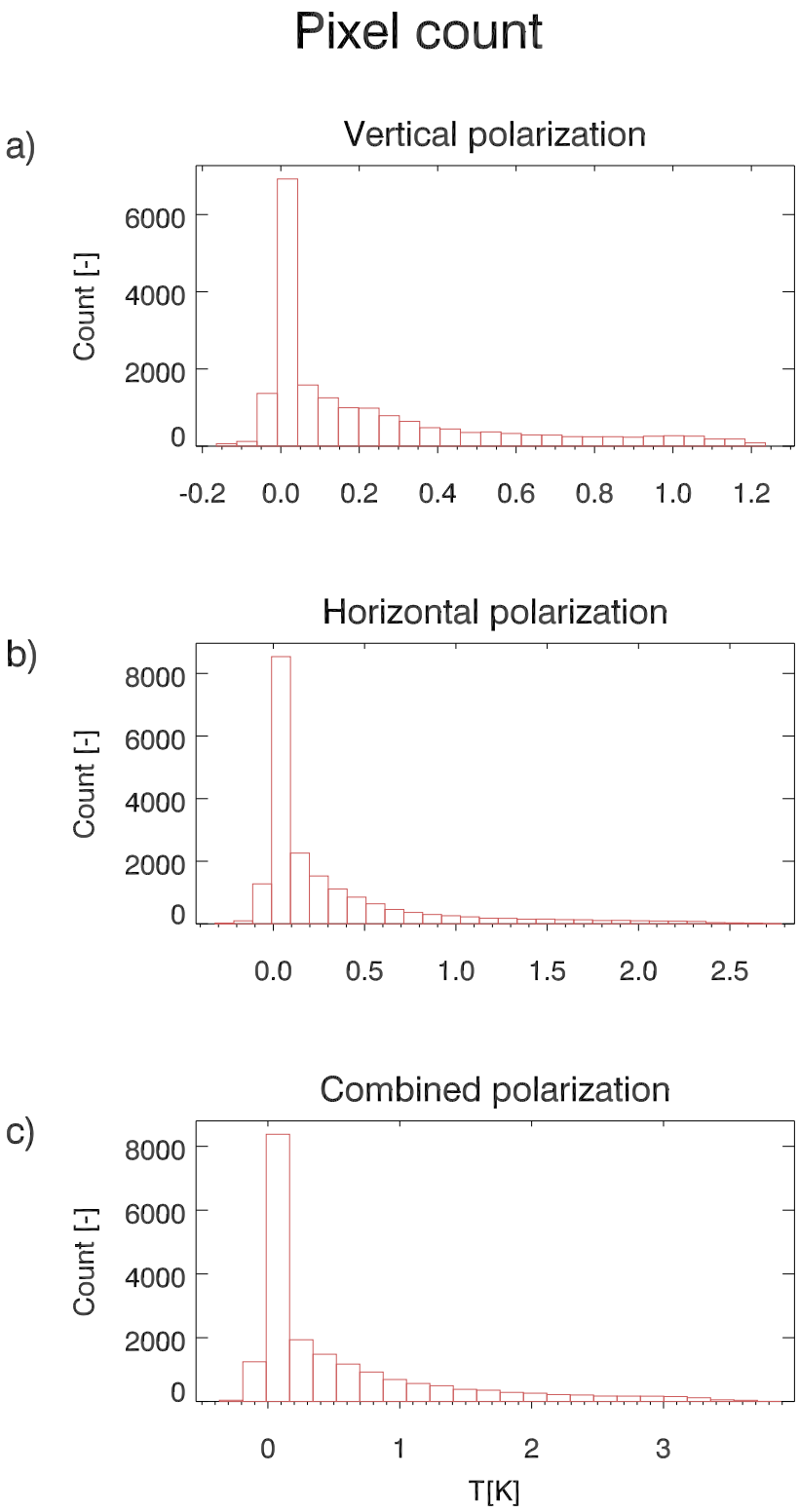

Figure 5.7: Negative residual analysis

5.4. Beaming Curve

The total power emitted by the electrons is captured by the flux density normalized to a distance of 4.04 AU [Klein et al., 1989]. The integrated flux density is obtained by integrating the emission over the source region as detailed in Chapter 4. This integration is performed separately for the two polarizations given in panel a) and b) of Figure 5.8 and for the combination of both polarizations in panel c), where the integrated flux density is shown as a function of the central meridian longitudes. This metric is referred to as the beaming curve in the literature. At this point, the reader is reminded that the beaming curve is a result of the beamed synchrotron radiation and the dipole tilt of the magnetic field, where the maximum of the beaming curve corresponds to the longitudes, where the magnetic equator is viewed straight on.

Vertical polarization The vertical polarization beaming curve is relatively flat lacking the well-pronounced maxima as expected from an ideal beaming curve. This is most likely not an actual physical artifact, rather a consequence of the weak signal received for the vertical polarization. The one outlier at CML of 285° is probably a real signal, as the corresponding synchrotron map shows no sign of uncertainties being the cause for this anomaly.

Horizontal polarization The orthogonal polarization shows the familiar shape of the beaming curve, with two defined maxima centered around ≈ 100 ° and ≈ 280 °. These longitudes correspond to the viewing geometry where the equator is seen edge on.

Combined polarization The two polarization were added and interpolated at a 10 deg cadence, and the results can be found in panel c) of Figure 5.8. The exact shape of the beaming curve is dependent on the declination of the observer [Klein et al., 1989]. For a systematic analysis, Klein et al. [1989] proposed to describe the beaming curve by the best-fit Fourier coefficients of the form:

$$S(\lambda) = A_0 \left[1 + \sum_{i}^{3} A_i \; sin(i(\lambda + \phi_i)) \right] \tag{5.1}$$

where,

$\boldsymbol{\lambda}$ $[rad]$ The Central Meridian Longitude of the observer
$\boldsymbol{A_i}$ $[-]$ Amplitude of the sinusoidal variations of order i
$\boldsymbol{\phi_i}$ $[rad]$

These seven parameters were obtained by fitting the beaming curve to Equation (5.1) using a weighted least square fit and the results are given in Table 5.3. The weights were obtained from the sensitivity analysis as presented in Section 5.6. The table also compares the obtained coefficients to Klein et al. [1989] systematic analysis of the coefficients as a function of the observer's declination using multi-year observation at 13-cm. With a changing declination of the observer, the angle with magnetic equator varies, resulting in different beaming curve characteristics. Especially the intensity and the location of the maxima are sensitive to the declination. Variations of the coefficients with frequency are not well understood [de Pater et al., 2003], however, the comparison reveals that the beaming curve coefficients are remarkably stable across a wide frequency range. The deviations of the higher order coefficients is more likely related to the poor signal, rather than an actual deviation. Furthermore, also the spread in the coefficients presented in the original research increases for the higher orders, and agree with other beaming curve analysis comparisons [Santos-Costa et al., 2011].

Table 5.3: Beaming curve obtained from the Cassini measurements, and compared to declination-dependent coefficients derived from a multi-year analysis [Klein et al., 1989].

Coefficients	A_0 (Jy)	A_1 (Jy)	ϕ_1 (°)	A_2 (Jy)	ϕ_2 (°)	A_3 (Jy)	ϕ_3 (°)
Cassini Radar	1.10	0.031	226.2	0.047	-65.0	0.02	33.9
Multi year analysis	-	0.032	227.3	0.052	-71.3	0.01	-5

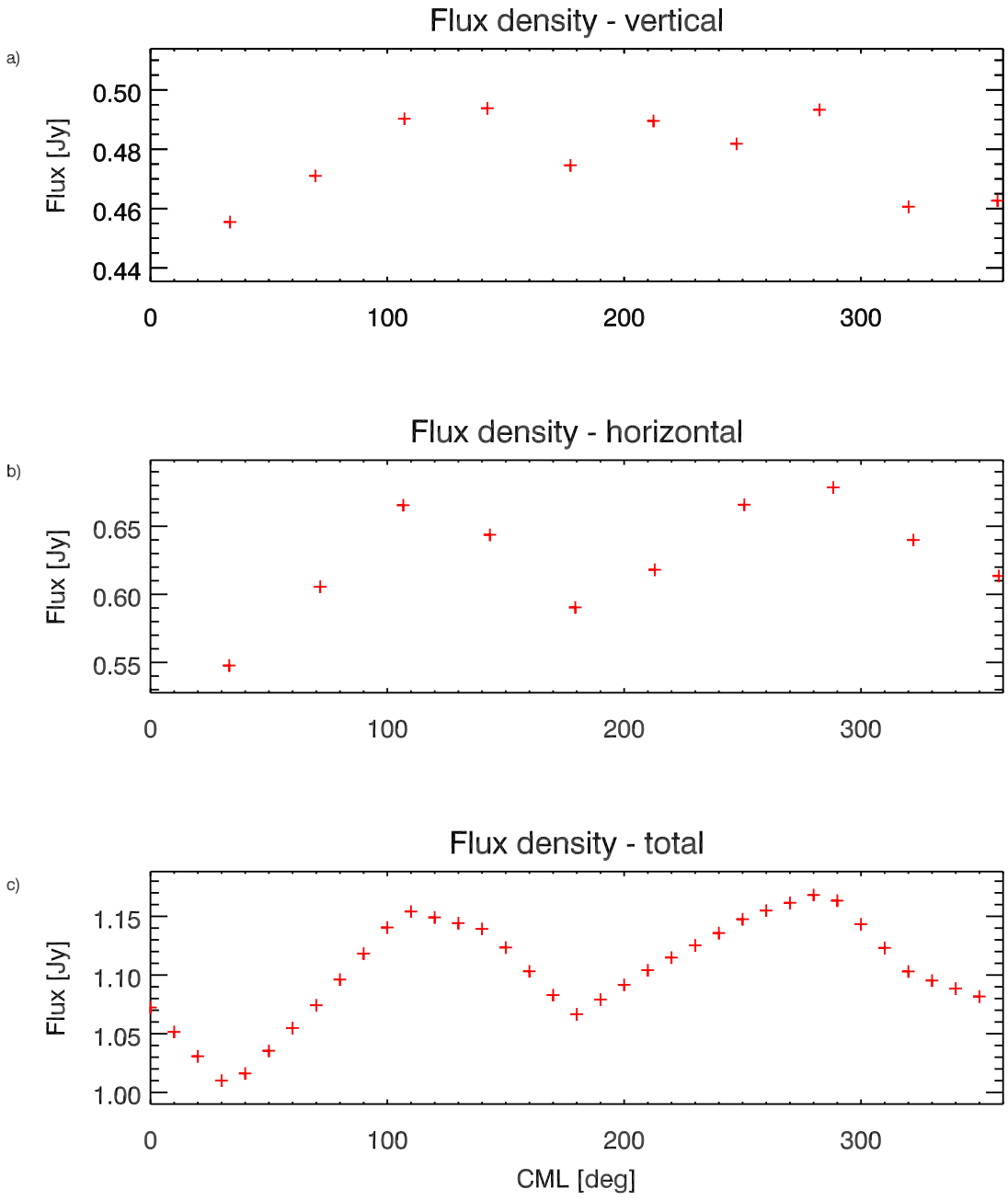

Figure 5.8: Beaming curve of the synchrotron radiation for the vertical polarization (panel a), for the horizontal polarization (panel b) and combined polarization.

5.5. Tomographic Reconstruction

The rotationally averaged maps allow for understanding the spatial distribution of the electrons, whereas the tomographic reconstruction allows to understand how the electrons are distributed in the equatorial plane. There are three methods available for producing tomographic reconstruction technique: (i) deriving the 3-D distribution directly from the visibility data of the interferometer [Sault et al., 1997]; (ii) back projection technique [de Pater and Sault, 1998]; and a cartographic reconstruction technique [Santos-Costa et al., 2011]. The first method is not possible as the data were obtained from a single dish measurement; however, the other two are applicable.

Both techniques are based on combining the vertical and horizontal polarization maps. The measurement campaign first mapped a full rotation in vertical polarization before rotating the spacecraft by 90 deg and

obtaining the orthogonal polarization. As a consequence, the polarizations are separated by 10 hours and combining the maps is based on the assumption that the synchrotron structure is invariant during the full mapping campaign. There is no information on the variability on such short time scale so that it is hard to assess the applicability of this assumption. With a scan duration of 60 minutes, each map corresponds to a certain CML range. The mapping was organized such that the same CML range was obtained at each polarization, allowing to merge the maps.

5.5.1. Back Projection Technique

The back projection technique is based on equatorial cuts through the maps. For each CML range, a cut along the magnetic equator was obtained, as shown in Figure 5.9 for three selected CMLs. These scans represent ten slices through the equatorial plane separated by 30 °. By interpolating between the various slices, the brightness temperature can be projected into the equatorial plane as after correcting the CML. The emission from the planet originates from the sides of the planet and thus is offset by ± 90° from the spacecraft's longitude. Therefore, the projection is rotated by 90 ° to agree with the measurement geometry. When looking at the figure, the brightness temperature corresponds to the longitude where it occurs. The equatorial emission is given in Figure 5.10, the northern and southern are given in Figures 5.11a and 5.11b.

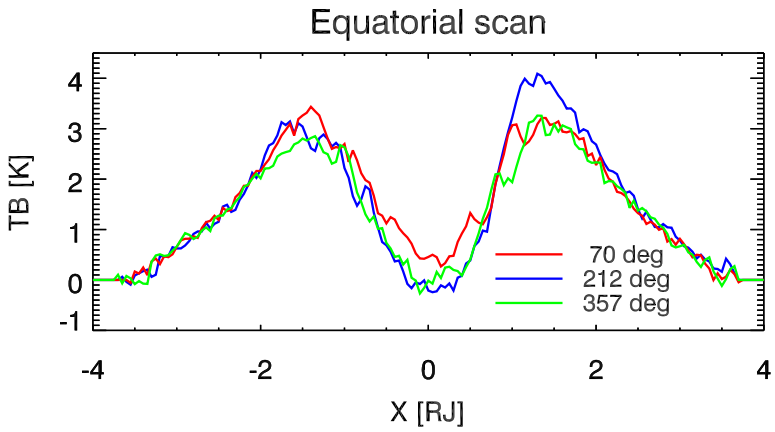

Figure 5.9: Cut through along the magnetic equator for the indiciated central meridian longitude. The variations in intensity are caused by higher order moments in the magnetic field.

Equatorial ring As expected the maximum in the radial direction can be found just inwards of 1.5 R_J, confirming that the value found for the rotationally averaged maps (see Table 5.2 is consistent across all CMLs. The location of the peak as a function of the CML is given in Figure 5.12, where small variations of the peak location are evident. The CML corresponds to the location of the peak and is shifted by 90 ° from the CML of the observer so that if the spacecraft is at CML of 180 °, the left peak corresponds to 270 ° and the right peak to 90 °. Nevertheless, the peak location for the individual maps is prone to noise in the retrieval, and large deviations from the average position are most likely a combination of physical effects and noise in the system. Furthermore, the large beam size of Cassini degrades the accuracy of the peak location.
A closer look at the peak location can still reveal some information. The intensity is controlled among others by the local magnetic field strength, which is variable close to the planet due to the higher order moments. Note, that the peak location refers to the same longitude, and an agreement of both curves is a good indication that the magnetic field strength is the controlling factor in the peak location. The agreement between the curves also validates the retrieval and confirms that the uncertainties are constrained properly.
The rocking motion of the magnetic field controls the intensity as discussed for the beaming curve, and the regions with lower intensity in the equatorial plane correspond to viewing geometries with large angles to the equator. The variation with CML can also be seen further outside, where especially the region around 330° appears compressed, however, the decreasing signal hinders a more detailed analysis.
The last point of interest in the equatorial regions is the East-West asymmetry, which existence was explained by the higher order moments in the magnetic field [de Pater et al., 1997]. The ratio of the intensity of the left peak and right peak are compared in Figure 5.13. The curve as obtained by the VLA [de Pater et al., 1997] is characterized by three maxima, one major maximum at 216° and two minor maxima at which at 115° and

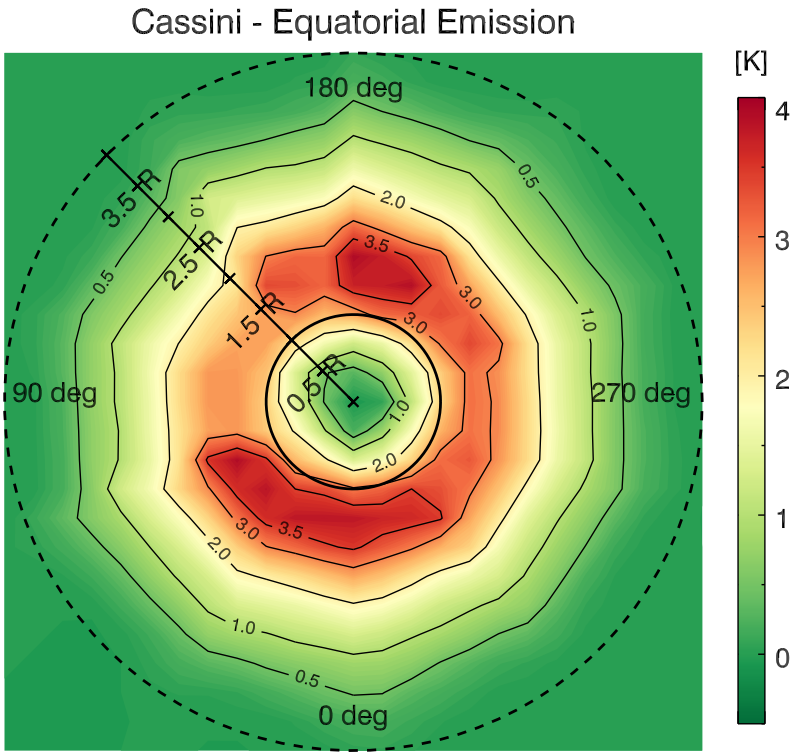

Figure 5.10: Backprojection technique for the equatorial plane. The units are given in brightness temperature.

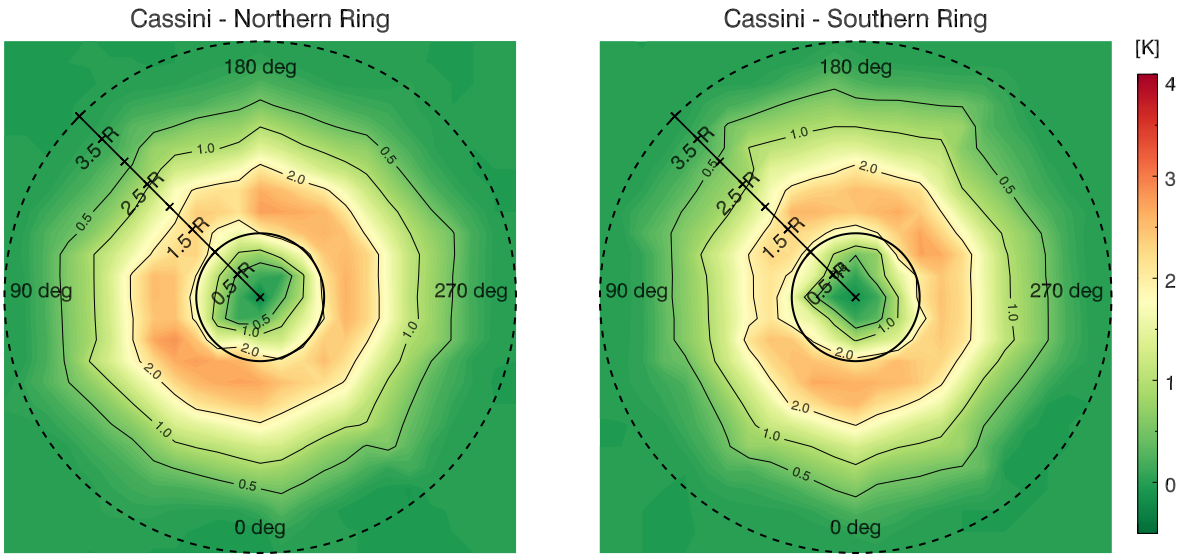

(a) Northern emission ring at 30° latitude

(b) Southern emission ring at -30° latitude

Figure 5.11: Backprojection technique for the high latitude emission ring. The units are given in brightness temperature.

322°. The curves agree regarding the locations of the enhancement but differ clearly in magnitude. The convolution of the Cassini beam brings the ratio of the two peaks closer to unity, as it widens the emission region, and thus reduce the sharpness of the peaks. The agreement of the maxima location can also be seen as validation of the retrieval, as the maps do not differ substantially from previous measurements.

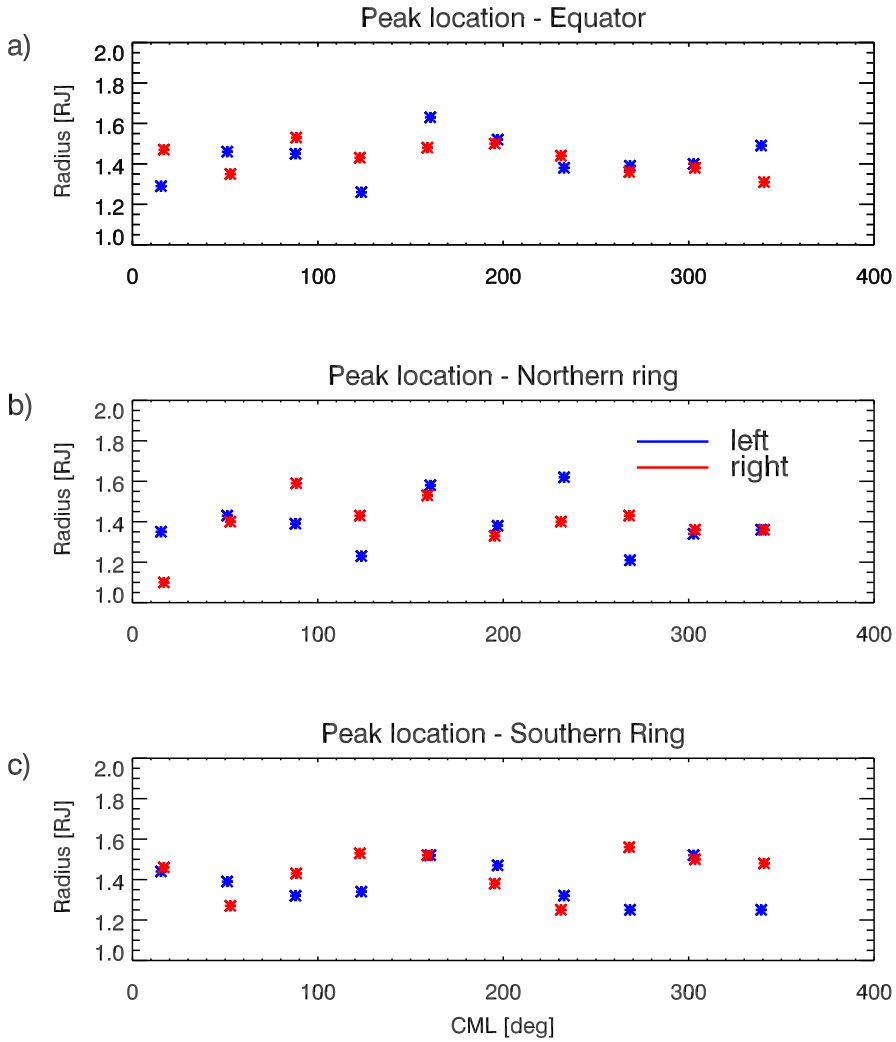

Figure 5.12: Location of the synchrotron peak as a function of longitude. The location of the peak is assumed to be in the orthogonal plane and thus is shifted by 90° from the observer's longitude. The position for the equatorial emission is given in panel a), for the northern ring and the southern ring can be found in panel b) and c).

The high latitude rings The high latitude rings are more homogenous as seen in Figures 5.11a and 5.11b for the northern and the southern ring. Both emission rings are more radially compressed and weaker compared to the equatorial emission as expected. In terms of deviations, especially the northern ring appears radially very symmetric, indicating the rocking motion of the magnetic field has less impact on the northern ring. There are signs of a small decrease in emission around 300°, which would be shifted by 30° from the equatorial location. When looking at the southern ring, the minimum around 1.5 R_J can be found at 10°, a 40° rotation compared to the equator.
The peak location as found in Figure 5.12, panel b and c, shows more variability, which is more a sign of the poor signal than an actual physical effect.

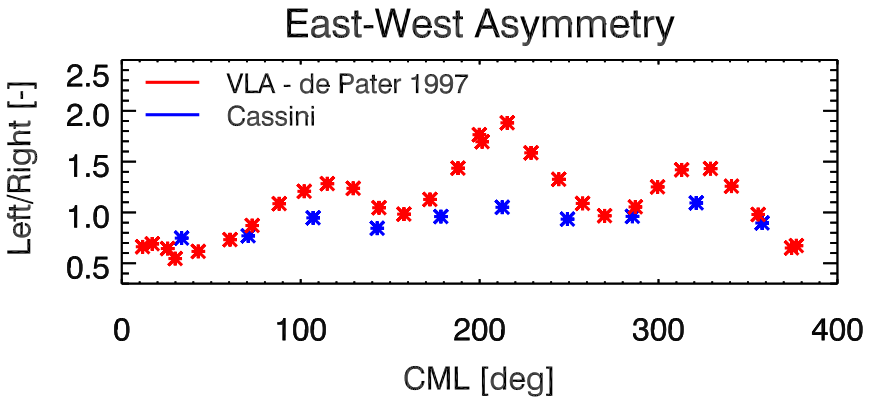

Figure 5.13: East West assymetry as a function of longitude. The variations are assumed to be a consequence of higher order moments in the magnetic field.

5.5.2. Cartographic Reconstruction Technique

This technique is desribed in detail by [Santos-Costa et al., 2011, Appendix A]. Inverting the measurements directly offers the advantage of mapping the electron distribution, and requires fewer assumptions than the back projection technique.
This technique represents the equatorial plane as point sources, where each point represents a volume filled with radiating electrons. As the equatorial region is scanned, the received signal is the line-of-sight integral of all point sources. As the planet is rotating, the line of sight is composed of a different combination of point sources. This system represents a set of linear equations, of form AX = B, where A is a matrix indicating which point sources are contributing, X is the strength of each volume and B is the integrated line-of-sight intensity. The equatorial scans populate the A matrix, and with sufficient coverage, the linear system can be solved by minimizing the residuals to obtain the magnitude of the point sources in units of volume emissivity. The volume emissivity is a proxy for the electron density in the region and therefore a very useful quantity. The results of the Cassini scans can be found in Figure 5.14.
On first impression the cartographic reconstruction is very similar to the back projection technique, validating the assumptions that the emission can be folded over by projecting it at a 90°. Nevertheless, the detail on the cartographic reconstruction is greater and allows to study the electron population more in detail.
As expected, the majority of the emitting electrons are concentrated around 1.5 R_J, with two distinct high-emission regions at 30° and 200°. Notably is that the electrons appear more spread out than in the back projection technique, especially the region around 300°, indicating that the emission region is more homogenous than expected. We will revisit this point when comparing the emission to other observations in Section 5.8.

5.6. Sensitivity

The analysis presented above is based on best-fit solution for each single scan, making the analysis sensitive to the chosen combination of uncertainties. By studying the impact of the uncertainties on the retrieved quantities, their importance can be evaluated.
For the sake of brevity and sanity, only the impact of the beaming curve is be analyzed in detail. Considering that the beam offset and oscillator drifts mostly impacts the signal close to the planet, the overall structure of the synchrotron is not very sensitive to these two parameters, whereas changes in the thermal model surpress or enhance the radiation region, and are, therefore, best captured through the beaming curve. The detailed analysis focuses on the impact of the each uncertainty on the beaming curve, by keeping all uncertainties constant (Ceteris paribus) and varying only the uncertainties of interest through the full range in the solution space. As an example, when evaluating the impact of the time-offset, the best solution for the remaining four uncertainties is used, and the integrated flux density is obtained for each possible value of time drift ranging from 0 to 0.5. The range of integrated flux density is indicated by the error bars on the beaming curve, where the lower end corresponds to the minimum value obtained and the upper end to the highest value obtained. It is, therefore, intentional that the error bars are not symmetric.

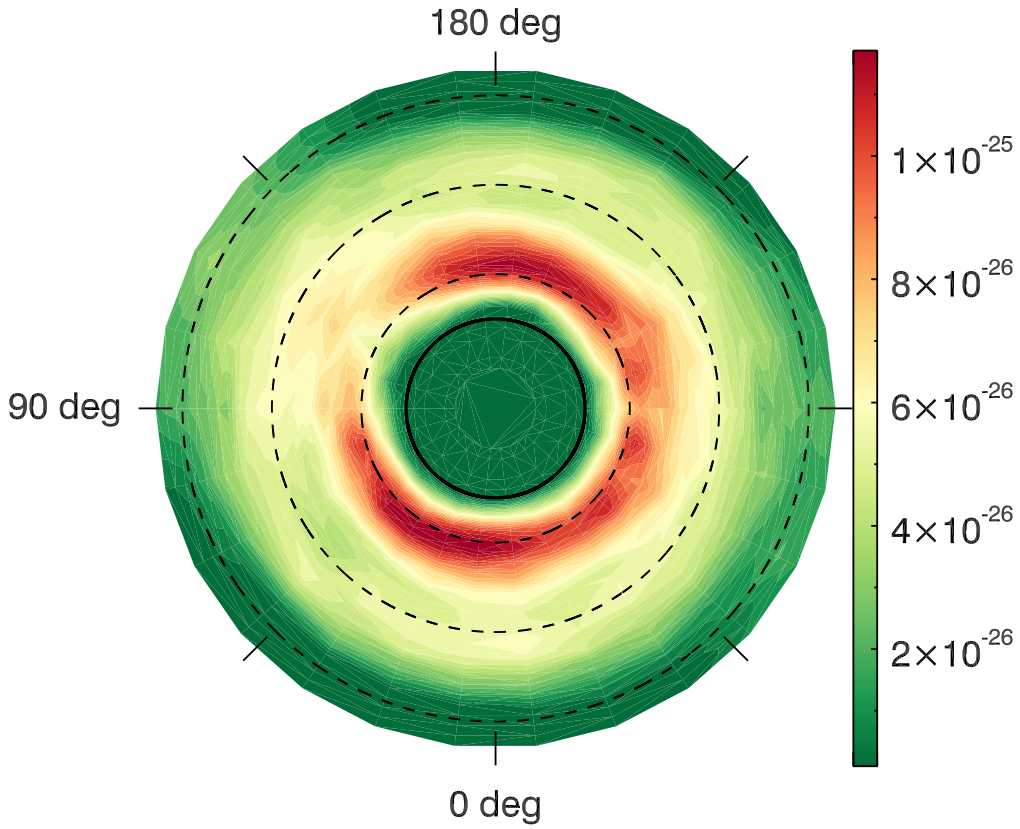

Figure 5.14: Cartographic reconstruction of the electron population in the equator in units of Volume Emissivity $[W\ Hz^{-1}m^{-3}sr^{-1}]$

5.6.1. Individual Uncertainty Analysis

The impact of each uncertainty on the horizontal polarization are discussed here.

Time offset The drifting oscillator causes a displacement of the brightness model, and thus mostly affects the regions close to the limb crossing. Due to the strong temperature gradient at the limb of the disk, even small offset can cause large residuals. Nevertheless, a time-offset causes a residual pair for each scan across the limb of the planet. Whereas when entering onto the limb, a positive offset will cause a negative residual, it will equally result in a negative residual when leaving the limb of the planet. Since the effect always comes in a pair, they cancel to first order and the impact on the integrated flux density is small. This can be seen when looking at the small error bars in Figure 5.15a.

Beam x-offset The same effect can also be observed for the x-offset, where to first order the residuals cancel. Nevertheless, there are a few scans that show larger variability Figure 5.15b. These are the result of large negative residuals when the solution is far from the optimum. Disregarding the large residuals, the curves show little sensitivity to the x-offset. Note, that the lack of positive error bars indicates, that variations in the

x-offset artificially decrease the retrieved flux density.

Beam y-offset The y-offset affects the residuals at the poles of the Jupiter and has a slightly larger impact on the beaming curve, with examples where it increases and decreases the flux density (see Figure 5.16a. Postive-only error bars indicate that the solution is in a valley, and a step in either direction results in a larger flux density, as seen for the first half of the scan. The larger residuals at the end of the scan are caused by outliers again.

Limb darkening coefficent Recalling the analysis of the limb darkening coefficient from Section 5.1, the limb darkening coefficient converged to lowest values in the solution space of p = 0.05. Increasing the limb darkening coefficients reduces the thermal emission from the poles and result in stronger polar residuals. This causes a positive correlation between the limb-darkening coefficient and the flux density as seen by the large error bars in Figure 5.16b. The maximum value of the limb-darkening coefficient of p =0.09, results in an increase in flux density by as much as 30%. Note that the y-axis was adjusted to accommodate these large residuals. As discussed in Section 5.3, the solution of the limb darkening is robust, as shown by the lack of polar residuals for the vertical polarization.

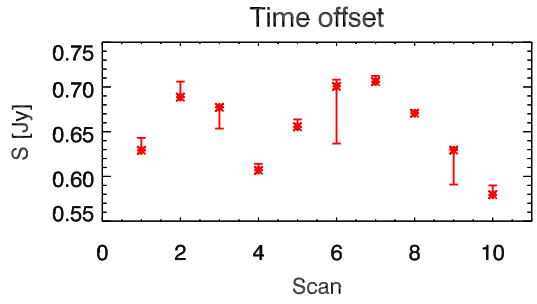

(a) Oscillator drift: dt 0 to 0.5 [s]

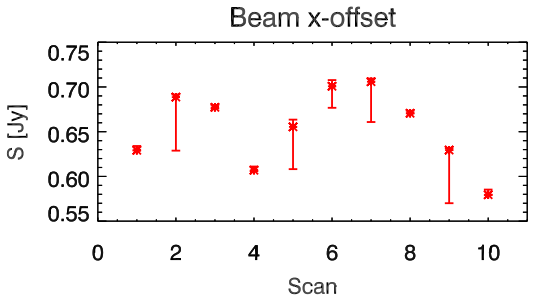

(b) Beam x-offset: dx = 0.35 to 0.44 [mrad]

Figure 5.15: Impact of the uncertainties on the beaming curve

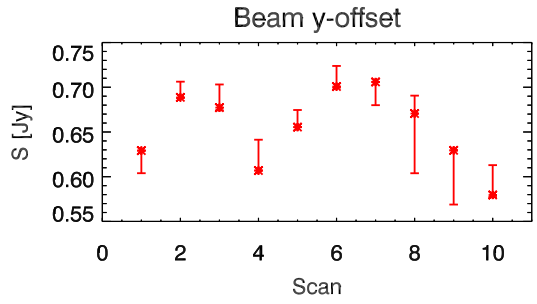

(a) Beam y-offset: dy = 0.53 to 0.62 [mrad]

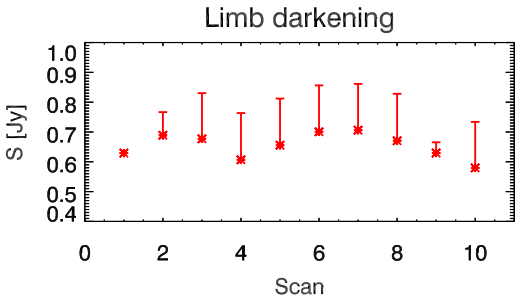

(b) North-South limb darkening: p = 0.05 to 0.09 [-]

Figure 5.16: Impact of the uncertainties on the beaming curve

Brightness temperature The sensitivity of the flux density to the nadir brightness temperature warrants a longer discussion. As seen in Figure 5.17, changing the nadir brightness temperature of Jupiter between 160 and 163 K has a significant impact on the retrieved flux density. The anti-correlation of brightness temperature with flux density is further exemplified in Figure 5.17b, where the flux density is calculated across the brightness temperature solution space. The blue curve gives the magnitude of the compound cost function and converges at 161.25 K. As expected, with increasing distance from the optimum, the cost function increases steeply. The flux density (red dots) decreases with increasing brightness temperature, with a gradient

of $0.1\,Jy/K$.
Before jumping to a conclusion, this sensitivity has to be critically evaluated. One might expect that the brightness model of Jupiter controls mainly the emission in the vicinity of the disk of Jupiter, but when the beam is far from the planet, it should have little impact. This statement is correct for most synchrotron observations with ground-based interferometry and has been demonstrated before [Kloosterman et al., 2008]. For interferometers, the HPBW is often small compared to the disk of Jupiter, and when the beam is centered on the main synchrotron emission region, the influence of Jupiter is indeed small. In this case, a large sensitivity to the brightness model would, therefore, indicate excessive signal in front of the disk; and thus hints at a retrieval artifact, rather than a signal.

For Cassini RADAR, the footprint of the beam at flyby distances is slightly exceeding a radius of Jupiter, and when centered on the main emission lobe of Jupiter ($1.5R_J$), the main beam is just of the disk of Jupiter. As detailed in Chapter 4, the Cassini RADAR beam also has relatively large sidelobe contributions, and even though the main beam is off the planet, the large size of Jupiter fills a large section of the side lobes. The excellent knowledge of the side beams allows for quantifying this impact and removing it accordingly, however, the early retrieval suffered from poor knowledge of the exact shape of the side lobes. Considering that at 1.5 R_J, the thermal contribution leaking in through the side lobes is a factor of 5 larger than the synchrotron signal, it is clear that a misrepresentation of Jupiter's thermal contribution can have a significant impact on the synchrotron flux density. In conclusion, it is not the signal in front of the disk that causes the considerable changes in the integrated flux density, but the thermal signal leaking in through the side lobes while mapping the main emission regions.
The initial retrieval overestimated the brightness temperature as seen by large negative residuals on the disk of Jupiter [Janssen et al., 2001]. The impact of the negative residuals was mitigated by excluding them from the integration of the flux density, however, the secondary impact on the main emission region through the side lobes was not accounted for. This was probably the largest factor that caused the extreme depletion of electrons as concluded by the initial retrieval.

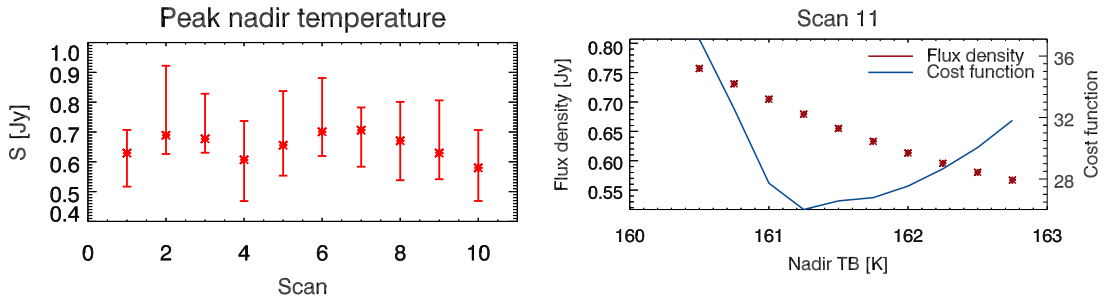

(a) Nadir brightness temperature: T = 160 to 163 [K] (b) Impact on Scan 11

Figure 5.17: Impact of Jupiter's nadir brightness temperature on the beaming curve.

Impact of the chosen brightness model In Chapter 4, three different brightness models were discussed. The simple uniform brightness model delivers unrealistic results due to the misrepresentation of the signal towards the limb. The resulting synchrotron results are severaly altered by the limb residuals and thus the model was quickly abandoned.
For sake of brevity, only the impact on the horizontal polarization is shown. Figure 5.18a provides the nominal map based on the best-fit model obtained through the MCMC. Juxtaposed to the nominal maps is the result of changing the MCMC weights (polar signal was reduced by a factor of two, magnetic axis crossing increased by a factor of two). The difference in flux density is less than 0.01 Jy, indicating that the maps are not very sensitive to the chosen MCMC weights.
When changing major parameters in the brightness model, the impact is more drastic. In Figure 5.19a the brightness model used the lower resolution 2000 zonal scans (see Chapter 4 and Appendix A). The direct impact can be seen by negative residuals on the southern hemisphere, nevertheless, the calculated flux density is only fractionally smaller: 0.61 Jy compared to the 0.64 Jy for the nominal maps. This is a consequence of

the large beam size, that is very insensitive to small zonal variations.
The largest impact comes from changing the underlying base model the solar abundance model [de Pater et al., 2001] as seen in Figure 5.19b. The rotationally averaged flux density of this map is 0.80 Jy and thus clearly deviates from the nominal maps.

This analysis confirms that the results of the retrieval are insensitive to the chosen MCMC weights, however, the thermal brightness model can significantly alter the results.

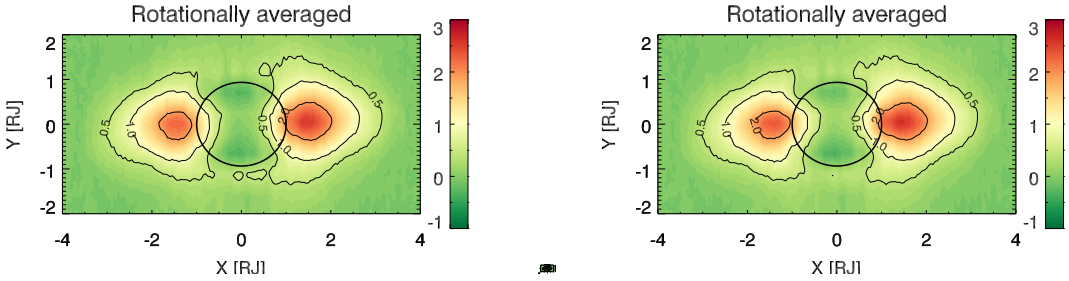

(a) Nominal combination (b) Change in MCMC weights

Figure 5.18: Changes in the rotationally averaged map when changing the MCMC weights. The flux density of both maps are comparable.

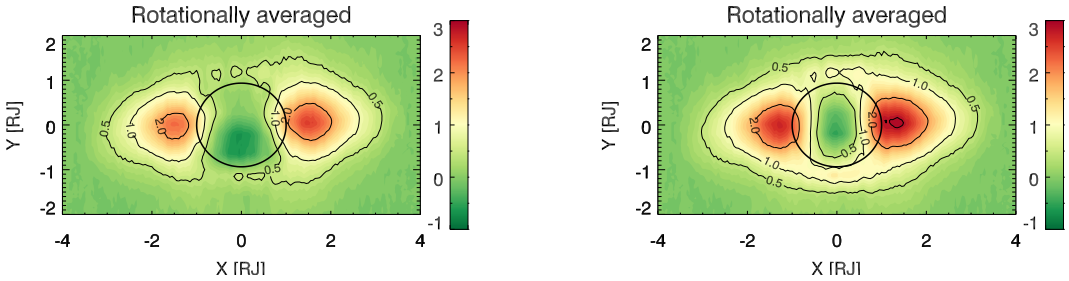

(a) VLA 2000 zonal structure (b) Solar abuandance volatiles [de Pater et al., 2001].

Figure 5.19: Changes in the rotationally averaged map when the zonal temperature profile, and the underlying solar abundance model.

5.6.2. Compound Analysis

It was highlighted in Chapter 4, that the weights applied for the compound cost-function of the MCMC require fine-tuning and thus are biased by a-priori knowledge. This is a problem that all optimization share, where the cost function is not clearly defined. Instead of computing the flux density only for a best-fit, it is computed for a range of combinations that result in similar cost function magnitudes. The range of uncertainties was presented at the beginning of the chapter Section 5.1 and is the basis for the sensitivity analysis presented here. The larger the spread in the computed flux density, the lower is the confidence in the solution. Contrary, if different combinations of uncertainty parameters converge to a similar solution, the flux density estimate can be considered robust.
The rotationally averaged maps are very robust to the uncertainties, as they mostly affect small details close to the limb of the planet, whose impact is reduced during the averaging process. Figure 5.27 displays the 1-σ variation in computed flux density for the top 10 solutions found by the MCMC, and indicates that flux density is also not very sensitive to the results.
The low emission characteristics of the vertical polarization (synchrotron brightness temperatures of 1 K) is reflected by the wide divergence in the top 10 solutions as seen in Figure 5.20a. This indicates that the MCMC has trouble converging to a solution, rendering the solution sensitive. Nevertheless, the 1-σ variations are around $\pm$0.03 Jy, and are at an acceptable level.
The stronger emission received from the horizontal polarization scans results in a narrower variations in the

top 10, where 1-σ variations are of the order of ± 0.02 Jy. Nevertheless, compared to the sensitivity found in detailed analysis, this variability is small and a sign that the solution converged to the true optimum.

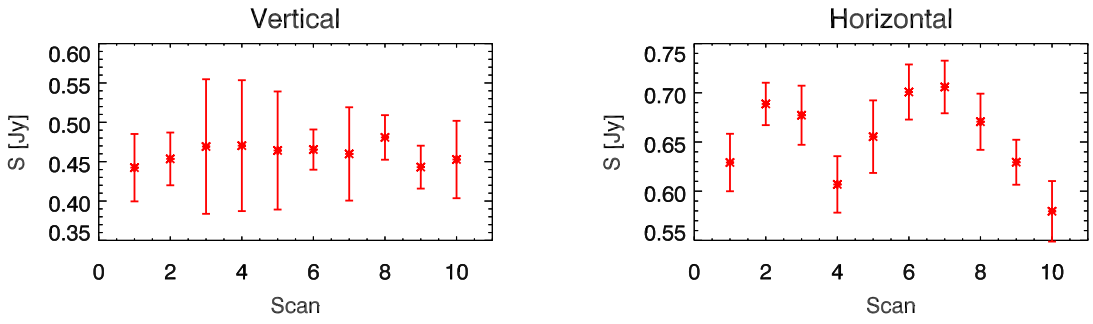

(a) Vertical polarization

(b) Horizontal polarization

Figure 5.20: Standard deviation variations derived from the MCMC solution space

When adding the two polarizations to form the beaming curve, the uncertainties are assumed to be uncorrelated and thus the uncertainties for the beaming curve are given by the root mean square of the two set of one σ variations. The results can be found in Figure 5.21, which gives the individual measurment points and the beaming curve constructed from the best-fit courier coefficient of Section 5.4.

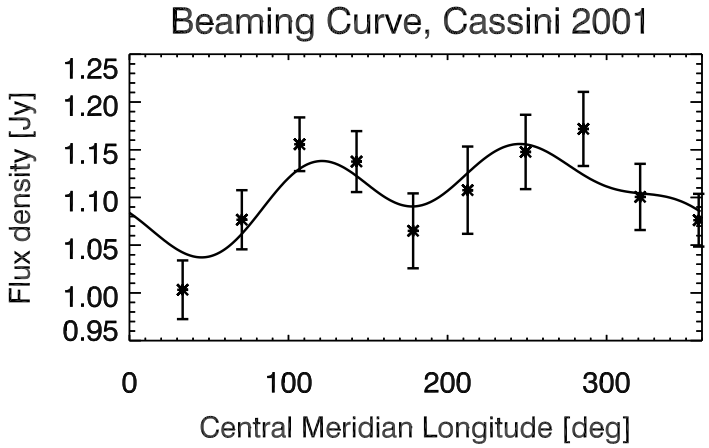

Figure 5.21: The variability of the solution obtained from the range of MCMC solutions. The solid lines gives the beaming curve obtained from fitting the measurements to the first three terms of the Fourier expansion.

Testing for the impact of the MCMC weights The robustness of the solution to the chosen MCMC weights can be achieved by running the optimzation with different weights for the various regions, and ideally the computed signal should be relatively stable despite different optimization priorities. The horizontal beaming curve is used to visualize the impact as seen in Figure 5.22. These two panels should be compared with Figure 5.20b, which presents the nominal case. The double-peak structure is recognizable across the two verification cases, albeit to a lesser degree. The rotationally averaged integrated flux density of the two verification curves was calculate to be 0.64 Jy and 0.66Jy, which compares excellently to the beaming curve of the nominal case of 0.65 Jy. This provides evidence that the final weights are not as crucial as initially expected.

5.7. Uncertainty of the Final Results

The last quantity remaining is the integrated flux density, average over the full rotation. This quantities has already be obtained by fitting the measurements to the beaming curve, however, quantifying the uncertainty

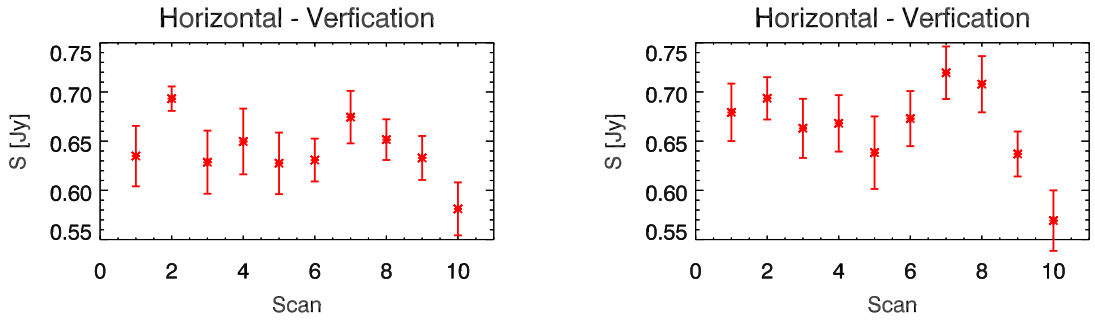

(a) Increased weight for the magnetic axis crossing, reduced weight for the residuals above the poles.

(b) Increased weight used for the signal in front of the disk, forcing a brigher Jupiter model.

Figure 5.22: Horizontal beaming curve for different weights chosen of the MCMC.

requires an understanding of all applicable error sources.

MCMC variations The flux density was obtained for the top 10 solutions in Section 5.6, and the results are given in Figure 5.21. The impact of these uncertainties on the parameters can be obtained by propagating the individual uncertainties [Hansen et al., 2012]. For the linear system, $AX = B$, σ_B are the uncertainties in the true value, in this case the root mean square variation in flux density obtained from the MCMC solution analysis. The covariance matrix for the solution is then obtained:

$$COV_x = \left(A^T\ A\right)^{-1} A^T \sigma_B^2 A \left(A^T\ A\right)^{-1} \tag{5.2}$$

Where the diagonal entries are the correspond to the uncertainties in the retrieved parameters in units of Jy.

Radiometer noise formula The intrinsic noise of an radiometer is controlled by the systematics of the instrument. It is given by [Janssen, 1993]:

$$\Delta T_{RN} = \frac{T_S}{B_R t} \tag{5.3}$$

where,

$\boldsymbol{T_{RN}}$ $[K]$ Radiometer noise
$\boldsymbol{T_S}$ $[K] \approx 700$, Estimate of the system temperature when observing the main synchrotron radiation
$\boldsymbol{B_R}$ $[Hz]$ 135 10^6, Bandwidth of radiometer
$\boldsymbol{t}$ $[s]$ 0.95, Integration time per measurment

Calibration factor The calibration factor is obtained for observations of a known brightness source at thermal equilibrium. This was performed separately at Jupiter and Saturn reflecting on the changing thermal conditions with increasing distance to the sun. The absolute calibration, however, was obtained based on the Titan's temperature and the Saturn factor might be more applicable. Since no further scans of Jupiter are possible to test the impact, the difference is included in the estimate of the uncertainty.

$$\Delta T_{cal} = \left(\frac{cal_{Saturn}}{cal_{Jupiter}} - 1\right) * T_{syn} \tag{5.4}$$

where,

$\boldsymbol{\Delta T_{cal}}$ $[K]$ Temperature variations due to the calibration constant
$\boldsymbol{cal_{Saturn}}$ $[-]$ 203.5, Estimate of the calibration constant based on Titan scans at Saturn
$\boldsymbol{cal_{Jupiter}}$ $[-]$ 206.2, Estimate of the calibration constant based on early Jupiter scans
$\boldsymbol{T_{syn}}$ $[K]$ Maximum synchrotron temperature

Table 5.4: Cassini error estimate in Jansky

Radiometer	Calibration	Cal. scale factor	Beaming curve 3-σ	RMS	Worst case
0.020	0.009	0.013	0.033	0.041	0.074

Absolute calibration The absolute calibration knowledge is determined from the knowledge of the calibration sources, which was given by Titan's surface temperature. The latest estimates indicate that the calibration of Cassini RADAR is at the 1% level [Janssen et al., 2016], which is the value used for this research.

Total uncertainty The total uncertainty can be obtained by combining the various uncertainties. The various parameters are tabulated in Table 5.4.

5.8. Comparison with Other Observations

Comparison of the results obtained from the Cassini measurements with other observations can be used to validate the observations, but also can highlight regions that are abnormal.

5.8.1. Spetral Flux Density

The Cassini frequency probes the ultra-relativistic electron population at Jupiter, however, allows limited insights into the behavior of lower energy particles. Probing the full magnetosphere requires observations at a range of different frequencies. The flyby in 2001 was accompanied by ground-based measurements using the VLA [Bolton et al., 2002, Janssen et al., 2001, Santos-Costa et al., 2014], GAVRT and Deep Space Network [Klein et al., 2001]. Unfortunately, the VLA in 2001 was in the A configuration with the longest baselines. The large antenna spacing allows for an excellent resolution, at the cost of resolving part of the synchrotron emission region. Especially, the L-band measurements (1.4 GHz) are compromised by this effect, where the missing short spacing was corrected based on model calculations [de Pater and Dunn, 2003]. The longer wavelength at P-band mitigates this effect, and only small corrections are required from the VLA observations, which renders the measurements more reliable. The integrated flux densities were obtained from the raw measurements as used and provided by Santos-Costa et al. [2014] and their magnitude was re-computed using the beaming curve coefficients for a set of observations [Klein et al., 1989]. The zeroth order coefficient of the beaming curve can be found in Table 5.5.

Single dish measurements such as Cassini and the Deep Space Network (DSN), do not resolve part of the source at the relevant distances and as such are better suited for obtaining the integrated flux density. The DSN has long be used in the Jupiter Patrol Program to observe the long-term variability in the synchrotron flux. Unfortunately, no measurements were obtained on the 2-3 of January but an estimate could be reconstructed by interpolating between adjacent measurements [Klein et al., 2001].

The Cassini measurement completes the spectrum at high frequencies, where the new measurement point has a flux density a factor 2.5 higher compared to the initial estimate. Also, through the extensive analysis, the uncertainties were reduced considerably, and are reflected by the small error bars.

Based on these measurements, the flux density spectrum can be established and is compared to other measurement campaigns in Figure 5.23. The blue and red line correspond to measurements from 1994 and 1998, to which a synchrotron model was fit [de Pater et al., 2003]. These measurements are the result of a worldwide campaign, which involved observations at many different frequencies. The synchrotron model was then fit to the observations to obtain information on the electron population, most notably their energy distribution. Whereas there are plenty of observations at lower frequencies, at higher frequencies, the increased thermal contribution requires good knowledge of the Jovian brightness distribution to retrieve the synchrotron flux. Only recently, there is enough information on the ammonia abundance at Jupiter, so that flux density can be retrieved confidentially even at higher frequencies. The low flux density as obtained by the initial retrieval resulted in further research studying the high-energy electron population of Jupiter. The black dots are obtained from VLA maps in 1991 [de Pater and Dunn, 2003], and the orange dot are obtained from more recent maps in 2004 by Kloosterman et al. [2008].

Unfortunately, there was no time for modeling the synchrotron flux based on the recomputed 2001 measurements. While trying to explain the electron depletion, de Pater and Dunn [2003] simulated the synchrotron radiation for various conditions. The details of the simulation can be found in [de Pater, 1981a, de Pater and Dunn, 2003, de Pater et al., 1997]. The green curve as shown in Figure 5.23 is one of these simulations, for the

Table 5.5: Information on the measurment campaigns for establishing the flux density spectrum.

Observatory	ν (GHz)	S (Jy)	Comments	Source
		1991		
VLA, D-configuration	15	1.5 ± 0.15		[de Pater and Dunn, 2003]
VLA, D-configuration	22	1.5 ± 0.4		
		1994		
Multi-observatory	See Table 1 of reference for details			[de Pater et al., 2003]
		1998		
Multi-observatory	See Table 1 of reference for details			[de Pater et al., 2003]
		2001		
VLA, A-configuration	0.3	6.41 ± 0.40	Derived from the beaming curve	[Santos-Costa et al., 2014]
VLA, A-configuration	1.4	4.1 ± 0.43	Derived from the beaming curve	[Santos-Costa et al., 2014]
Deep Space Network	2.3	4.02 ± 0.08	Single dish measurement	[Bolton et al., 2002]
Cassini	13.8	1.10 ± 0.07	Single dish measurement	This work
		2004		
VLA, D-configuration	15	1.26 ± 0.12		[Kloosterman et al., 2008]

following conditions:

- Lifetime against losses of 6×10^7 $[s]$
- Diffusion parameter, D_0 of 3.5×10^{-9} $[1/s]$
- Energy spectrum defined by the parameters a = 0.4, b = 3.0 and E_0 = 100 MeV, so that phase space density at L = 6 in the equator is given by $j(E) \propto E^{-a} + (1 + E/E_0)^{-b}$.
- The main change to the other models came from the cutoff energy E_{max} = 40 MeV, that describes the maximum energy level considered in the integration. This value is a factor of 2.5 lower than the curves fit to the other spectra.

Superimposing this curve shows an excellent agreement between the model's curve and the 2001 observations. This is a strong indication that there is indeed a strong depletion of high energy particles, however, less severe as predicted by the initital retrieval.

5.9. Comparison with Other Radio Maps

The following sections are devoted to comparing the rotationally averaged maps of Cassini to other observations. The maps differ in measurement epoch, frequency and viewing geometry and these differences have to kept in mind when comparing the maps.

Resolution adjustment Despite the relatively close observation distance of ~ 149 R_J, the Cassini beam size cannot compete with the resolution from ground-based antenna arrays, which make use of large antenna spacing to decrease the beam size. Therefore, the VLA observation even at a maximum distance between Jupiter and Earth can retrieve finer structure than the Cassini spacecraft. A direct comparison between the maps, therefore, requires degrading the resolution of the maps to match the Cassini half-power beam width. The degradation of the maps is based on the convolution theorem [Hirschman and Widder, 2012], that specifies that the convolution of Gaussian results in a Gaussian. The high-resolution VLA maps are constructed using Multichannel Image Reconstruction Image Analysis and Display (MIRIAD) [Sault et al., 1995] and the clean image are restored with symmetric Gaussian beams (see [Santos-Costa et al., 2014] for more details of the retrieval). This is the starting point for the algorithm to degrade the maps to the Cassini resolution:

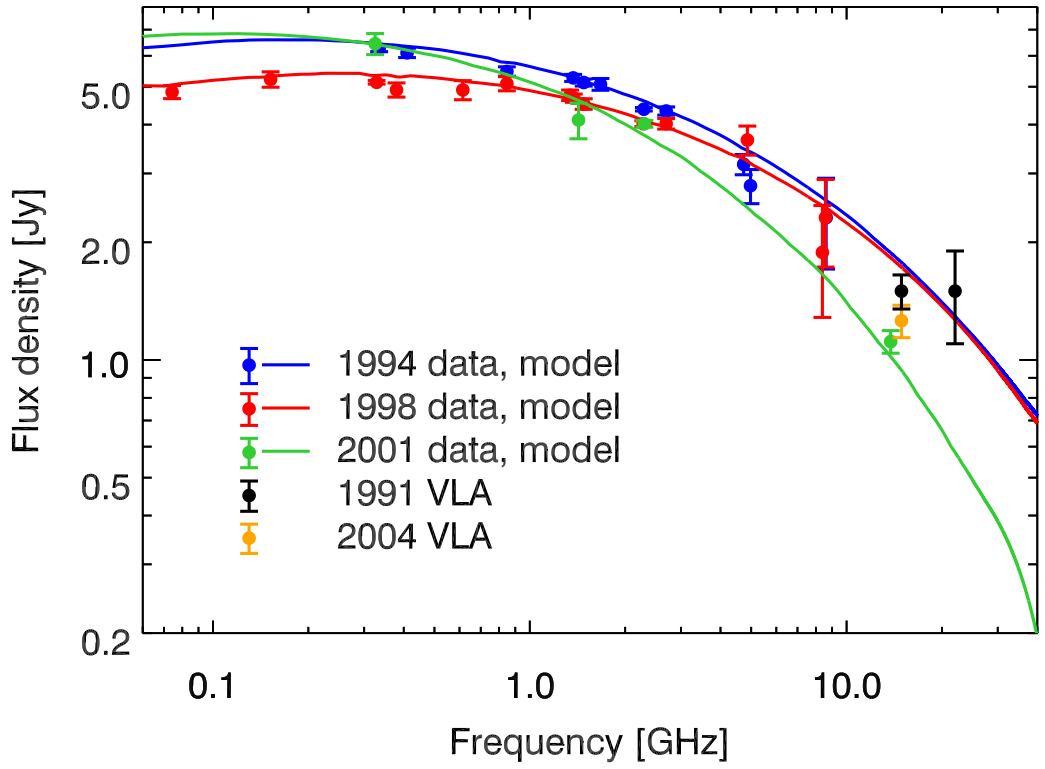

Figure 5.23: Flux density spectrum for the 2001 measurement campgain, the 2001 model curve is obtained from [de Pater and Dunn, 2003] and the results are compared to spectra obtained at different epochs. For more information on the measurement points see Table 5.5

1. Calculate the size of the Cassini footprint on Jupiter based on the half-power beam width and the flyby distance. The footprint diameter is changing as Cassini is slowly receding from Jupiter, but the variations are small, and thus the average flyby distance of 149 R_J was used.

2. Outside of the radio astronomy, Gaussian distribution are defined by the standard deviation, which describes the distance from the center in which 68% of all data points fall, whereas the half power beam width is defined as the distance where the intensity drops the half the peak value. An example of this relationship is visualized in Figure 5.24. The following calculations are done in standard deviation, whereas the results are given in half-power beam width to adhere to the radio-astronomy standard.

3. The convolution theorem specifies that two successive convolutions (VLA and SYN) are equivalent to a single convolution (CAS) if their standard deviations have the following property: $\sigma^2_{CAS} = \sigma^2_{VLA} + \sigma^2_{SYN}$. In case of the VLA, this requires convolving the original maps with a synthesis beam ($_{SYN}$) to match the resolution of the Cassini beam ($_{CAS}$).

4. The Gaussian Kernel is then constructed using the calculated standard deviation, truncated at 3σ to minimize the computational extend of the convolution. The in-built IDL CONVOL_FFT routine is used for the calculations.

5. The resulting maps are the beam averaged brightness temperature or the equivalent flux that is received by the beam in units of $Jy/beam$. The lower resolution results in more shallow peaks, as the total energy is conserved in the processes, however, appears more spread out. The high-latitude emission rings are among the features that disappear in the convolution processes.

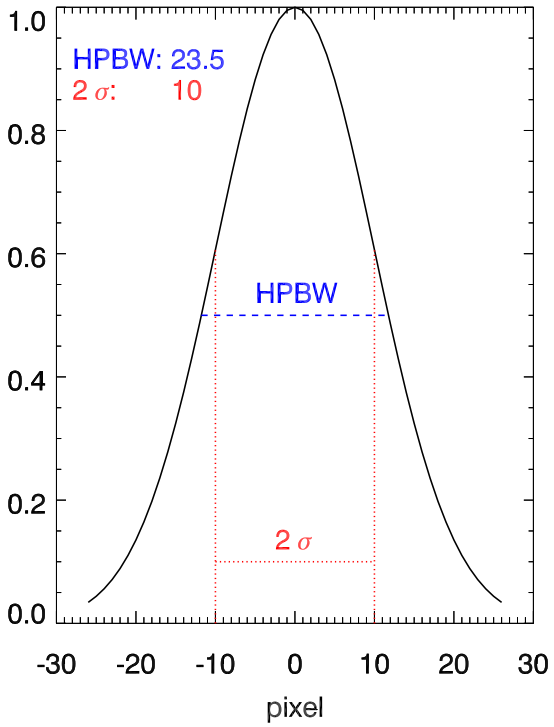

Figure 5.24: Relationship between the half-power beam width and the standard deviation.

Normalization This section focuses on a comparison of maps obtained at a similar frequency. The electrons emit at many different frequencies, however, the synchrotron spectrum is peaked at the critical frequency, $\nu \sim E^2 B$ [Ginzburg and Syrovatskii, 1965]. Consequently, the higher the frequency of observations, the higher is the energy of the probed electrons. The electron population follows a power law so that at higher energies there are fewer particles that emit. This results in lower energies recorded at higher frequencies as see in Figure 5.23. Comparing maps in units of brightness temperature or flux density, therefore, is dominated by the magnitude of the flux density, and does not reveal information about the detailed structure. This detailed structure, however, indicates changes in the electron distribution and, therefore, the maps have to be converted into comparable quantities. Two options are available for that:

- Scaling: The flux density spectrum describes the relationship between frequency and total power emitted. Using this flux density spectrum, a scale factor can be devised to compare maps, and allowing for comparing maps in absolute brightness units after adjusting the brightness temperature using the Rayleigh-Jeans approximation. Problems arise when comparing maps at different epochs, as the spectral index are known to vary [de Pater et al., 2003], and the 2001 measurements confirm that the spectral index can vary considerably. The variability in the spectrum is most pronounced in the low and high frequencies [de Pater et al., 2003, Santos-Costa and Bolton, 2008], rendering this method very sensitive to temporal changes. As seen in Figure 5.25a, the method works very well when comparing maps at nearby frequencies, however, fails to produce satisfactory results for large frequency differences. The comparison between high (green and gray) and low-frequency (red and blue) measurements is, therefore, dominated by the difference in magnitude, and does not reveal any information on the structure of the synchrotron.

- Normalization: The maximum flux for the synchrotron radiation is recorded across all frequencies in the equatorial emission lobes at ~ 1.5 R_J, which can be used to normalize the maps. The advantage of the normalization is its universal use regardless of measurement epoch or frequencies. There is observational evidence that the electron distribution is independent of the energy of the electrons [de Pater et al., 2003] so that the normalized maps are similar in structure as well. Nevertheless, there are some

fundamental differences, and it is important to distinguish between effects introduced by the normalization and physical changes in the magnetosphere.
Whereas the lower energy particles can found throughout the magnetosphere, especially the energetic particles are concentrated close to the planet. Further outwards, at regions of lower magnetic field strength, these particles haven not yet undergone sufficient acceleration. Recalling that emission frequency and power are dependent on $\sim E^2B$ and $\sim E^2B^2$, results in a concentration of high-frequency emissions close to the planet. The high-frequency emissions are expected to show a steeper radially fall off in the equator, compared to a more gradual decrease and a further radial extent of the low-frequency measurements. This effect can be seen in Figure 5.25b, where with the lowest frequency measurements (VLA-P) has the widest reach, and the intensity drops quicker with higher frequencies.
Similarly, as electrons bounce to the higher latitudes, they are accelerated and gyrate in regions of high magnetic field strength. It is, therefore, expected that at higher frequencies these emissions appear enhanced.

Therefore, for comparison between nearby frequencies both the scaled and normalized maps will be used to highlights differences in the map. However, for comparison between the low-frequency measurements with the Cassini measurements, only the normalized maps will be used. As discussed the normalization of the maps can cause systematic artifacts, such as an enhancement at the poles. This effect can be mitigated by comparing how the normalized maps change over time. As both maps share the same systematic artifacts, any change in the structure must be of temporal nature.

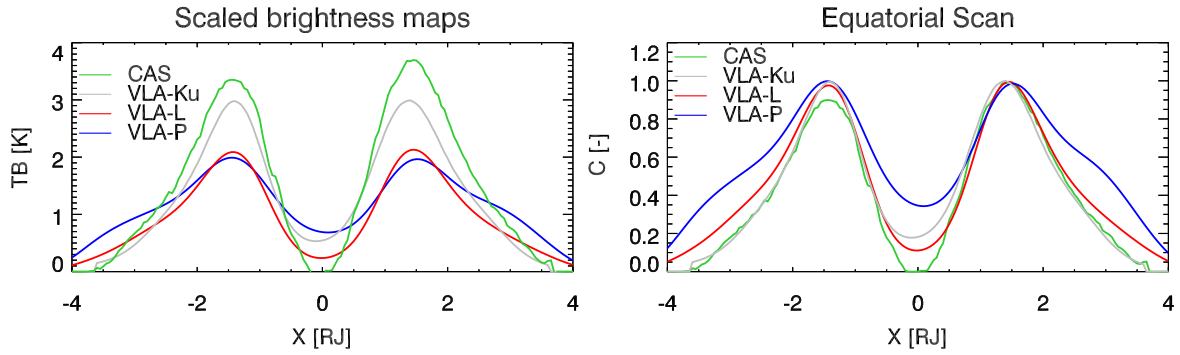

(a) Scaling (b) Normalization

Figure 5.25: Comparison between equatorial cuts. The different colors refer to the various rotationally averaged maps (CAS = Cassini, VLA-Ku = 14.9 GHz, VLA-L = 1.4 GHz, and VLA-P = 0.3 GHz. See the text for the discussion of the two methods. Note that around 2.5 R_J one can identify the shoulder, indicative of Amalthea's influence on the radio emission for the lower frequency measurments.

5.9.1. VLA, K-band, 2004

The details of the VLA observations [Kloosterman et al., 2008] can be found in Table 5.6. The declination of the observer is known to influence the fine structure of the radio maps. Fortunately, the declination of the observer for both campaigns (-1.7° compared to -1.5°) matches, so that viewing geometry should not influence the map comparison.
Regarding the probed electron population, both observations probe the most energetic particles in the Jovian magnetosphere. At the Cassini's frequency of 13.8 GHz, the spacecraft is sensitive to electrons with kinetic energies of ≈ 45 MeV (corresponding magnetic field strength ≈ 1.5 Gauss at the 1.5 R_J). In comparison, the VLA observations are mapping the electrons around 47 MeV; in essence the same electron population.
Despite the modest difference in frequency, the flux density and equivalent brightness temperature already differ by 8% and 20%, respecitively based model predictions (green line in Figure 5.23).
The original maps (rotationally averaged) can be found in Figure 5.26a converted in units of brightness temperature. Despite the large distance of 6.08 AU, the high-latitude emission rings can be identified. Whereas the right side of the planet compares well with lower frequency maps, the right side of the planet appears extended. Note that Kloosterman et al. [2008] stated that the structure in front of the disk should be disregarded, as the subtracted thermal disk did not include the zone-belt structure. This effect is preserved when the maps are degraded to match the Cassini resolution in Figure 5.26b. These maps cannot be scaled (see Figure 5.27a) or normalized (see Figure 5.27b) and compared to the Cassini maps. A positive enhancement

indicates that Cassini is brighter.
Since the frequency of the observations is comparable, the scaled maps and the normalized maps share many features. Whereas the equatorial region compares relatively well, the outstanding feature is the enhancement at high latitudes. It's important to point out, that the VLA measurements are taken at a higher frequency, and therefore systematic effects should render them brighter at higher latitudes, as detailed above. Nevertheless, the comparison highlights that the Cassini maps are brighter towards the poles, suggesting that especially the higher latitudes regions have undergone significant changes. The enhancement is concentrated around the latitudes of the high emission rings, and therefore supports the hypothesis of Santos-Costa et al. [2014] that at the time of the flyby the Jovian magnetosphere was profoundly disturbed. Furthermore, the fact regional enhancement is an indication that scattering occurs preferentially inwards of Amalthea. By localizing regions where the changes occurred, certain processes can be ruled out from the explanation. This is indicative that the scattering processes inside of Amalthea are more efficient at redistributing the particles. For a detailed discussion see Chapter 6.

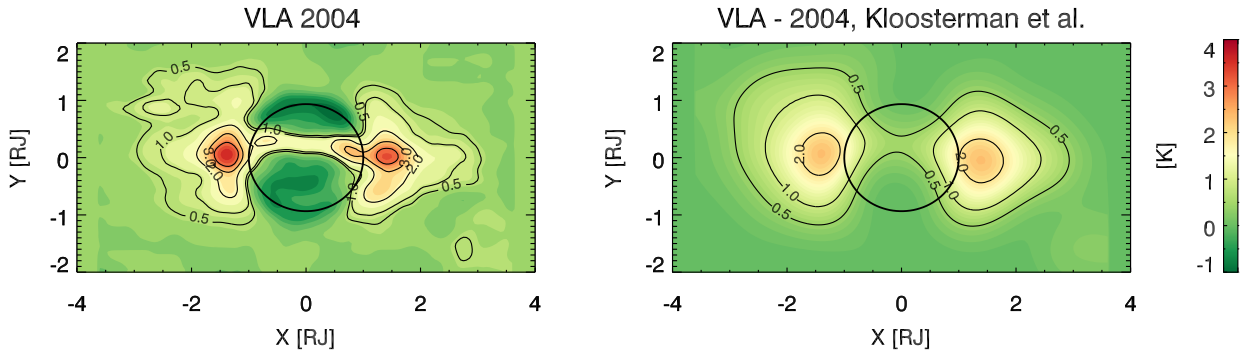

(a) Native resolution

(b) Convolved with the Cassini beam

Figure 5.26: VLA 2004 synchrotron maps after subtracting Jupiter's thermal emission using the MIRIAD-UVDED model [Kloosterman et al., 2008]

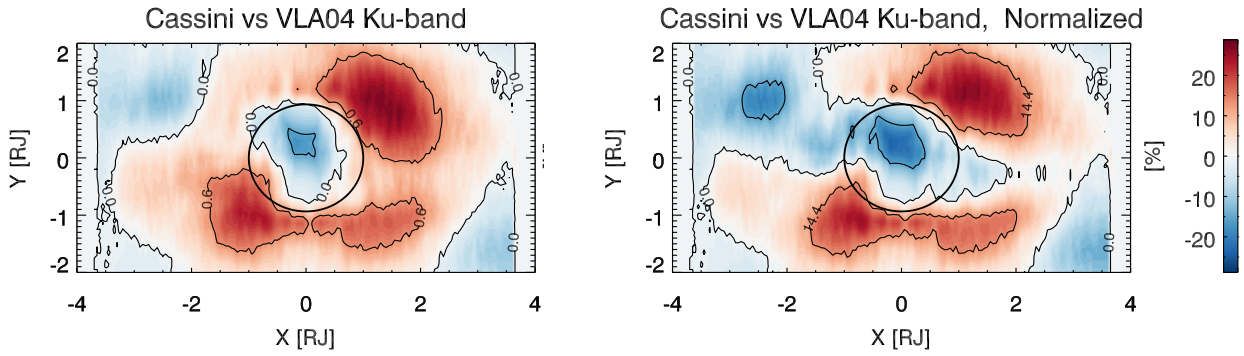

(a) Difference in absolute brightness

(b) Difference between the normalized maps

Figure 5.27: Comparison between high frequency maps [Kloosterman et al., 2008]

5.10. Comparison with 2001 Measurements

The 2001 flyby was accompanied with ground-based efforts to map the synchrotron radiation across different frequencies. Santos-Costa et al. [2014] have performed an excellent analysis on the original data [Bolton et al., 2002, Janssen et al., 2001, Klein et al., 2001] and the reader is referred to the original publications for an in-depth analysis. The main conclusion of the comparative study found that the magnetosphere was significantly altered during the time of the flyby. Whereas the equatorial zones were found to be weaker than previous maps, the overall extent of the radiation belt was increased with enhancement in the high latitude regions. Interestingly, the authors argue that the main variations occurred beyond the outer ring edge and Amalthea, a region where electrons are scattered into higher latitude rings [Dulk et al., 1997].

Table 5.6: Relevant information on the maps that are used for the comparison with the Cassini measurements. S. beam refers to the synthesis beam used for degrading the maps. Source key: J01 [Janssen et al., 2001], K08 [Kloosterman et al., 2008], and S14 [Santos-Costa et al., 2014].

Date	ν	VLA	D_E	D	Disk	CML	Beam	S. beam	Source
	(GHz)		(deg)	(AU)	(arcsec)	(deg)	(arcsec)	(arcsec)	
Jan-01	Ka (13.8)	-	-1.5	0.07	2750	full rotation	1296.0	-	J01
Jul-04	Ku (14.9)	D	-1.72	6.08	32.77	131-261, 29-50	6.00	13.84	K08
Jan-01	P (0.3)	A	3.44	4.26	46.26	full rotation	6.06	21.87	S14
Jan-01	L (1.4)	A	3.44	4.26	46.26	full rotation	3.61	22.41	S14
Dec-88	P(0.3)	A	3.58	4.16	47.41	95 - 336	6.20	21.83	S14
Dec-88	L (1.4)	A	3.58	4.16	47.41	95 - 336	3.70	22.39	S14

Due to the large difference in frequencies only the normalized maps are shown, as the scaled maps were dominated by signal strength rather than the fine structure. Figure 5.29a demonstrates the difference between the Cassini measurement and the low-frequency measurement in the P-band (0.3 GHz), where the color red denotes an enhancement of the high-frequency measurements of Cassini RADAR. At these frequencies, the electron population that is an order of magnitude less energetic than the Cassini measurements is mapped, and thus the maps electrons should be more spatially distributed. The maps confirm this hypothesis as indicated by the blue spots in the equatorial region. At these regions, particles have not yet diffused inwards enough to reach the energy levels of Cassini's sensitivity. At the poles, the strong magnetic field leads to particles being accelerated to large energy levels, as their adiabatic invariant is conserved. As a consequence, these particles emit at higher energies, and some enhancement is intrinsic to the comparison at different frequencies. This observation alone does not suffice as an explanation for more particles distributed into the high latitude rings.
The comparison with the measurements at 1.4 GHz (L-band) allows more insights. The fine structure as seen in Figure 5.29b clearly reveals localized regions of enhancement and depletion. The depletion in the equatorial region at distances outside of Amalthea (R > 3) is a result of the same mechanism as explained before. Of more interest are the intensifications at higher latitudes, which occur predominantly around the high latitude rings. With increasing latitude, the magnetic field strength growth, resulting in electrons emitting more power and at higher frequencies. As dicussed before, this presents a systematic bias, that should be kept in mind when analyzing the maps. Nevertheless, the spatial agreement between the high latitude rings and stronger emission features can also hint at processes that preferentially scatter energetic particles to higher latitudes. Such an energy depenent scattering process will be discussed in Chapter 6.

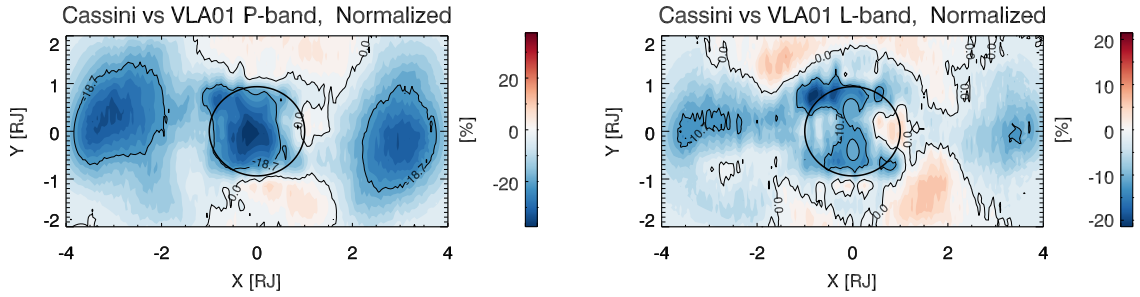

(a) VLA P-band (0.3 GHz)

(b) VLA L-band (1.4 GHz)

Figure 5.28: Comparison between high frequency maps [Santos-Costa et al., 2014]

5.11. Comparison with 1988 Measurements

The bias as introduced by the normalization in the maps can be addressed by comparing changes in similarly normalized maps. The ideal candidate for this comparison are maps that were taken at similar viewing geometries and VLA array configuration, such as the VLA radio images from 1988 Santos-Costa et al. [2014].

Therefore, any changes in structure seen between these maps is of temporal nature, as all other factors are kept constant. This allows analyzing changes in the electron distribution. The second set of normalized maps is shown in Figure 5.29.
The P-band measurements compare relatively well with the 2001 maps, indicating that the lower frequency portion has not undergone drastic changes. The higher latitude rings show up slightly brighter, meaning that in 2001 the low energy particles were also scattered, however, the changes are small. The lower degree of depletion in the equatorial zone indicates that the belts were not as spatially extended as they were in 2001, confirming the conclusion of Santos-Costa et al. [2014].
The most interesting comparison stems from the normalized L-band measurements. The equatorial zone does no longer appear depleted. The Cassini measurement should naturally image fewer particles at distances around $2.5R_J$ as explained above due to the limited diffusion. The lack of depletion, therefore, leads to the conclusion that there was an excessive number of high energy particles present in the vicinity of the moon of Amalthea. It must be cautioned that the low flux density recorded in the 1988 [Santos-Costa et al., 2014] (a 25% reduction compared to model computation) implies that radiation belts were void of low energy particles. These two processes are impossible to separate due to the limited observations. Nevertheless, this fact requires processes that must have accelerated particles to sufficient energies in the vicinity of Amalthea. The enhancement spreads across the main emission region, but the secondary emission rings immediately come to attention. The electron population that populates this L-shell cross the equator inside of the Amalthea, and therefore must have been pitch angle scattered while diffusing past this region. Interestingly, the enhancement can be found also at lower frequency, that is when comparing the L-band measurements, however, not as pronounced as the at higher frequencies. From this one can conclude that the pitch angle scattering affects electrons at all frequencies, however, seems to increase in efficiency at higher frequencies.
Both maps also confirm the enhancement above the poles, providing evidence that the full magnetosphere was disturbed during the 2001 flyby.

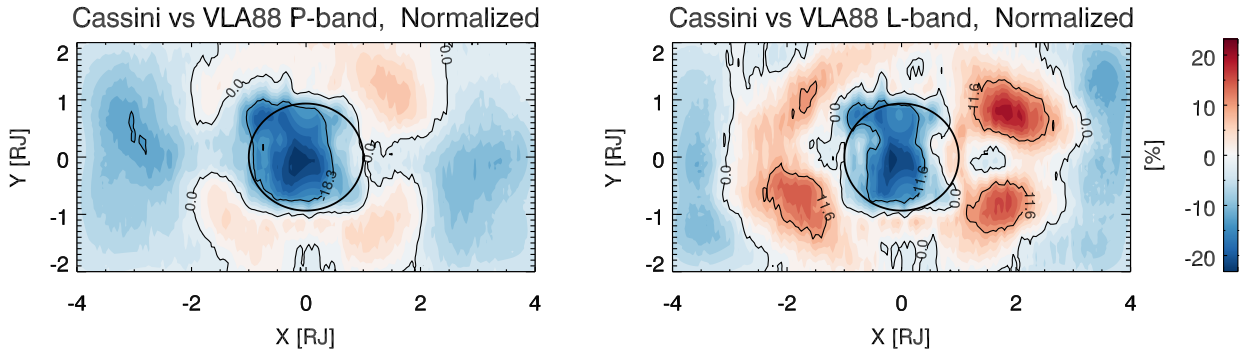

(a) VLA P-band

(b) VLA L-band

Figure 5.29: Comparison between normalized maps of the 1988 measurements [Santos-Costa et al., 2014]

6 Discussion

The Cassini synchrotron radiation maps give clues to which possible processes could alter their shape and distribution. This chapter, therefore, discusses possible scenarios that could explain the observed 2001 state.

6.1. Summary of the Observation

The retrieved maps allowed for localizing regions where the magnetosphere was disturbed. The following list summarizes the main observations on synchrotron obtained from the detailed 2001-retrieval.

Depletion of energetic electrons The flux density (Figure 5.23) is a proxy for the number density of relativistic electrons in the magnetosphere, the more particles are present, the higher is their combined emitted power. The integrated flux density of 1.10 Jy from the Cassini measurements corresponds to a depleted atmosphere, compared to model calculations that predict 65 % greater flux density [de Pater and Dunn, 2003], and compared to measurements at 14.9 GHz that report greater flux densities by 15% [Kloosterman et al., 2008] and by 36% [de Pater and Dunn, 2003]. Despite a 2.5 factor increase of the Cassini measurement compared to the initial retrieval [Bolton et al., 2002], the retrieval confirms that the magnetosphere was depleted of ultra-relativistic electrons. This is in contrast to the concurrent measurements at lower frequencies, especially at the P-band [Santos-Costa et al., 2014], which indicate an increase in flux density within the natural variability. The model curve that was fit to the 2001 measurements is based on standard modeling coefficient, however, forced a depletion of particles by truncating the electron energy that was considered.

Cassini radio maps The radio maps present the distribution of the electrons across the radiation belts. The electrons to first order can be divided into two populations: an equatorial constrained population and a more isotropic distribution that bounces between the mirror latitudes of ~ 35 deg. The coarse resolution of the Cassini Radar instrument does not allow resolving the two electron population, but their existence can be inferred by the north-south elongation. Comparison with other high-frequency maps (Section 5.8) identified an electron concentration at higher latitudes, with observational evidence that the increase is concentrated around the secondary emission rings. This feature requires a mechanism to re-distribute energetic electrons, and preferentially pitch angle scatter the ultra-relativistic electrons to higher latitudes.

VLA radio maps Comparing the normalized maps with Cassini measurements indicates an enhancement in the equatorial region [Santos-Costa et al., 2014]. Electrons must, therefore, be more abundant or more energetic at the considered L-shells (L > 3). Since particles drift inwards, the source of a number density disturbance must be located further outwards or requires in-situ acceleration at these L-shells.

6.2. Review of Known Processes

Variations in the synchrotron spectrum are an indication of changes to the energy population, and as such affect the whole spectrum [de Pater and Dunn, 2003]. Most processes are anticorrelated so that a decrease at the higher frequencies can only be accomplished by increasing the flux at lower frequencies as demonstrated by the fit in Figure 5.23. Variations pertaining only to limited frequency bands require processes that are

energy dependent and have not yet been considered in models so far [de Pater and Dunn, 2003, Santos-Costa et al., 2008]. The low flux density at high frequencies in contrast to the slightly enhanced emission at low frequency, however, indicates that processes must be acting preferentially on the energetic fraction of the electrons.

Flux density Most processes considered in previous research allow for a hardening of the spectrum, that is an increase of flux density at higher frequencies. This is in contrast with the Cassini measurement that indicates a softening of the spectrum.
The electrons supplied to the magnetosphere are a consequence of plasma exchange at the Io torus, where the outwards diffusion of cold plasma is replaced by hot plasma of solar wind origin [Khurana et al., 2004]. Fluctuations in the energetic electron number density naturally affect the integrated emitted power where the fluctuations correspond to a lag time in agreement with the inwards diffusion of the particles [Bolton et al., 1989, de Pater and Goertz, 1994, Galopeau and Gerard, 2001, Klein et al., 1989]. The inwards diffusing hot plasma is well mixed so that changes affect the synchrotron radiation across all frequencies and thus cannot explain localized changes such as the depletion at high frequencies. A similar conclusion was reached when doing a detailed study of the origin of the variability [Santos-Costa et al., 2008]. The analysis looked at the main solar wind parameter in the last couple of decades and established a good correlation between solar wind pressure and the response of the synchrotron belts. Nevertheless, the author highlights that this comparison is not applicable for the 1996-2002 window, where the agreement noticeably deteriorates. A similar breakdown of correlation was found when the radiation belts' response was analyzed to the solar flux conditions [Santos-Costa et al., 2014].
There is observational evidence that the flux density spectrum is more variable at higher frequencies (3.3 GHz vs 1.4 GHz) as inferred by changes in the spectral index [Galopeau and Gerard, 2001], however, no explanation is offered for the source of the energy dependence. Nevertheless, the research at 3.3 GHz probes a different electron population than Cassini's measurements, so that the question remains if this variability also pertains to the ultra-relativistic electron population.
Interaction with dust particles in the feeble rings of Jupiter can affect the electron population through pitch angle scattering and energy degradation [de Pater and Goertz, 1990, Santos-Costa et al., 2014]. The interaction with dust particles significantly alters low energy electrons through absorption and inelastic scattering. The faster the electron, the less affected they are by the presence of the dust particles so that interaction with dust particles leads to overall hardening of the spectrum [de Pater and Goertz, 1990]. This hypothesis was confirmed by Santos-Costa and Bolton [2008]. The study investigated the impact of different processes on the synchrotron radiation. Additional to the impact of dust particles, other factors such as radial transport, the sweeping effects of moons, and effects of rapid gyration were studied. Of all factors considered during the analysis, all factors resulted in a hardening of the spectrum, except when ignoring the moonlet's motion resonance with particles. // Singular events such as impacts from large cometary bodies can alter the radiation belts on very short time scales. There is no observational evidence for an impact before the 2001-flyby, which does however not exclude the possibility. The impact of cometary bodies was studied extensively during the Shoemaker-Levy impact [Brecht et al., 2001, de Pater et al., 1995, Harrington et al., 2004] and references therein. The comet caused a system of shockwaves to travel through the magnetosphere in combination with an increased mass loading of the ionosphere. The combined effects resulted in an increase in radial diffusion [de Pater et al., 1995], which in turn energized particles and caused an increase in flux density. The intensification (10% at 0.3 GHz and up to 45% at 5 GHz) was more pronounced at shorter wavelengths leading to a hardening of the spectrum.
A follow-up study [Millan et al., 1998] confirmed the observations, where at 9 GHz even a doubling of the synchrotron flux was observed and decay time of 300 days. Interestingly, the flux density of 1 Jy at 9 GHz is relatively low, especially compared to the 1.5 Jy after the belts have returned to their normal state. This observation is yet another sign of variability at higher frequencies with an amplitude of variation of up to 50%, whereas the lower frequency measurements are relatively stable over time.
A similar conclusion was reached when observing long-term trends after the Shoemaker-levy 9 impact, which found an enhanced variability at higher frequencies and argues for processes that pitch angle scattering effects energetic particles more drastically [Galopeau and Gerard, 2001].
In conclusion, most known processes lead to an enhancement at higher frequencies, and processes that remove particles were not considered so far. There are two remaining explanations left that could explain a depletion at higher energies.

Lack of acceleration The simplest explanation that could explain the lack of electrons is that the electrons have not undergone sufficient acceleration to reach the required energy levels. This hypothesis is consistent with the depletion of ultra-relativistic electrons and also the enhancement at lower frequencies.
The current state of the art models use radial inwards diffusion [de Pater, 1981a, Santos-Costa and Bourdarie, 2001] that causes energization of the electrons by conserving the first adiabatic invariant for an increasing magnetic field. The diffusion is most likely caused by fluctuations in the ionosphere of Jupiter [Brice and Mcdonough, 1973] and as such present time-variant phenomena in line with the Cassini observations.
There are, however, major concerns that discount this theory. A weakened radial diffusion should also cause an outward motion of the peaks [de Pater and Goertz, 1994], however, the radiation maximum at ~ 1.45 is in good agreement with other observation [de Pater and Klein, 1989] and does not confirm an outwards movement. Quite the contrary, the radiation peaks at high frequency should be located further outwards, due the shorter lifetime of energetic particles [de Pater, 1991], where the 6 cm peak locations were ~ 0.05 R_J further outwards than 20 cm counterparts. Similarly, the low resolution of the Cassini maps causes a systematic outward bias due to the skewed synchrotron radiation distribution. The convolution processes average the signal over the beam region and would conserve the peak location for a symmetric distribution. The sharp drop off towards the planet in contrast to the more shallow further outwards causes an asymmetry in the radiation. Convolving the asymmetric maps causes not only a reduction in the peak value but also shifts the peak further outwards as the energy is conserved in the process.
Lastly, this processes cannot explain the expanded magnetosphere as seen in 2001. No known relationship links radial diffusion and pitch angle scattering that can account for the enhancement at higher latitudes. Considering all arguments, it is very unlikely this processes can explain the observations.

Relativistic electron dropout The counterpart to above explanations is the existence of processes that remove particles from the magnetosphere, preferentially the energetic particles. To this date, no such processes are included in radiation models of Jupiter, as most observations could be explained without energy-dependent processes. The terrestrial radiation belts have received considerably more attention and as such are more advanced than their Jovian counterpart. During magnetospheric storms, which compress the day-side magnetosphere substantially, spacecraft have observed Relativistic Electron Dropouts (RED), which describe a sudden depletion of the energetic particles on very short time scales. Despite some fundamental differences between the two magnetospheres, such processes are the best candidate for explaining the 2001 radiation belts.

6.3. Review of Relativistic Electron Dropouts

The first in-situ observation of a sudden depletion in MeV electrons come from the Explorer 12 spacecraft's particle detectors [Freeman, 1964], which highlighted the variable dynamics present in the magnetosphere. The impact of precipitating electrons was also confirmed by ground-based observations through their effects on the auroral zones [Bailey, 1968]. This section aims at summarizing the most important points of relativistic electron dropouts; the interested reader is referred to more specialized literature for an in-depth review [Millan and Thorne, 2007, Summers et al., 1998, Takahashi, 2006, Thorne and Kennel, 1971, Thorne et al., 2006].
Rapid electron dropouts were found to be a common occurrence during magnetospheric storms and substorms, which cause a compression of the magnetosphere on the sunwards side, and results in a movement of charged particles in the radiation belts. The events are initiated around the midnight sector, causing a redistribution of electrons through a combination of acceleration and scattering processes [Millan and Thorne, 2007]. The acceleration can cause particles to move to the outer region of the magnetosphere, a consequence of conserving the first adiabatic, where they enter different drift shells and are eventually lost to the magnetosheath. Contrary, pitch angle scattering can decrease the pitch angle of particles substantially and cause particles to be lost to the atmosphere. These two paths will lead to an efficient removal of particles, henceforth a depletion of the particles. The depletion event, which is very short lived on the order of a less than an hour [Selesnick and Blake, 2002], is followed by a period of acceleration, that requires injection of electrons into the magnetosphere and rapid acceleration to replenish the belts. The source of these particles is not yet fully established, but solar wind is cited as the most probable source [Selesnick and Blake, 2002]. The post-storm conditions determine the final state of the radiation belt, and as such both depletion and enhancement were observed with spacecraft [Reeves et al., 2003].
Wave-particle interactions describe the effect of fluctuations pertinent to the plasmasphere on the electrons.

Modeling and observations have provided clues that their impact can best explain the various events that occur during the relativistic electron dropout events [Kennel and Petschek, 1966, Thorne and Kennel, 1971]. The effect is enabled, when the gyromotion of the electrons resonates with the Doppler-shifted frequency of the plasma waves [Millan and Thorne, 2007], which leads to causes conditions for acceleration and pitch angle scattering. As such, the interaction with the plasma waves is dependent on the electrons' properties (such as energy, pitch angle) and the local magnetic field strength as seen in Equation (6.1) [Millan and Thorne, 2007]. This provides an energy dependence for the interaction, as required to explain the Cassini observations. Particles outside of the resonance condtions are consequently not affected by the plasma waves. Despite the possibility of oblique propagation, most models assume parallel propagation along the field lines, so that the velocity vector parallel to the field lines is of main interest.

$$\omega - k_{\parallel} v_{\parallel} = \frac{n\Omega_e}{\gamma} \tag{6.1}$$

- $\boldsymbol{\omega}$ $[rad/s]$ Frequency of the plasma waves
- $\boldsymbol{k_{\parallel}}$ $[-]$ Parallel wavenumber of plasma waves
- $\boldsymbol{v_{\parallel}}$ $[m/s]$ Parallel velocity of electrons
- $\boldsymbol{\Omega_e}$ $[Hz]$ Gyrofrequency of the electrons
- $\boldsymbol{n}$ $[-]$ Harmonics indicator of resonance
- $\boldsymbol{\gamma}$ $[-]$ Lorentz factor

In the terrestrial belts, these waves have been studied for decades, but there is also observational evidence that the magnetospheres of the outer planets support a wide range of waves [Zarka, 2004]. The main waves of interest are discussed below along with the applicability to the Jupiter observation:

Hiss Hiss are right-handed polarized radio waves in the inner magnetosphere. Whereas their origin is not fully established, they are found in the dense plasmasphere and seem to be produced in the equatorial region. They are acting mainly in the inner magnetosphere and interact with the low energy electron population [Summers et al., 2008]. Electrons in resonance with Hiss undergo pitch angle scattering, however, on very slow timescales of days to weeks. Since they interact with electrons at low energy levels and require dense plasma regions, it is unlikely that Hiss scattering can fully explain the observations.

Whistler mode chorus Electron-cyclotron instabilities in the magnetosphere give rise to Whistler mode chorus waves [Kennel and Petschek, 1966]. Similar to the Hiss waves, at the fundamental resonance mostly low energy particles are affected and cause pitch angle scattering of these particles [Millan and Thorne, 2007]. At higher harmonics of the resonance they also interact with higher energy electrons, therefore, its impact is felt across the whole energy population [Horne et al., 2003].

Electromagnetic ion cyclotron waves Electromagnetic ion cyclotron (EMIC) waves are caused by temperature anisotropy of ion population and propagate below the proton gyrofrequency. Protons injected during magnetic storm conditions give rise to the ring currents, which in turn excite the EMIC wave [Jordanova et al., 2001]. Whereas, the Hiss and Chorus waves are right-handed polarized waves; EMIC waves are left-handed. For resonance, the electrons have to overtake the waves with sufficient velocity to invert the sense of rotation [Millan and Thorne, 2007]. As a consequence, EMIC waves require energetic electrons to reach the required velocities, whereas they do not interact with lower energy electrons. This property makes them the prime candidate for the scattering of relativistic electrons, and for relativistic electron depletion in the terrestrial radiation belts [Thorne and Kennel, 1971].
The temperature anisotropy of the ions determines the marginal stability at which optimal wave propagation occurs. It is given in units normalized to proton-gyrofrequency, and standard values in the terrestrial belts are between 0.7-0.9 [Summers and Thorne, 2003, Thorne et al., 2006], with typical values at Jupiter around 0.8 [Bagenal et al., 1997]. The proton - gyrofrequency determines the upper limit for propagation and is often referred to as the stop band. At lower propagation frequencies, the required velocities for interaction is too high to make them a viable option. The gyrofrequency depends on the mass and charge of the particles and the local magnetic field strength. The presence of heavier ion species introduces further stop bands at their respective gyrofrequency but also affects the propagation curve in other bands. For example, the presence of HE^{+} facilitates the interaction in the vicinity of the proton stop band [Thorne et al., 2006].

The waves can lead to both an energization and rapid pitch angle scattering of ultra-relativistic electrons [Thorne et al., 2006]. It appears, that whereas acceleration is very inefficient for resonance with ultra-relativistic particles, pitch angle scattering has very short time scales associated with it [Summers et al., 1998]. These effects have been further supported through the use of simulation [Jordanova et al., 2008] and confirmed by recent spacecraft measurements, which were able to confirm both the depletion and presence of EMIC waves [Shprits et al., 2016, Tsurutani et al., 2016, Zhang et al., 2016]. The main physics and the applicability to the Jovian radiation belts are discussed in the following section, along with a short model to prove their applicability.

6.4. EMIC Wave Conditions at Jupiter

EMIC waves are generated by three known mechanisms [Thorne et al., 2006]. The first mechanism requires a large scale injection of plasma ions into the inner magnetosphere, that in turn will lead to ring currents being setup. Large scale ion flux can produce an anisotropy in the plasma temperature which in turn gives rise to EMIC waves [Kennel and Petschek, 1966]. At Jupiter, large-scale convection of ions is provided by the highly variable plasma sources at Jupiter. On the outer edge of inner magnetosphere, Io's volcanic activity is the primary source of cold plasma and injects large quantities of plasma into the Io plasma torus [Bagenal, 1994, Divine and Garrett, 1983, Kupo et al., 1976]. Variable volcanic activity can explain rapid injection of plasma ions. On the inner edge, the ionosphere injects plasma into the magnetosphere [Garrett et al., 2015, Yelle and Miller, 2004], and diffuses outwards. The ionosphere is driven by solar extreme ultraviolet flux (EUV) and as such is known to fluctuate on order of magnitudes as well. It is, therefore, conceivable that at times of intense EUV flux, the ionosphere injects large quantities of plasma into the magnetosphere, causing temperature anisotropies, which sustain EMIC waves.
The second mechanism concerns compression of the magnetosphere by the solar wind, however, due to the extended magnetosphere at Jupiter is most likely not applicable.
Lastly, ultra low-frequency (ULF) waves are known to perturb the ion population [Ozeke et al., 2017, Rasinkangas and Mursula, 1998], and as such can give rise to EMIC waves. ULF wave observations require in-situ observations, and thus there is very little information on the existence of such waves in the inner magnetosphere. The Voyager spacecraft reported on ULF waves in the middle magnetosphere [Khurana and Kivelson, 1989], however, spacecraft charging prohibited observations further inwards. Further inwards, indirect observations gave further clues on the existence of ULF waves [Arkhypov and Rucker, 2006]. It is, therefore, not unrealistic that ULF wave could also excite EMIC waves.

Simplified model This research found that enhanced emissions from high latitudes indicate pitch angle scattering must have occurred across all frequencies. Furthermore, the extent of the high-frequency maps compared to lower-frequency maps is a sign of an energy-dependent scattering process that favors energetic particles. Summers and Thorne [2003] developed an analytical expression for resonance conditions for EMIC wave interaction in multiple species plasma, which can be applied to the Jovian magnetosphere.
The authors introduced a nondimensional factor, α^*, that controls the resonance conditions and is dependent on the local magnetospheric properties:

$$\alpha^* = \frac{\Omega_e^2}{\omega_{pe}^2} \tag{6.2}$$

with,

$$\Omega_e = \frac{qB}{\gamma m_e c} \tag{6.3}$$

$$\omega_{pe} = \sqrt{4\pi N_e q^2 / m_e} \tag{6.4}$$

- $\boldsymbol{\Omega_e}$ $[Hz]$ Gyrofrequency of the electrons
- $\boldsymbol{B}$ $[T]$ Local magnetic field strength
- $\boldsymbol{\gamma}$ $[-]$ Lorentz factor
- $\boldsymbol{\omega_{pe}}$ $[rad/s]$ Plasma frequency
- $\boldsymbol{N_e}$ $[m^{-3}]$ Plasma density, cold electrons below 10 keV
- $\boldsymbol{q}$ $[C] = 1.60 \times 10^{-19}$, Charge of an electron
- $\boldsymbol{m_e}$ $[kg] = 9.11 \times 10^{-31}$ Mass of an electron

It is clear that both the magnetic field strength, B, and the local cold plasma density play a crucial role in controlling the wave-particle interaction, where a lower value for α^* is preferable. This requires a combination of dense plasma in conjunction with a weak magnetic field, the opposite of the inner magnetosphere of Jupiter. This indicates that very high energies are required to obtain resonance, and thus still a valid hypothesis.
As explained above, the resonance conditions are influenced by the ion composition, and for a multispecies plasma, denotated by the subscript $_i$, the propagation speed of the EMIC waves [Stix, 1992] is given by:

$$\frac{c^2k^2}{\omega^2} = 1 - \frac{\omega_{pe}^2}{\omega(\omega + |\Omega_E|)} - \sum_{=1}^{i} \frac{\omega_{pj}^2}{\omega(\omega - \Omega_j)} \tag{6.5}$$

$\boldsymbol{\omega_{pj}}$ $[Hz]$ Ion plasma frequency, for ion species i
$\boldsymbol{\Omega_i}$ $[Hz]$ Ion-gyrofrequency of ion species i

This relationship can be normalized to take into account the relative abundances of the main species:

$$\frac{1}{u^2} = 1 - \frac{1}{\alpha^* \epsilon x}\left(\frac{1}{1+\epsilon x} + \sum_{j}^{i} \frac{\eta_i}{m_i/m_p x - 1}\right) \tag{6.6}$$

$\boldsymbol{u}$ $[-]$ Dimensionless wave phase speed
$\boldsymbol{x}$ $[-]$ Dimensionless wave frequency, normalized by the proton-gyrofrequency
$\boldsymbol{\epsilon}$ $[-]$ $m_e/m_p = 0.00054$, electron-proton mass ratio
$\boldsymbol{\eta_i}$ $[-]$ Fractional abundance of ion species i
$\boldsymbol{m_i}$ $[-]$ Mass of ion species I

The parameter, u, controls the propagation speed of EMIC waves through the plasma. For this propagation speed, one can now calculate the energy that the electrons must possess to overtake the wave to reverse the polarity and reach resonance conditions. The highest velocity is reached when the electrons are moving parallel to field lines, that is at minimum pitch angle. The minimum energy for interaction is given by:

$$E_{min} = \gamma_{min} - 1 = \left(1 - \frac{v_\parallel^2}{c^2}\right)^{-1/2} - 1 \tag{6.7}$$

Where,

$$\frac{v_\parallel}{c} = \frac{u[\epsilon^2x^2 + (\epsilon^2x^2 + u^2(1-\epsilon^2x^2))^{1/2}]}{\epsilon^2x^2 + u^2} \tag{6.8}$$

$\boldsymbol{E_{min}}$ $[MeV]$ Minimum energy for interaction with EMIC waves of phase speed ω
$\boldsymbol{v_\parallel}$ $[m/s]$ Velocity parallel to the magnetic field lines.

The equations were verified by reproducing the results from the original research paper [Summers and Thorne, 2003], both for a simple electron-proton plasma and for the case of a more complex multispecies plasma.

Jovian plasmasphere The plasma conditions in the inner magnetosphere require in-situ exploration, so that very little information are available on its composition, however, it still allows for studying feasibility conditions. The Galileo probe before entering the Jovian atmosphere [Fischer et al., 1996, Mihalov et al., 2000] was able to measure the energetic particle flux of protons, helium, and heavier-than-helium particles. The relative abundances as displayed in Figure 6.1 are directly derived from the flux measurement, assuming a constant ion temperature.

The magnetic field at Jupiter is based on a simple dipole model that assumes an inclined dipole with strength of 1.56×10^{20} [Yoder, 1995], and the model was verified using the Khurana magnetic model [Khurana and Kivelson, 1989], developed for IDL.

Lastly, the most important parameter is the cold plasma density. Cold plasma refers to electrons below the 10keV energy level and constitutes the bulk of the plasma in the magnetosphere. The cold plasma is produced by a variety of sources:

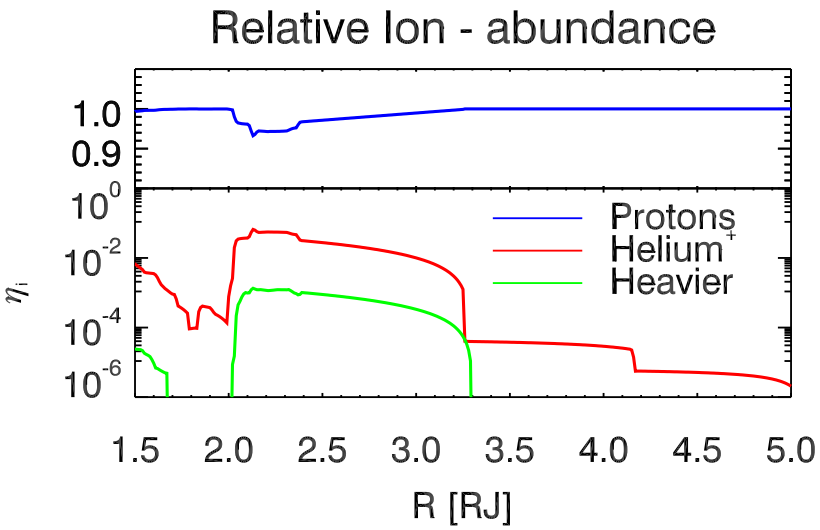

Figure 6.1: Relative ion abundance in the inner magnetosphere derived from Galileo Jupiter probe flux measurements [Fischer et al., 1996, Mihalov et al., 2000]. Note the change in y axis for the bottom panel to logarithmic coordinates.

- Io: Vulcanic activity supplies the magnetosphere continuously both directly with ions and neutrals, which are eventually also ionized in the energetic magnetospheric region [Kupo et al., 1976, Thomas et al., 2004]. As the particles are ionized, they are corotating with the magnetic field, and quickly form a plasma torus around Io's orbit. Diffusion of the plasma causes the density to drop with increasing distance from Io. The electron density varies by more than an order of magnitude depending on the location of the sampling [Gurnett, 2001].

- Ionosphere: Nagy et al. [1986] suggested early on that the ionosphere is a source of cold plasma. Photoionization of neutral particles by EUV flux produces ions in the upper thermosphere, where the number density quickly drops off with increasing altitude [Yelle and Miller, 2004]. Radio occultation measurement allows for retrieving estimates for the electron density in the ionosphere [Hinson et al., 1998, 1997] and revealed large variability in the ionospheric density, often on the order of magnitudes. Currently, there is no spatial correlation of the fluctuations indicating that they might be of temporal nature [Yelle and Miller, 2004].

- Jovian rings: Despite their low number density, the rings can contribute to the cold plasma through photoionization. Neutral particles in the rings can be ionized, similar to processes taken place in the rings of Saturn [Coates et al., 2005]. Whereas the rings are known to absorb electrons, the gaps in the Saturnian ring provide gaps for the electrons to move around [Ip, 2005] and have an order of magnitude enhanced plasma density compared to the ring region.

- Moon material: Similar to Europa [Kollmann et al., 2016, Mauk et al., 2003] and Io [Thomas et al., 2004], Amalthea might have a plasma torus associated with it. Sputtered surface material can escape the weak gravitational influence and produce a plasma torus around the orbit of Amalthea [Arkhypov and Rucker, 2013]. The existence of several small-scale objects in the vicinity of Amalthea supports the hypothesis that the small moonlet is surrounded by a neutral cloud [Fieseler et al., 2004], which in turn would quickly be ionized and formed into a plasma ring.

Variability in the source naturally propagates to the plasma density, therefore, any measurement attempt must bear in mind these variabilities and spatio-temporal variations. Figure 6.2 summarizes the main models and observation for plasma density. Whereas the synchrotron electron density can be obtained from their radio emission, the cold plasma is harder to constrain. Measuring the local cut-off plasma frequency (see Equation (6.4)) allows for the highest accuracy retrieval for an upper bound on the cold plasma and both Voyager 1 [Warwick et al., 1979] and Galileo [Bagenal et al., 1997] were able to retrieve the quantities as seen by the blue and gold solid lines in Figure 6.2. Both spacecraft sampled the middle magnetosphere relatively

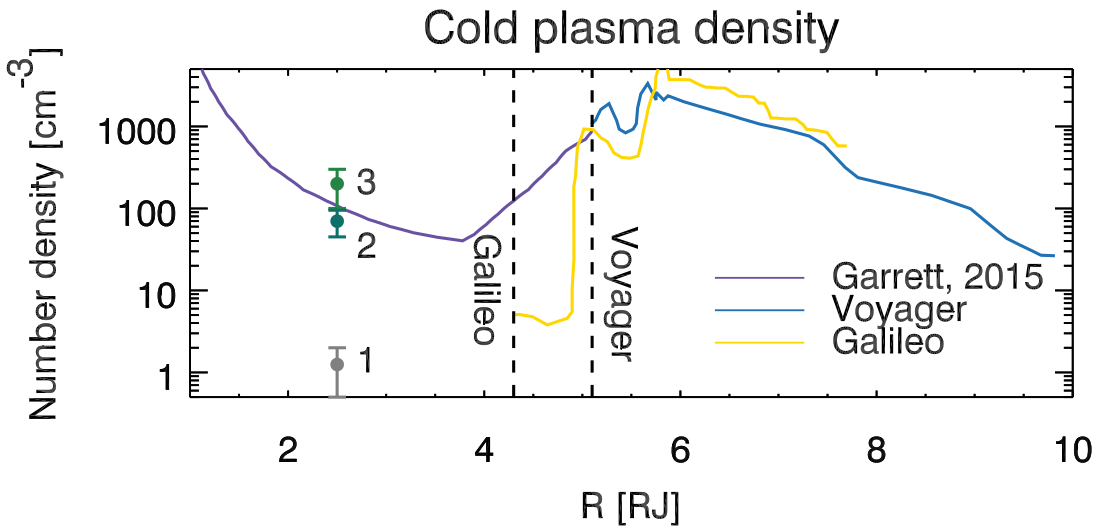

Figure 6.2: Cold plasma density overview of models and measurements from different indirect and direct observations. The purple line is based on the Divine and Garrett radiation model [Divine and Garrett, 1983, Garrett et al., 2015], the blue line is based on Voyager measuremets [Warwick et al., 1979], the golden line is based on Galileo measurements [Bagenal et al., 1997]. The dots correspond to remote observations: measurement point 1 [Hamilton and Krüger, 2008], measurement point 2[Wang et al., 1998], measurement point 3 [Arkhypov and Rucker, 2013]. The uncertainties are 10% estimates, as no information was provided in the original publications.

well, enabling a good estimate on the Io plasma tube, which can be divided in the warm, dense outer torus ($\sim 2000\ cm^{-3}$) and the colder, less dense inner torus ($\sim 1000\ cm^{-3}$). Despite the expectation that Io's plasma torus is symmetric in both directions [Herbert et al., 2008], both spacecraft measured a sudden drop in cold plasma density inwards from $\sim 5\ R_J$, where the density drops by two orders of magnitude over a distance of merely $0.05\ R_J$ [Bagenal et al., 1997]. This seems to indicate a truncation of the inner torus. At present, there are no explanations for such a sharp drop in density [Thomas et al., 2004]. The low velocity could cause the cold plasma to collapse to the spin equator, and the spacecraft's latitude could sample the depleted region outside of the spin equator. [Herbert et al., 2008] proposed a similar explanation that the torus can simply no longer be observed due the lack of power source for the emission. Lastly, the plasma model inwards of Io is based on two in-situ observation, in an environment that is characterized by large fluctuations.
Exploration of the inner magnetosphere is difficult, as the energetic synchrotron electrons saturate the receiver and do not allow for retrieval anymore. The Galileo probe and the Pioneer spacecraft transversed the inner magnetosphere, but they were only able to measure the high energetic flux, and not the cold plasma. Remote sensing of the cold plasma stems from observing the effect of plasma on other radio emissions [Arkhypov and Rucker, 2013, 2006, Wang et al., 1998] or ring particle distribution [Hamilton and Krüger, 2008]. Nevertheless, any information from the inner magnetosphere is at best a short snapshot of highly diverse region. The latest model for the inner magnetosphere plasma density [Garrett et al., 2015] is in most parts based on the original Diving and Garrett model developed by [Divine and Garrett, 1983], with some updates on the Io plasma torus and the ionosphere. The purple curve in Figure 6.2 displays the latest iteration of the plasma density inside of Io's orbit.

Resonance conditions Based on the above plasmaspheric description, one can now calculate the minimum energy for resonance conditions, at various distances of Jupiter. The first parameter of interest is the indicator, α^*. The lower this factor, the lower is the energy required for interaction.

In the vicinity of the Io's plasma torus, conditions are favorable for interaction with particles as indicated by the low resonance value [Horne et al., 2008], whereas further inside, the low plasma density does not allow for interaction. A better picture is obtained when calculating the corresponding energy of the electrons for interaction according to Equation (6.7). The red line in Figure 6.4 indicates the energy that Cassini is sensitive to, based on the approximate relationship $\nu_C = 16.08E^2B$ [Carr et al., 1983], where the magnetic field strength ist taken at the mirror points. The black lines indicates the level of energy that the electrons

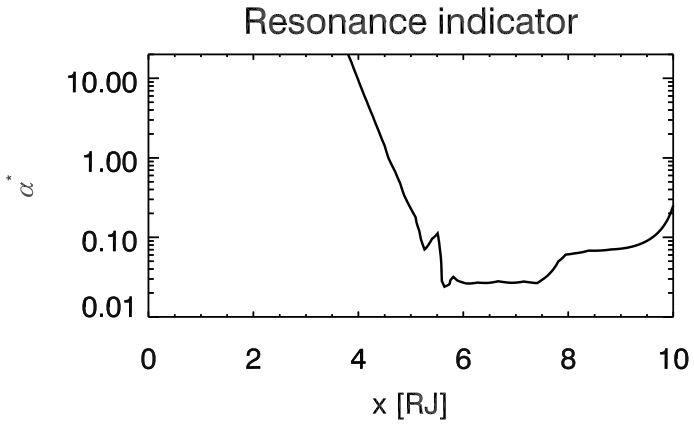

Figure 6.3: Resonance conditions (see Equation (6.2)) for the EMIC wave interaction with relativistic electrons. Lower values for α^* are favorable for interaction.

must have to interact with the EMIC waves.

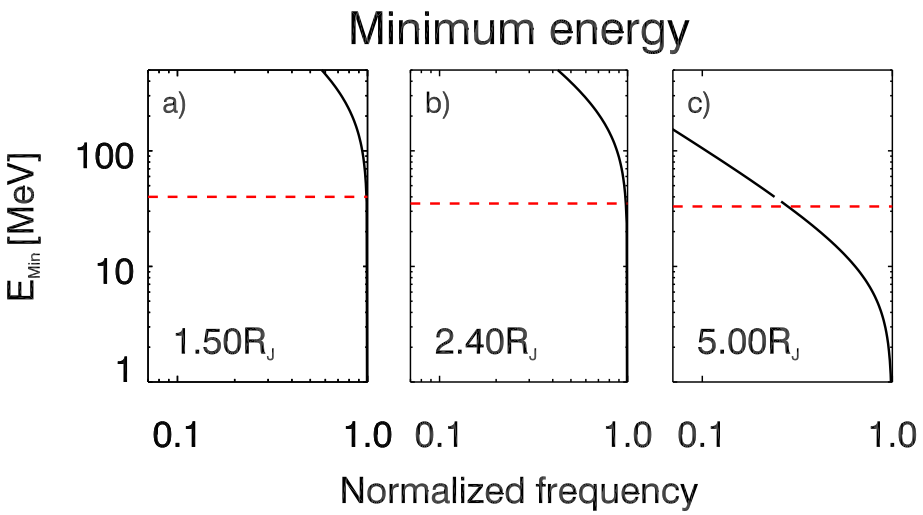

Figure 6.4: Minimum energy required for electrons to overtake EMIC waves with sufficient velocity. The red line indicates the particles energy that Cassini is sensitive to (40, 37, 30 MeV, respectively). Three regions are selected, where a) refers to the inner magnetosphere where the majority of the signal is created, b) refers to the region just inside of Amalthea orbit, and c) refers to the region where the Io plasma torus is truncated. Electrons that are resonance must have an energy around a normalized frequency ~ 0.8 and above the black line.

For optimal interaction, the normalized frequency should be around ~ 0.8. The region inside of Amalthea ($R_J < 2.5$) is of highest interest, as electrons at these distances mirror in the secondary emission rings, and thus correspond to the region that experienced enhancement. The panel b), however, indicates that for normal plasma conditions, the energy required for interaction is around 200 MeV and with that far above the level expected for Jupiter. Further inwards, the minimum energy is even higher, whereas further out (panel c), the electrons most likely do not have sufficient energy, as seen by the low brightness temperatures in the Cassini maps. Therefore, an undisturbed plasma sphere does not support EMIC wave scattering. This can explain the standard flux density in 1991 [de Pater and Dunn, 2003] and 2004 [Kloosterman et al., 2008]. However, we are looking for an extreme event, and thus it is worthwhile to consider the case of a highly disturbed plasmasphere.

Disturbed magnetosphere As explained above the plasmasphere is supplied by highly variable sources, that can fluctuate on order of magnitudes. The enhanced sources diffuse outwards and can locally change the plasma density on short time scales. The question remains if an enhancement of plasma density can explain the observations. The new resonant conditions are shown in Figure 6.5, where the resonance conditions at 0.8 intersect the energy population that Cassini is observing at an energy level of 33 MeV.

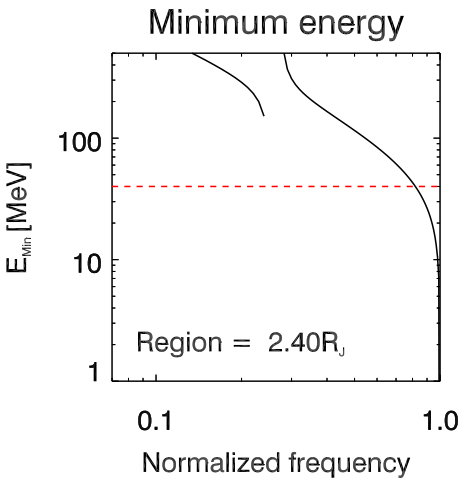

Figure 6.5: Resonance conditions for a highly disturbed plasmasphere, by a ten-fold increase in cold plasma density. The resonance conditions is given for electrons that are sensitive to the Cassini frequency.

The graphics depict the minimum energy that the electrons must possess. This condition requires the electrons to have minimum pitch angle. Amalthea effectively filters electrons with small pitch angle [de Pater et al., 1997], as the bouncing population collides with the surface. The remaining electron population inside of Amalthea is confined to the equator, henceforth, their pitch angle is too large to result in the required parallel velocity. However, it is speculated that the motion of Amalthea through the plasma excites Whistler mode waves [de Pater et al., 1997, Gurnett, 1995, Menietti et al., 2005] and in combination with the dust effects [Santos-Costa and Bolton, 2008] causes pitch angle scattering of electrons at all energy levels. As a consequence, the energetic electrons are scattered by these processes, and when their parallel velocity reaches resonance conditions, EMIC wave scattering becomes feasible. The resulting onset of rapid pitch angle scattering will remove the particles very quickly. In such an event, measurements of the flux density would observe a drop in flux, consistent with the Cassini measurements.

7

Conclusion

In retrospect, the Cassini measurements at Jupiter were a blessing. The disagreement between the initial retrieval and simulations prompted a rigorous re-analysis of the raw data and allowed and increased understanding of the variability intrinsic to the Jovian synchrotron radiation.
The calibration algorithm specifically developed for the Cassini Radar system was applied on the Jupiter raw data, incorporating the improved understanding of the radiometer, obtained from a decade of operation at Titan. The upgraded algorithms included a more refined beam pattern, an updated thermal brightness model for Jupiter, and the latest calibration factors allowing for an absolute calibration accurate below the 1% level.

The uncertainties intrinsic to the instrument, as well as the parameters of the brightness model, were obtained by fitting the Cassini observations to the brightness model of the Jupiter. The goodness-of-fit is based on five selected regions, using a-priori knowledge on the synchrotron radiation structure. The Markov-Chain Monte-Carlo optimization simultaneously solved for the uncertainties in the beam position, the parameters of the brightness model and the solutions' sensitivity to these variables.
An in-depth analysis of the uncertainties in the instrument revealed that the oscillator drifts about 0.5 seconds per day, and leading to a misrepresentation of the beam location. Similarly, the uncertainty analysis confirmed that the beam location is shifted from the boresights of the radio antenna, and shows signs of spacecraft jitter below the pointing accuracy of the Cassini. The brightness model parameters allowed for constraining the disk-averaged brightness temperature to 158.6 K $\pm$ 2.4 K, and a depletion of ammonia towards at poles as indicated by a limb darkening coefficient of 0.05 compared to 0.08 as cited in literature [de Pater et al., 2016].

The integrated flux density, a measure of the total power emitted by the electrons, was revised to 1.10 Jy $\pm$ 0.07 Jy, compared to the 0.44 Jy $\pm$ 0.15 of the initial retrieval [Bolton et al., 2002]. The variations with the longitude as given by the beaming curve are in excellent agreement with predictions and thus confirm the validity of the retrieval. Despite the 2.5 factor increase compared to the initial retrieval, the retrieval still indicates a depletion of energetic particles from the Jovian radiation belts, contrary to the enhanced flux emitted by less energetic particles.

The radio maps from Jupiter support the hypothesis that the magnetosphere in 2001 was highly disturbed, as seen by the north-south expansion of the belts. Comparison with similar high-frequency maps shows a drastic enhancement at higher latitudes, demonstrating that the energetic particles must have been redistributed. A similar conclusion is reached when comparing the normalized maps to the lower frequency observations, where an enhancement in radiation at higher latitudes and a localized brightening in the secondary emission rings, can be found.

None of the current processes in the synchrotron model can explain the Cassini observation, revealing a gap in knowledge. The observations are consistent with energy dependent pitch angle scattering, which causes particles to mirror at higher latitudes until they are eventually scattered into the loss cone, removing them from the radiation belts. Such processes are known to occur on Earth when the energetic particles resonate with waves in the plasmasphere.

Whilte a simple model indicates that the interaction is not feasible for a nominal plasmasphere, an enhancement of cold electrons allows electromagnetic ion cyclotron waves to propagate and inflict rapid pitch angle scattering on the energetic particles. This process could partially explain the short-term variability of Jupiter's synchrotron radiation, especially at higher frequencies.

Future models should consider including the effects of wave-particle interaction. The inclusion of these events allows for studying the interaction in detail, and can also help to improve the predictive capabilities of the synchrotron model. Eventually, this advancement in knowledge will be reflected in the design of the next generation of Jupiter probes, reducing the uncertainty associated with shielding from the energetic particles.

The first step towards advancing this research stems from gathering in-situ observations of the plasma conditions in the inner magnetosphere. As Juno's orbit slowly decays, the spacecraft increasingly samples the inner magnetosphere. The onboard plasma instrument can add further measurements points on the cold plasma density, and establish spatio-temporal variations. Should large flucuations be present in the plasmasphere, more simulations of the interactions are required, including estimates of the timescales involved in depleting and re-populating the magnetosphere.

Appendicies

Appendix A - VLA 2000 measurements

Radio images of Jupiter were obtained in July 2000 when the VLA was in C&D configuration. The measurement consists of three different bands, Ku (2.0 cm), K (1.3 cm) and Q (0.7 cm). The VLA Ku-band corresponds to a frequency range of 13 to 14 GHz Witz [2015] and falls in the same region as the Cassini RADAR. The effective resolution of an interferometric array such as the VLA is determined by the synthetic beam, a combination of the various baselines in the array. The maps cover a near complete rotation of Jupiter, observing Jupiter between $\sim = 30°$ and $330°$ longitude. The signal-to-strength ratio of the measurements depends on the integration time of the observations. As a consequence, short integration times of features at the beginning and end of the scan are prone to artifacts, which is resembled by the poor effective resolution at the extremes of the beam. Therefore, the beam size is used as a proxy for the reliability of the maps and used to clean the maps. An example of a cut through the beam size is given in Figure 7.1, where the red dashed line indicates the rejected portion of the beam. The rejection removes the majority of the signal from the far side of the maps, and is based on:

- Signal before the first local maxima are rejected, when taking a slice through the beam
- The first peak must exceed an effective resolution of 0.5.

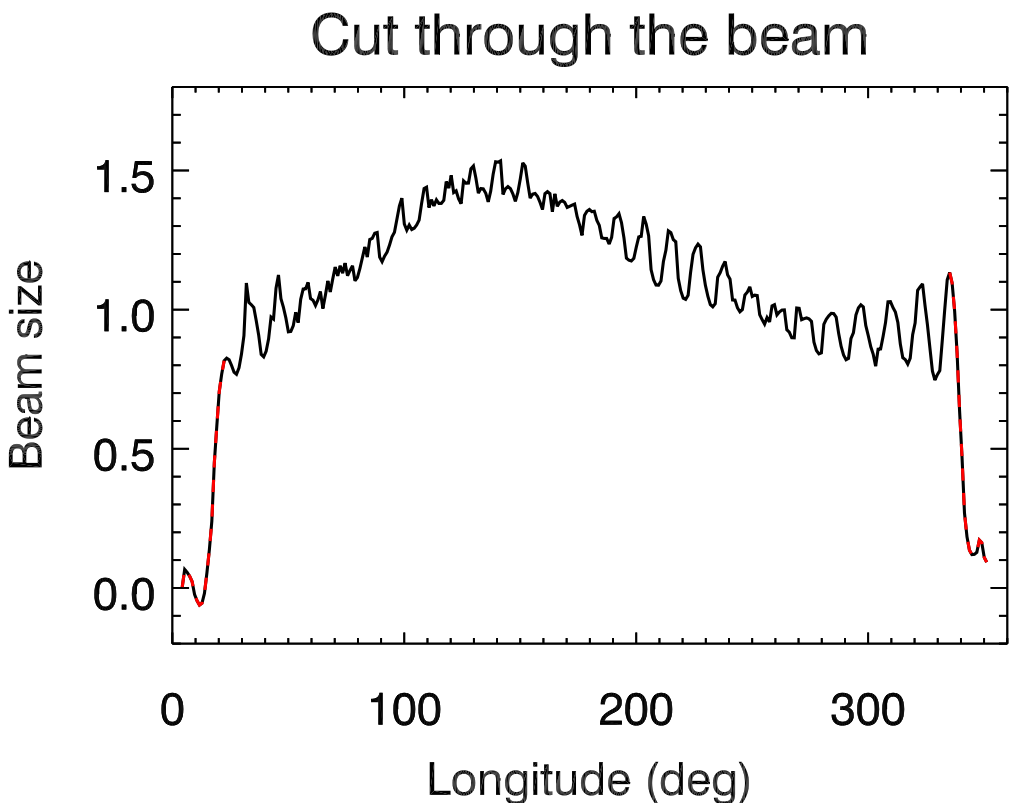

Figure 7.1: Resolution of the VLA 2000 maps, the red line indicates regions that were rejected due to the poor resolution.

The maps are very insensitive to the chosen metrics for the rejection. Especially, the zonal mean shows little influence to changes in the chosen cleaning algorithm. Nevertheless, when averaging over a smaller longitude range, the residuals at the pole start to differ.

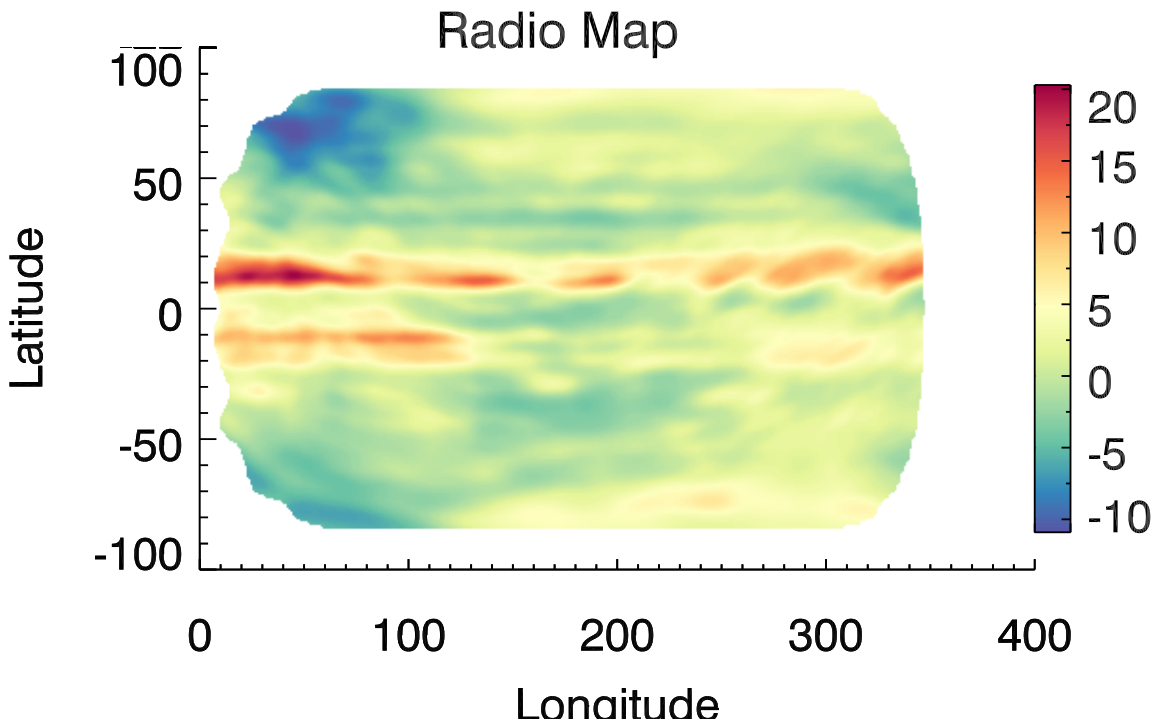

Figure 7.2: Temperature residuals of the VLA 2000 longitude resolved scans

The raw data are presented as residuals from a uniform-limb darkened disk with T_b = 140K, and a coefficient p = 0.06. A first analysis showed signs of an improper subtraction of the limb-darkened disk. More specifically, a downwards trend in the residuals at the poles indicates the need for a larger limb-darkening coefficient, and the residual offset indicates underestimated the brightness temperature. A better agreement was found, when subtracting instead a uniform-limb darkened disk with T_b = 149K, and a coefficient p = 0.07. The final best-fit brightness temperature indicates signs of absolute calibration issues so that the measured brightness temperature was about 15K lower, than more recent measurements as done by [de Pater et al., 2016, 161K] and found in this research (164K). Therefore, the final step scaled the residuals by the ratio of the brightness temperature: 164/149. The final residual map is shown in Figure 7.2.

Appendix B - Interpolating the temperature profiles

The temperature models are constructed from equatorial and zonal cuts through the atmosphere. They give the temperature distribution as a function of Jupiter's radius, so that at the limb the radius is equal to unity. These profiles are then interpolated onto a grid, first onto a circular model in polar coordinates to avoid edge effects and then an oblique model in a Cartesian grid. At every point, the local x and y coordinates are computed and the brightness temperature is obtained through a weighted average. For r ∈ [0,1] and $\theta \in$ [0,2Π]:

$$r_x = r * cos(\theta) \tag{7.1}$$

$$r_y = r * sin(\theta) \tag{7.2}$$

The temperature T_x and T_y corresponding to r_x and r_y are obtained through interpolating the input profiles to the required location. The local temperature profiles are then obtained through a weighted fit:

$$T_{r,\theta} = cos(\theta) T_x + sin(\theta) T_y \tag{7.3}$$

This temperature distribution is then interpolated onto a Cartesian grid using bilinear interpolation. The local x,y coordinates are transferred into polar coordinates, while also adjusting the local coordinates to the oblique shape of Jupiter and the four closest neighbors are bilinearly interpolated. For values exceeding the 1-bar level, the temperature is set to the CMB value of 2.7 K.

Appendix C - Individual maps

The invidual maps, projected into a magnetic frame of refrence, can be stichted together to produce a video of the synchrotron belts. Special care should be taken to the alternation of the left and right brightness peak, a sign of the East-West assymetry. The beaming effect can be appreciated when looking for systematic brightening of the belts at certain longitudes.

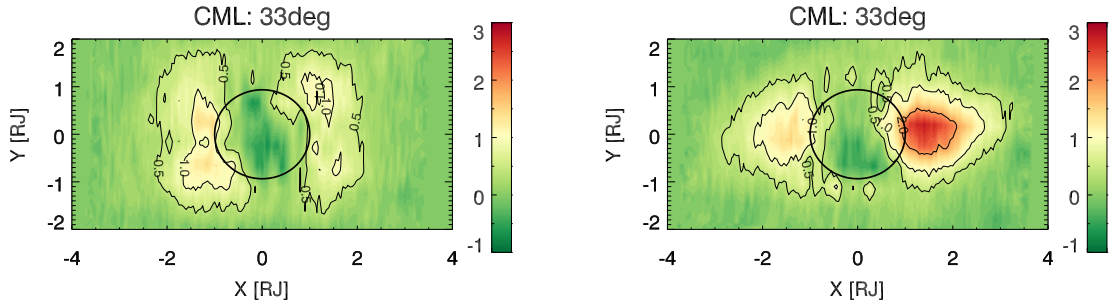

(a) Vertical polarization

(b) Horizontal Polarization

Figure 7.3: Synchrotron belt at 33° CML

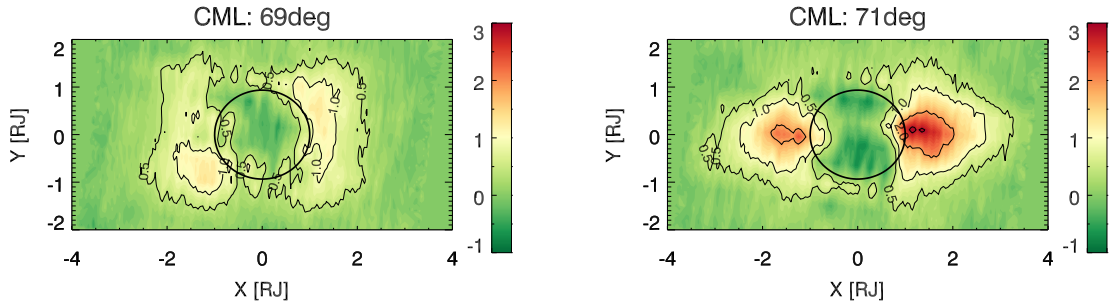

(a) Vertical polarization

(b) Horizontal Polarization

Figure 7.4: Synchrotron belt at 70° CML

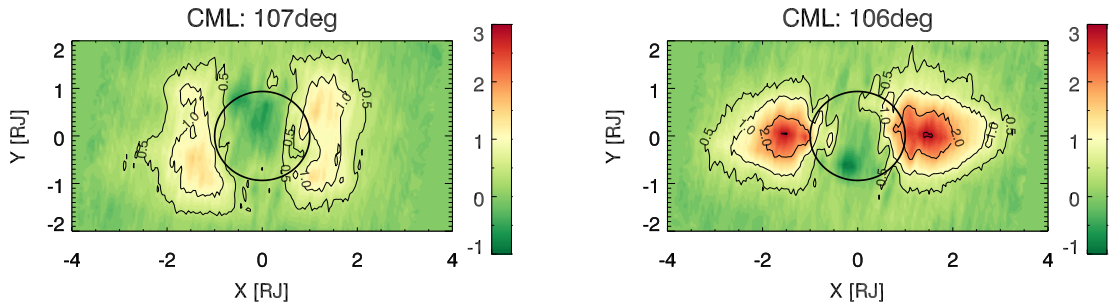

(a) Vertical polarization

(b) Horizontal Polarization

Figure 7.5: Synchrotron belt at 106° CML

Table 7.1: Uncertainty combination used for generating the individual maps.

Scan	dt [s]	dx [mrad]	dy [mrad]	T [K]	p [-]
1	0.1	0.35	0.36	161.5	0.05
2	0.1	0.34	0.23	161.25	0.05
3	0.2	0.34	0.23	162	0.05
4	0.2	0.33	0.24	161.75	0.05
5	0.2	0.33	0.25	161.75	0.05
6	0.3	0.33	0.24	161.75	0.05
7	0.3	0.33	0.24	161.5	0.05
8	0.3	0.33	0.26	161.75	0.05
9	0.3	0.33	0.26	161.5	0.05
10	0.4	0.33	0.26	161.5	0.05
11	0.1	0.39	0.57	162.5	0.06
12	0.1	0.41	0.58	162.5	0.05
13	0.1	0.4	0.57	162.5	0.05
14	0.1	0.39	0.59	162.5	0.06
15	0.1	0.4	0.58	162	0.05
16	0.15	0.39	0.57	162.5	0.06
17	0.2	0.4	0.57	162	0.06
18	0.3	0.4	0.55	162	0.05
19	0.3	0.4	0.59	162	0.05
20	0.3	0.41	0.58	161.5	0.05

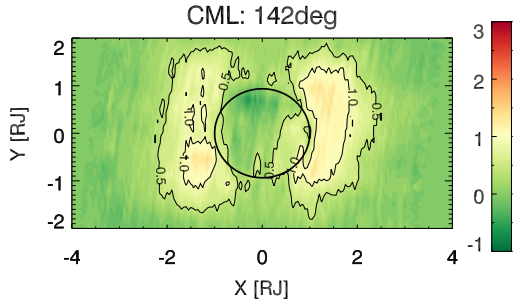

(a) Vertical polarization

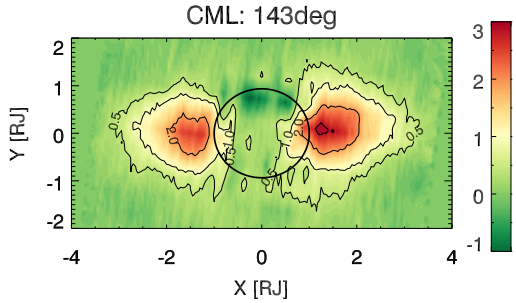

(b) Horizontal Polarization

Figure 7.6: Synchrotron belt at 142° CML

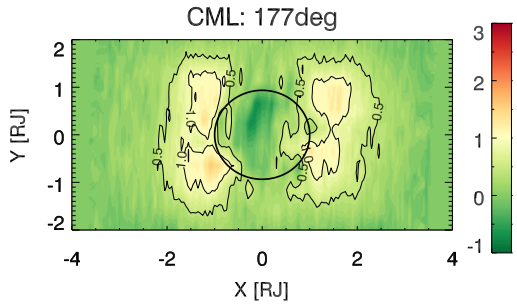

(a) Vertical polarization

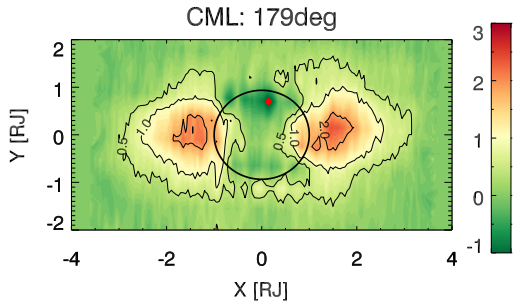

(b) Horizontal Polarization

Figure 7.7: Synchrotron belt at 178° CML

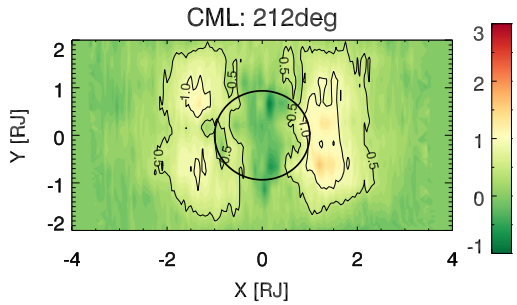

(a) Vertical polarization

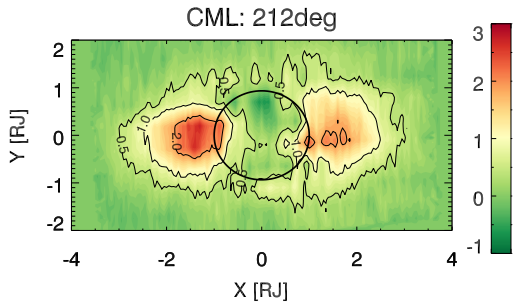

(b) Horizontal Polarization

Figure 7.8: Synchrotron belt at 212° CML

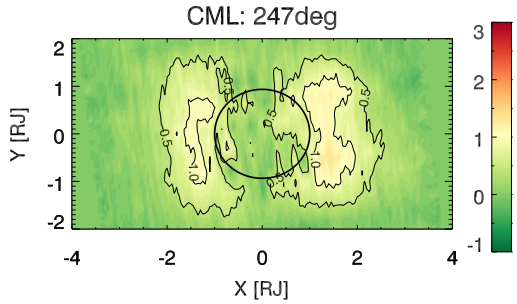

(a) Vertical polarization

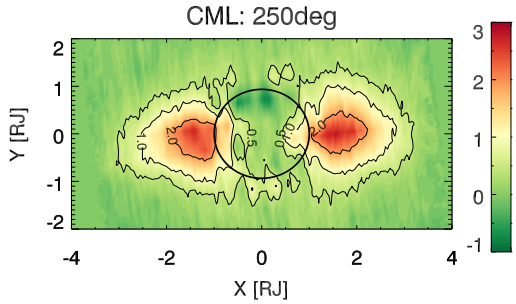

(b) Horizontal Polarization

Figure 7.9: Synchrotron belt at 248° CML

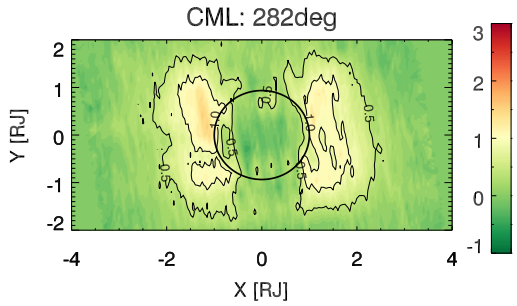

(a) Vertical polarization

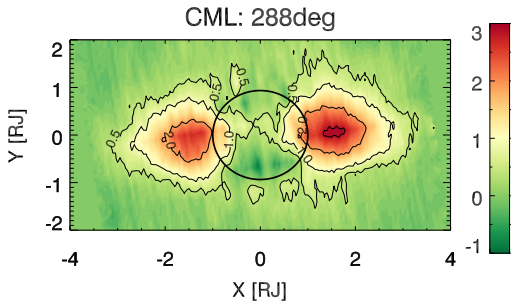

(b) Horizontal Polarization

Figure 7.10: Synchrotron belt at 286° CML

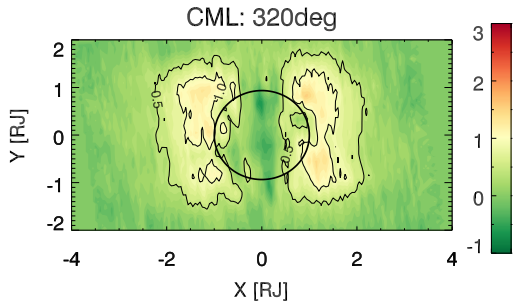

(a) Vertical polarization

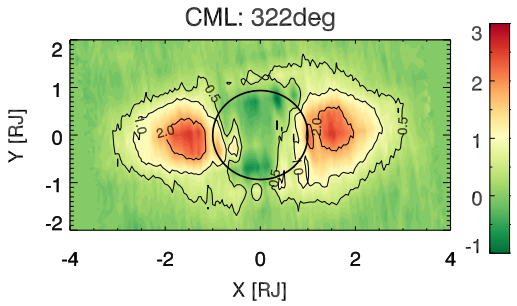

(b) Horizontal Polarization

Figure 7.11: Synchrotron belt at 321° CML

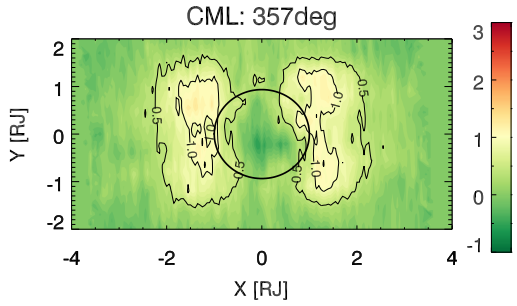

(a) Vertical polarization

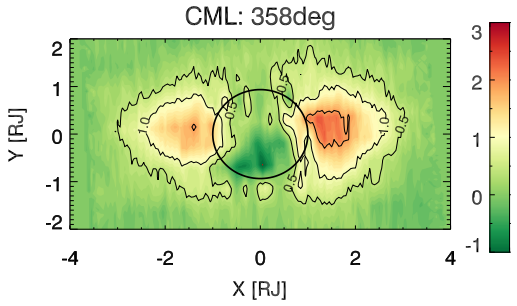

(b) Horizontal Polarization

Figure 7.12: Synchrotron belt at 358° CML

Bibliography

B. A. Archinal, M. F. A'Hearn, E. Bowell, A. Conrad, G. J. Consolmagno, R. Courtin, T. Fukushima, D. Hestroffer, J. L. Hilton, G. A. Krasinsky, et al. Report of the iau working group on cartographic coordinates and rotational elements: 2009. *Celestial Mechanics and Dynamical Astronomy*, 109(2):101–135, 2011.

O. V. Arkhypov and H. O. Rucker. Decametric modulation lanes as a probe for inner jovian magnetosphere. *Icarus*, 226(2):1214–1224, 2013.

O. Arkhypov and H. Rucker. Ultra low frequencies phenomena in jovian decametric radio emission. *Astronomy & Astrophysics*, 452(1):347–350, 2006.

F. Bagenal, F. Crary, A. Stewart, N. Schneider, D. Gurnett, W. Kurth, L. Frank, and W. Paterson. Galileo measurements of plasma density in the io torus. *Geophysical research letters*, 24(17):2119–2122, 1997.

F. Bagenal. Empirical model of the io plasma torus: Voyager measurements. *Journal of Geophysical Research: Space Physics*, 99(A6):11043–11062, 1994.

D. Bailey. Some quantitative aspects of electron precipitation in and near the auroral zone. *Reviews of Geophysics*, 6(3):289–346, 1968.

H. N. Becker, J. L. Joergensen, A. Adriani, A. Mura, J. E. P. Connerney, D. Santos-Costa, S. J. Bolton, S. Levin, J. W. Alexander, V. Adumitroaie, E. Manor-Chapman, I. Daubar, L. Clifford, M. Benn, T. Denver, J. Sushkova, C. Andrea, and R. Noschese. Observations from juno's radiation monitoring investigation during juno's first look at jupiter's inner radiation belts: Perijove 1. *Abstract P24B-05 presented at 2016 Fall Meeting*, Juno's Exploration of Jupiter and the Earth-Based Collaborative Campaign II, 2016a.

H. Becker, J. Alexander, A. Adriani, A. Mura, A. Cicchetti, R. Noschese, J. Jørgensen, T. Denver, J. Sushkova, A. Jørgensen, et al. The juno radiation monitoring (rm) investigation. *Space Science Reviews*, pages 1–39, 2016b.

G. Berge and S. Gulkis. Earth-based observations of jupiter: millimeter to meter wavelengths. Technical report, Owens Valley Radio Observatory, Pasadena, Calif.(USA), 1976.

S. J. Bolton, R. M. Thorne, S. Bourdarie, I. de Pater, and B. Mauk. Jupiter's inner radiation belts. *Jupiter. The planet, satellites and magnetosphere, Cambridge University Press, Cambridge, UK*, pages 671–688, 2004.

S. Bolton, S. Gulkis, M. Klein, I. de Pater, and T. Thompson. Correlation studies between solar wind parameters and the decimetric radio emission from jupiter. *Journal of Geophysical Research: Space Physics*, 94(A1): 121–128, 1989.

S. Bolton, M. Janssen, R. Thorne, S. Levin, M. Klein, S. Gulkis, T. Bastian, R. Sault, C. Elachi, M. Hofstadter, et al. Ultra-relativistic electrons in jupiter's radiation belts. *Nature*, 415(6875):987–991, 2002.

S. H. Brecht, I. de Pater, D. J. Larson, and M. E. Pesses. Modification of the jovian radiation belts by shoemaker–levy 9: An explanation of the data. *Icarus*, 151(1):25–38, 2001.

N. Brice and T. R. Mcdonough. Jupiter's radiation belts. *Icarus*, 18(2):206–219, 1973.

B. Burke and K. Franklin. Observations of a variable radio source associated with the planet jupiter. *Journal of Geophysical Research*, 60(2):213–217, 1955.

B. Butler and T. Bastian. Solar system objects. In *Synthesis Imaging in Radio Astronomy II*, volume 180, page 625, 1999.

T. Carr, M. Desch, and J. Alexander. Phenomenology of magnetospheric radio emissions. *Physics of the jovian magnetosphere*, 1:226–284, 1983.

A. Coates, H. McAndrews, A. Rymer, D. Young, F. Crary, S. Maurice, R. Johnson, R. Baragiola, R. Tokar, E. Sittler, et al. Plasma electrons above saturn's main rings: Caps observations. *Geophysical research letters*, 32(14), 2005.

J. Connerney, M. Acuna, N. Ness, and T. Satoh. New models of jupiter's magnetic field constrained by the io flux tube footprint. *Journal of Geophysical Research: Space Physics*, 103(A6):11929–11939, 1998.

R. G. Cosentino, B. Butler, B. Sault, R. Morales-Juberias, A. Simon, and I. de Pater. Atmospheric waves and dynamics beneath jupiter's clouds from radio wavelength observations. *Icarus*, 2017.

I. de Pater. Observations and models of the decimetric radio emission from jupiter. 1980a.

I. de Pater. 21 cm maps of jupiter's radiation belts from all rotational aspects. *Astronomy and Astrophysics*, 88:175–183, 1980b.

I. de Pater. A comparison of the radio data and model calculations of jupiter's synchrotron radiation, 1. the high energy electron distribution in jupiter's inner magnetosphere. *Journal of Geophysical Research: Space Physics*, 86(A5):3397–3422, 1981a.

I. de Pater. A comparison of radio data and model calculations of jupiter's synchrotron radiation 2. east-west asymmetry in the radiation belts as a function of jovian longitude. *Journal of Geophysical Research: Space Physics*, 86(A5):3423–3429, 1981b. ISSN 2156-2202. doi: 10.1029/JA086iA05p03423. URL `http://dx.doi.org/10.1029/JA086iA05p03423`.

I. de Pater. Jupiter's zone-belt structure at radio wavelengths: Ii. comparison of observations with model atmosphere calculations. *Icarus*, 68(2):344–365, 1986.

I. de Pater. Radio images of jupiter's synchrotron radiation at 6, 20, and 90 cm. *The Astronomical Journal*, 102: 795–805, 1991.

I. de Pater and D. E. Dunn. Vla observations of jupiter's synchrotron radiation at 15 and 22 ghz. *Icarus*, 163 (2):449–455, 2003.

I. de Pater and C. K. Goertz. Radial diffusion models of energetic electrons and jupiter's synchrotron radiation: 1. steady state solution. *Journal of Geophysical Research: Space Physics*, 95(A1):39–50, 1990.

I. de Pater and C. K. Goertz. Radial diffusion models of energetic electrons and jupiter's synchrotron radiation: 2. time variability. *Journal of Geophysical Research: Space Physics*, 99(A2):2271–2287, 1994.

I. de Pater and M. J. Klein. Time variability in jupiter's synchrotron radiation. *NASA Special Publication*, 494: 139–150, 1989.

I. De Pater and S. T. Massie. Models of the millimeter-centimeter spectra of the giant planets. *Icarus*, 62(1): 143–171, 1985.

I. de Pater and R. Sault. An intercomparison of three-dimensional reconstruction techniques using data and models of jupiter's synchrotron radiation. *Journal of Geophysical Research: Planets*, 103(E9):19973–19984, 1998.

I. de Pater, S. Kenderdine, and J. R. Dickel. Comparison of the thermal and nonthermal radiation characteristics of jupiter at 6, 11, and 21 cm with model calculations. *Icarus*, 51(1):25–38, 1982.

I. de Pater, P. N. Romani, and S. K. Atreya. Possible microwave absorption by h2s gas in uranus' and neptune's atmospheres. *Icarus*, 91(2):220–233, 1991.

I. de Pater, C. Heiles, M. Wong, R. Maddalena, et al. Outburst of jupiter's synchrotron radiation after the impact of comet shoemaker-levy 9. *Science*, 268(5219):1879, 1995.

I. de Pater, M. Schulz, and S. H. Brecht. Synchrotron evidence for amalthea's influence on jupiter's electron radiation belt. *Journal of Geophysical Research: Space Physics*, 102(A10):22043–22064, 1997.

I. de Pater, D. Dunn, P. Romani, and K. Zahnle. Reconciling galileo probe data and ground-based radio observations of ammonia on jupiter. *Icarus*, 149(1):66–78, 2001.

I. de Pater, B. Butler, D. Green, R. Strom, R. Millan, M. Klein, M. Bird, O. Funke, J. Neidhöfer, R. Maddalena, et al. Jupiter's radio spectrum from 74 mhz up to 8 ghz. *Icarus*, 163(2):434–448, 2003.

I. de Pater, R. Sault, B. Butler, D. DeBoer, and M. H. Wong. Peering through jupiter's clouds with radio spectral imaging. *Science*, 352(6290):1198–1201, 2016.

N. Divine and H. Garrett. Charged particle distributions in jupiter's magnetosphere. *Journal of Geophysical Research*, 88(A9):6889–6903, 1983.

G. Dulk, Y. Leblanc, R. Sault, H. Ladreiter, and J. Connerney. The radiation belts of jupiter at 13 and 22cm. ii. the asymmetries and the magnetic field. *Astronomy and Astrophysics*, 319:282–289, 1997.

R. Durrer. The cosmic microwave background: the history of its experimental investigation and its significance for cosmology. *Classical and Quantum Gravity*, 32(12):124007, 2015.

C. Elachi, M. Allison, L. Borgarelli, P. Encrenaz, E. Im, M. Janssen, W. Johnson, R. Kirk, R. Lorenz, J. Lunine, et al. Radar: the cassini titan radar mapper. *Space Science Reviews*, 115(1-4):71–110, 2004.

P. D. Fieseler, O. W. Adams, N. Vandermey, E. Theilig, K. A. Schimmels, G. D. Lewis, S. M. Ardalan, and C. J. Alexander. The galileo star scanner observations at amalthea. *Icarus*, 169(2):390–401, 2004.

H. Fischer, E. Pehlke, G. Wibberenz, L. Lanzerotti, and J. Mihalov. High-energy charged particles in the innermost jovian magnetosphere. *Science*, 272(5263):856, 1996.

D. Fixsen, E. Cheng, J. Gales, J. C. Mather, R. Shafer, and E. Wright. The cosmic microwave background spectrum from the full cobe* firas data set. *The Astrophysical Journal*, 473(2):576, 1996.

J. W. Freeman. The morphology of the electron distribution in the outer radiation zone and near the magnetospheric boundary as observed by explorer 12. *Journal of Geophysical Research*, 69(9):1691–1723, 1964.

M. Fulchignoni, F. Ferri, F. Angrilli, A. Ball, A. Bar-Nun, M. Barucci, C. Bettanini, G. Bianchini, W. Borucki, G. Colombatti, et al. In situ measurements of the physical characteristics of titan's environment. *Nature*, 438(7069):785–791, 2005.

P. Galopeau and E. Gerard. Variations of jupiter's synchrotron radiation: a link with solar activity? *Planetary and Space Science*, 49(13):1379–1391, 2001.

H. B. Garrett, W. Kim, B. Belland, and R. Evans. Jovian plasma modeling for mission design. 2015.

E. Gerard. Long term variations of the decimetric radio emission of jupiter (and saturn?). In *The Magnetospheres of the Earth and Jupiter*, pages 237–239. Springer, 1970.

C. Geyer. Introduction to markov chain monte carlo. *Handbook of markov chain monte carlo*, pages 3–48, 2011.

J. Gibson, W. J. Welch, and I. De Pater. Accurate jovian radio flux density measurements show ammonia to be subsaturated in the upper troposphere. *Icarus*, 173(2):439–446, 2005.

V. Ginzburg and S. Syrovatskii. Cosmic magnetobremsstrahlung (synchrotron radiation). *Annual Review of Astronomy and Astrophysics*, 3(1):297–350, 1965.

C. K. Goertz, J. A. Van Allen, and M. F. Thomsen. Further observational support for the lossy radial diffusion model of the inner jovian magnetosphere. *Journal of Geophysical Research: Space Physics*, 84(A1):87–92, 1979.

D. Gurnett. Electron densities near io from galileo plasma wave observations. *Journal of Geophysical Research. A. Space Physics*, 106:26, 2001.

D. A. Gurnett. The whistler-mode bow wave of an asteroid. *Journal of Geophysical Research: Space Physics*, 100(A11):21623–21629, 1995.

D. P. Hamilton and H. Krüger. The sculpting of jupiter's gossamer rings by its shadow. *Nature*, 453(7191): 72–75, 2008.

C. J. Hansen, S. J. Bolton, D. L. Matson, L. J. Spilker, and J.-P. Lebreton. The cassini–huygens flyby of jupiter. *Icarus*, 172(1):1–8, 2004.

P. C. Hansen, V. Pereyra, and G. Scherer. *Least squares data fitting with applications*. JHU Press, 2012.

J. Harrington, I. de Pater, S. H. Brecht, D. Deming, V. Meadows, K. Zahnle, and P. D. Nicholson. Lessons from shoemaker-levy 9 about jupiter and planetary impacts. *Jupiter: The Planet, Satellites and Magnetosphere. F. Bagenal, T. Dowling, W. McKinnon, Eds. Cambridge Univ. Press*, pages 158–184, 2004.

F. Herbert, N. M. Schneider, and A. Dessler. New description of io's cold plasma torus. *Journal of Geophysical Research: Space Physics*, 113(A1), 2008.

D. Hilbert and S. Cohn-Vossen. *Geometry and the Imagination*, volume 87. American Mathematical Soc., 1952.

D. P. Hinson, J. D. Twicken, and E. Karayel. Jupiter's ionosphere: New results from voyager 2 radio occultation measurements. *Journal of Geophysical Research: Space Physics*, 103(A5):9505–9520, 1998.

D. Hinson, F. Flasar, A. Kliore, P. Schinder, J. Twicken, and R. Herrera. Jupiter's ionosphere: Results from the first galileo radio occultation experiment. *Geophysical Research Letters*, 24(17):2107–2110, 1997.

I. I. Hirschman and D. V. Widder. *The convolution transform*. Courier Corporation, 2012.

R. B. Horne, N. P. Meredith, R. M. Thorne, D. Heynderickx, R. H. Iles, and R. R. Anderson. Evolution of energetic electron pitch angle distributions during storm time electron acceleration to megaelectronvolt energies. *Journal of Geophysical Research: Space Physics*, 108(A1), 2003.

R. B. Horne, R. M. Thorne, S. A. Glauert, J. D. Menietti, Y. Y. Shprits, and D. A. Gurnett. Gyro-resonant electron acceleration at jupiter. *Nature Physics*, 4(4):301–304, 2008.

W.-H. Ip. An update on the ring exosphere and plasma disc of saturn. *Geophysical research letters*, 32(13), 2005.

M. Janssen, S. Bolton, S. Levin, R. Sault, M. Klein, S. Gulkis, M. Hofstadter, C. Elachi, W. Johnson, A. Bunker, et al. *Cassini radar/radiometer and VLA observations of Jupiter's synchrotron emission*. Fifth International Workshop on Planetary and Solar Radio Emission, 2001.

M. Janssen, R. Lorenz, R. West, F. Paganelli, R. Lopes, R. Kirk, C. Elachi, S. Wall, W. Johnson, Y. Anderson, et al. Titan's surface at 2.2-cm wavelength imaged by the cassini radar radiometer: Calibration and first results. *Icarus*, 200(1):222–239, 2009.

M. Janssen, A. Ingersoll, M. Allison, S. Gulkis, A. Laraia, K. Baines, S. Edgington, Y. Anderson, K. Kelleher, and F. Oyafuso. Saturn's thermal emission at 2.2-cm wavelength as imaged by the cassini radar radiometer. *Icarus*, 226(1):522–535, 2013.

M. A. Janssen. *Atmospheric Remote Sensing By Microwave Radiometry. Editor, Michael A. Janssen; Wiley, New York, NY, 1993. LC# QC871. J26 1993. ISBN# 0471628913.*, volume 1. Wiley-Interscience, 1993.

M. A. Janssen, A. Le Gall, R. M. Lopes, R. D. Lorenz, M. J. Malaska, A. G. Hayes, C. Neish, A. Solomonidou, K. Mitchell, J. Radebaugh, et al. Titan's surface at 2.18-cm wavelength imaged by the cassini radar radiometer: Results and interpretations through the first ten years of observation. *Icarus*, 270:443–459, 2016.

V. Jordanova, C. Farrugia, R. Thorne, G. Khazanov, G. Reeves, and M. Thomsen. Modeling ring current proton precipitation by electromagnetic ion cyclotron waves during the may 14–16, 1997, storm. *Journal of Geophysical Research: Space Physics*, 106(A1):7–22, 2001.

V. Jordanova, J. Albert, and Y. Miyoshi. Relativistic electron precipitation by emic waves from self-consistent global simulations. *Journal of Geophysical Research: Space Physics*, 113(A3), 2008.

C. F. Kennel and H. Petschek. Limit on stably trapped particle fluxes. *Journal of Geophysical Research*, 71(1): 1–28, 1966.

K. K. Khurana and M. G. Kivelson. Ultralow frequency mhd waves in jupiter's middle magnetosphere. *Journal of Geophysical Research: Space Physics*, 94(A5):5241–5254, 1989.

K. K. Khurana, M. G. Kivelson, V. M. Vasyliunas, N. Krupp, J. Woch, A. Lagg, B. H. Mauk, and W. S. Kurth. The configuration of jupiter's magnetosphere. *Jupiter: The planet, satellites and magnetosphere*, 1:593–616, 2004.

H. Kita, H. Misawa, F. Tsuchiya, C. Tao, and A. Morioka. Effect of solar uv/euv heating on the intensity and spatial distribution of jupiter's synchrotron radiation. *Journal of Geophysical Research: Space Physics*, 118 (10):6106–6115, 2013.

H. Kita, H. Misawa, A. Bhardwaj, F. Tsuchiya, T. Sakanoi, Y. Kasaba, C. Tao, Y. Miyoshi, and A. Morioka. Relation between the short-term variation of the jovian radiation belt and thermosphere derived from radio and infrared observations. *Journal of Geophysical Research: Space Physics*, 120(8):6614–6623, 2015.

M. J. Klein. The variability of the total flux density and polarization of jupiter's decimetric radio emission. *Journal of Geophysical Research*, 81(19):3380–3382, 1976.

M. Klein, T. Thompson, and S. Bolton. Systematic observations and correlation studies of variations in the synchrotron radio emission from jupiter. *NASA Special Publication*, 494:151–155, 1989.

M. Klein, S. Bolton, S. Gulkis, M. Janssen, S. Levin, J. Roller, and R. McLeod. *Cassini-Jupiter microwave observing campaign: DSN and GAVRT observations of Jovian synchrotron radio emissions*. Fifth International Workshop on Planetary and Solar Radio Emission, 2001.

J. L. Kloosterman, B. Butler, and I. de Pater. Vla observations of synchrotron radiation at 15 ghz. *Icarus*, 193 (2):644–648, 2008.

P. Kollmann, C. Paranicas, G. Clark, E. Roussos, A. Lagg, and N. Krupp. The vertical thickness of jupiter's europa gas torus from charged particle measurements. *Geophysical Research Letters*, 43(18):9425–9433, 2016.

I. Kupo, Y. Mekler, and A. Eviatar. Detection of ionized sulfur in the jovian magnetosphere. *The Astrophysical Journal*, 205:L51–L53, 1976.

S. M. Levin, S. J. Bolton, S. L. Gulkis, M. J. Klein, B. Bhattacharya, and R. M. Thorne. Modeling jupiter's synchrotron radiation. *Geophysical research letters*, 28(5):903–906, 2001.

G. F. Lindal, G. Wood, G. Levy, J. Anderson, D. Sweetnam, H. Hotz, B. Buckles, D. Holmes, P. Doms, V. Eshleman, et al. The atmosphere of jupiter: An analysis of the voyager radio occultation measurements. *Journal of Geophysical Research: Space Physics*, 86(A10):8721–8727, 1981.

J. M. Marr, R. L. Snell, and S. E. Kurtz. *Fundamentals of Radio Astronomy: Observational Methods*, volume 13. CRC Press, 2015.

B. Mauk, D. Mitchell, S. Krimigis, E. Roelof, and C. Paranicas. Energetic neutral atoms from a trans-europa gas torus at jupiter. *Nature*, 421(6926):920–922, 2003.

C. E. McIlwain. Coordinates for mapping the distribution of magnetically trapped particles. *Journal of Geophysical Research*, 66(11):3681–3691, 1961.

J. D. Menietti, D. A. Gurnett, and J. B. Groene. Radio emission observed by galileo in the inner jovian magnetosphere during orbit a-34. *Planetary and Space Science*, 53(12):1234–1242, 2005.

J. Mihalov, H. Fischer, E. Pehlke, and L. Lanzerotti. Energetic trapped electron measurements from the galileo jupiter probe. *Geophysical research letters*, 27(16):2445–2448, 2000.

R. Millan and R. Thorne. Review of radiation belt relativistic electron losses. *Journal of Atmospheric and Solar-Terrestrial Physics*, 69(3):362–377, 2007.

R. Millan, D. Smits, and I. de Pater. Observations of jupiter at 3.5 cm and 6.0 cm associated with the impact of comet p/shoemaker–levy 9. *Icarus*, 133(2):184–191, 1998.

Y. Miyoshi, H. Misawa, A. Morioka, T. Kondo, Y. Koyama, and J. Nakajima. Observation of short-term variation of jupiter's synchrotron radiation. *Geophysical research letters*, 26(1):9–12, 1999.

A. Nagy, A. Barakat, and R. Schunk. Is jupiter's ionosphere a significant plasma source for its magnetosphere? *Journal of Geophysical Research: Space Physics*, 91(A1):351–354, 1986.

L. G. Ozeke, I. R. Mann, K. R. Murphy, D. G. Sibeck, and D. N. Baker. Ultra-relativistic radiation belt extinction and ulf wave radial diffusion: Modeling the september 2014 extended dropout event. *Geophysical Research Letters*, 2017.

L. Page, C. Barnes, G. Hinshaw, D. Spergel, J. Weiland, E. Wollack, C. Bennett, M. Halpern, N. Jarosik, A. Kogut, et al. First-year wilkinson microwave anisotropy probe (wmap)* observations: Beam profiles and window functions. *The Astrophysical Journal Supplement Series*, 148(1):39, 2003.

J. R. Piepmeier, D. G. Long, and E. G. Njoku. Stokes antenna temperatures. *IEEE Transactions on Geoscience and Remote Sensing*, 46(2):516–527, 2008.

E. B. Pilinski and A. Y. Lee. Pointing-stability performance of the cassini spacecraft. *Journal of Spacecraft and Rockets*, 46(5):1007–1015, 2009.

R. Rasinkangas and K. Mursula. Modulation of magnetospheric emic waves by pc 3 pulsations of upstream origin. *Geophysical research letters*, 25(6):869–872, 1998.

G. Reeves, K. McAdams, R. Friedel, and T. O'Brien. Acceleration and loss of relativistic electrons during geomagnetic storms. *Geophysical Research Letters*, 30(10), 2003.

C. S. Roberts. On the relationship between the unidirectional and omnidirectional flux of trapped particles on a magnetic line of force. *Journal of Geophysical Research*, 70(11):2517–2527, 1965.

J. Roberts. The pitch angles of electrons in jupiter's radiation belt. In *Proceedings of the Astronomical Society of Australia*, volume 3, pages 53–55, 1976.

J. G. Roederer. *Dynamics of geomagnetically trapped radiation*, volume 1. Springer Science & Business Media, 1970.

A. Sanchez-Lavega and J. Gomez. The south equatorial belt of jupiter, i: Its life cycle. *Icarus*, 121(1):1–17, 1996.

D. Santos-Costa and S. Bourdarie. Modeling the inner jovian electron radiation belt including non-equatorial particles. *Planetary and Space Science*, 49(3):303–312, 2001.

D. Santos-Costa, S. Bolton, R. Thorne, Y. Miyoshi, and S. Levin. Investigating the origins of the jovian decimetric emission's variability. *Journal of Geophysical Research: Space Physics*, 113(A1), 2008.

D. Santos-Costa, S. Bolton, and R. Sault. Evidence for short-term variability of jupiter's decimetric emission from vla observations. *Astronomy & Astrophysics*, 508(2):1001–1010, 2009.

D. Santos-Costa, S. Bolton, R. Sault, R. Thorne, and S. Levin. Vla observations at 6.2 cm of the response of jupiter's electron belt to the july 2009 event. *Journal of Geophysical Research: Space Physics*, 116(A12), 2011.

D. Santos-Costa, I. de Pater, R. Sault, M. Janssen, S. Levin, and S. Bolton. Multifrequency analysis of the jovian electron-belt radiation during the cassini flyby of jupiter. *Astronomy & Astrophysics*, 568:A61, 2014.

D. Santos-Costa and S. J. Bolton. Discussing the processes constraining the jovian synchrotron radio emission's features. *Planetary and Space Science*, 56(3):326–345, 2008.

R. Sault, Y. Leblanc, and G. A. Dulk. Localized brightenings in jupiter's radiation belts resulting from comet sl9 impacts. *Geophysical research letters*, 24(19):2395–2398, 1997.

R. Sault, C. Engel, and I. de Pater. Longitude-resolved imaging of jupiter at λ= 2 cm. *Icarus*, 168(2):336–343, 2004.

R. J. Sault, P. J. Teuben, and M. C. Wright. A retrospective view of miriad. In *Astronomical Data Analysis Software and Systems IV*, volume 77, page 433, 1995.

R. Selesnick and J. Blake. Relativistic electron drift shell splitting. *Journal of Geophysical Research: Space Physics*, 107(A9), 2002.

Y. Y. Shprits, A. Y. Drozdov, M. Spasojevic, A. C. Kellerman, M. E. Usanova, M. J. Engebretson, O. V. Agapitov, I. S. Zhelavskaya, T. J. Raita, H. E. Spence, et al. Wave-induced loss of ultra-relativistic electrons in the van allen radiation belts. *Nature communications*, 7:12883, 2016.

R. M. Sloanaker. Apparent temperature of jupiter at a wave length of 10 cm. *The Astronomical Journal*, 64: 346–346, 1959.

T. H. Stix. *Waves in plasmas*. Springer Science & Business Media, 1992.

D. Summers and R. M. Thorne. Relativistic electron pitch-angle scattering by electromagnetic ion cyclotron waves during geomagnetic storms. *Journal of Geophysical Research: Space Physics*, 108(A4), 2003.

D. Summers, R. M. Thorne, and F. Xiao. Relativistic theory of wave-particle resonant diffusion with application to electron acceleration in the magnetosphere. *Journal of Geophysical Research: Space Physics*, 103(A9): 20487–20500, 1998.

D. Summers, B. Ni, N. P. Meredith, R. B. Horne, R. M. Thorne, M. B. Moldwin, and R. R. Anderson. Electron scattering by whistler-mode elf hiss in plasmaspheric plumes. *Journal of Geophysical Research: Space Physics*, 113(A4), 2008.

K. Takahashi. *Magnetospheric ULF waves: synthesis and new directions*. Number 169. Amer Geophysical Union, 2006.

N. Thomas, F. Bagenal, T. Hill, and J. Wilson. The io neutral clouds and plasma torus. *Jupiter. The planet, satellites and magnetosphere*, 1:561–591, 2004.

R. M. Thorne and C. Kennel. Relativistic electron precipitation during magnetic storm main phase. *Journal of Geophysical research*, 76(19):4446–4453, 1971.

R. M. Thorne, R. B. Horne, V. K. Jordanova, J. Bortnik, and S. Glauert. Interaction of emic waves with thermal plasma and radiation belt particles. *Magnetospheric ULF waves: synthesis and new directions*, pages 213–223, 2006.

B. Tsurutani, R. Hajra, T. Tanimori, A. Takada, R. Bhanu, A. Mannucci, G. Lakhina, J. Kozyra, K. Shiokawa, L. Lee, et al. Heliospheric plasma sheet (hps) impingement onto the magnetosphere as a cause of relativistic electron dropouts (reds) via coherent emic wave scattering with possible consequences for climate change mechanisms. *Journal of Geophysical Research: Space Physics*, 121(10), 2016.

F. T. Ulaby, R. K. Moore, and A. K. Fung. *Microwave Remote Sensing: Microwave remote sensing fundamentals and radiometry*, volume 1. Addison-Wesley Publishing Company, Advanced Book Program/World Science Division, 1981.

J. A. Van Allen. High-energy particles in the jovian magnetosphere. In *IAU Colloq. 30: Jupiter: Studies of the Interior, Atmosp here, Magnetosphere and Satellites*, volume 1, pages 928–960, 1976.

K. Wang, R. Thorne, R. Horne, and W. Kurth. Cold torus whistlers: An indirect probe of the inner jovian plasmasphere. *Journal of geophysical research*, 103(A7):14987–14994, 1998.

J. Warwick, J. Pearce, A. Riddle, J. Alexander, M. Desch, M. Kaiser, J. Thieman, T. Carr, S. Gulkis, and A. Boischot. Voyager 1 planetary radio astronomy observations near jupiter. 1979.

R. D. West, Y. Anderson, R. Boehmer, L. Borgarelli, P. Callahan, C. Elachi, Y. Gim, G. Hamilton, S. Hensley, M. A. Janssen, et al. Cassini radar sequence planning and instrument performance. *IEEE Transactions on Geoscience and Remote Sensing*, 47(6):1777–1795, 2009.

S. W. Witz. VLA - resolution. `https://science.nrao.edu/facilities/vla/docs/manuals/oss/performance/resolution`, 2015. [Online; accessed: 2016-07-30].

R. Yelle and S. Miller. *Jupiter's thermosphere and ionosphere*, volume 185. Cambridge University Press, 2004.

C. F. Yoder. *Astrometric and geodetic properties of Earth and the Solar System.* Wiley Online Library, 1995.

P. Zarka. Radio and plasma waves at the outer planets. *Advances in Space Research*, 33(11):2045–2060, 2004.

X.-J. Zhang, W. Li, R. Thorne, V. Angelopoulos, Q. Ma, J. Li, J. Bortnik, Y. Nishimura, L. Chen, D. Baker, et al. Physical mechanism causing rapid changes in ultrarelativistic electron pitch angle distributions right after a shock arrival: Evaluation of an electron dropout event. *Journal of Geophysical Research: Space Physics*, 121(9):8300–8316, 2016.

Z. Zhang, A. Hayes, M. Janssen, P. Nicholson, J. Cuzzi, I. de Pater, D. Dunn, P. Estrada, and M. Hedman. Cassini microwave observations provide clues to the origin of saturn's c ring. *Icarus*, 281:297–321, 2017.